Numerical Investigations of Particle Contamination and Thermal Effects in a Slider Disk Interface

by

Shuyu Zhang

B.S. (Tsinghua University) 1984
M.S. (Tsinghua University) 1987

A dissertation submitted in partial satisfaction of the

requirements for the degree of

Doctor of Philosophy

in

Engineering-Mechanical Engineering

in the

GRADUATE DIVISION

of the

UNIVERSITY OF CALIFORNIA at BERKELEY

Committee in charge:

Professor David B. Bogy, Chair
Professor Van P. Carey
Professor Keith Miller

1997

The dissertation of Shuyu Zhang is approved:

Chair Date

Date

Date

University of California at Berkeley

1997

NUMERICAL INVESTIGATIONS OF PARTICLE CONTAMINATION AND THERMAL EFFECTS IN A SLIDER DISK INTERFACE

by

Shuyu Zhang

CHARPTER 1

INTRODUCTION

1.1 Proximity Recording

Over the past few years, disk drive manufacturers have been focusing their efforts on increasing the areal density and capacity of their drives. It was estimated that the annual growth rate of areal density was about 60%, which enabled the hard disk drive industry to decrease storage costs by approximately 40% per year (Rottmayer, et al., 1997). This rate of improvement still shows no signs of abating and promises to continue at the present rates or even accelerate. A recent record for the areal density set by IBM was 2.64 Gbit/in^2 (News, 1997), and it is expected that the areal density can reach 10 Gbit/in^2 by 2000 (Singer, 1997).

To achieve a high areal density, part of the strategy is to have the read-write head to fly as close to the disk surface as possible. The reason for reducing the magnetic spacing is that the readback signal obtained from a magnetic recording channel is inversely proportional to the exponential of the magnetic spacing (Talke, et al. 1973; Best, 1997). The most desirable configuration from a magnetic viewpoint is the one of contact between the magnetic medium and the magnetic head. Unfortunately, the contact between the sliding surfaces generally results in wear and materials interactions, and this, in turn, results in a degradation of the performance and reliability of the recording system.

The flying height in current hard drives has been reduced to under 50 *nm*, and some drives now employ so-called proximity sliders that are designed to operate at some level of interference between the slider and the peak asperities on the disk. This ultra-low flying condition brings into being some new interface phenomena such as particle contamination, thermal asperities, etc. The existence of these phenomenon seriously decreases the reliability of hard drive operation. The study of their mechanisms and methods to reduce their effects is the motivation of this thesis.

1.2 Particle Contamination

When a slider flies very close to the disk surface, the particle contamination becomes a serious problem to the reliable operation of the hard drive. The effects of the particle contamination, such as abrasive wear and scratch on a disk surface, magnetic spacing modulation, unstable flying of the slider, etc., have been studied by several other researchers (Koka, 1989; Hiller, et al., 1993; Liu, et al., 1996). It was found that the effects were closely related to the flying characteristics of the slider and the sizes and hardnesses of the particles. Generally, the interaction of the particles with the slider/disk interface can be classified into two categories based on particle size. That is, particles small enough to go into the air bearing and particles too large to go into the air bearing. The small sized particles interact with the slider/disk interface (SDI) and accumulate on the slider surface so as to change the spacing of the interface. This not only causes unsteady flying of the slider, but also causes abrasive wear on the disk (Koka and Kumaran, 1991; Hiller and Singh, 1991). Hiller and Singh's experiment also shows that the contamination usually occurs on the taper surface at the leading edge and the rail surface at the trailing edge of the slider. The contamination on the slider surface at the trailing edge occurs in the form of whiskers that can grow in size and eventually break off. After that they are brought by the airflow back into the tapers where they are deposited again. It is observed that this indirect deposition is the main cause of contamination on the tapers.

The interactions of large particles with the tapers depend on the hardness of the particle and the angle of the tapers. They may result in scratches on the disks with the particles being embedded on the disks, or they may be broken into smaller parts if they are brittle, which may ultimately lead to unstable flying of the slider (Hiller and Brown, 1993; Koka, 1989a). The interaction between the particles and slider or disk surface is a complicated process related to momentum exchange, material properties and dynamic characteristics of the slider.

Most of the works mentioned above were focused on the observations of sliders and disks before and after the contamination tests, and little attention was paid on the process of particles moving in a SDI. Actually, one of the major sources of contamination comes from the particles that are suspended in the air and interact with a slider or disk during the operation of a hard drive. Therefore, the knowledge of how the particles move in a SDI will help in understanding the mechanism of the contamination, and finally in finding some ways to controlling the contamination.

1.3 Thermal Asperity

For proximity recording, another serious problem is the so called “thermal asperity” related to the magnetoresistive (MR) head. The principle of the MR head is simply that the resistance of the MR transducer changes with the change of the magnetization in it. Since the resistance is also temperature dependent, any temperature change can result in a significant noise in the MR readback signal. One such phenomenon called thermal asperity is induced by the contact of a MR transducer with the disk surface, which causes the temperature to rise nearby the MR transducer. This phenomenon can be simplified as a heat source moving on the head surface. Therefore, the problem is classified as one of heat conduction inside a slider. In this way, Hempstead (1974) studied the thermal response of a MR head due to friction heating between the head surface and dust particles or other asperities on the recording medium surface during relative motion of the head and medium. He assumed that the heat source produced by the interaction between the slider surface and a particle or an asperity was a point heat source moving across the surface of a semi-infinite solid, that the heat transfer in the air bearing was negligible, and that the solid surface could be regarded as insulated except for a moving point heat source. Thus, the transient temperature distribution inside the solid could be obtained by integration of the heat conduction equation (Carslaw and Jaeger, 1986).

Jander, et al. (1996) proposed a simplified geometric model for simulating the heat conduction in a MR head. They assumed that the current in the MR sensor is uniform, resulting in a uniform heat generation. By neglecting the heat transfer in the air bearing, they simplified the problem to that with a planar rectangular heat source (MR transducer) embedded in an infinite stratified medium consisting of the gap dielectric, shields, underlayer and overcoat. With these assumptions, they obtained the temperature distribution around the heat source by solving the heat conduction equation (Carslaw and Jaeger, 1986).

A common point in the works mentioned above is that the heat transfer in the air bearing was neglected. But a recent paper (Tian, et al., 1997) showed that such a simplification was questionable. They found experimentally that when a slider flies over an asperity without contact, the MR readback signal fluctuates following the fluctuation of the slider's flying height. The closer the slider is to the disk surface, the lower the magnitude of the MR readback signal. Since no contact was observed in the experiment, they concluded that the signal fluctuation, which is related to the resistance variation of the MR transducer, was caused by the fluctuation of the heat transfer in the air bearing, and that the air bearing acted as a "coolant".

If we regard a slider as a solid block, then the MR transducer can be regarded as a heat source insider the block when a current pass through it. The temperature distribution is affected by this heat source as well as the heat exchange with the air bearing and the disk. The so-called thermal asperity is a special case, where work is done by the slider/disk contact to produce an amount of heat in the slider, so as to cause a significant temperature rise around the contact point on the slider. To simulate the temperature in the MR transducer, it is important to know the mechanism of the heat transfer between a slider and air bearing, irrespective of contact, because the heat exchange between the slider and air bearing is one of the most important factors affecting the heat balance inside the slider.

1.4 Micro-structure Consideration

Micro-structure consideration is an important issue in dealing with fluids and heat transfer problems in a head disk air bearing. The flow can be regarded as micro-structure flow if its length of the molecular mean free path λ is comparable to some significant dimension L of the flow field. The dimensionless ratio $Kn=\lambda/L$ is called the Knudsen number and is used to distinguish the different flow regimes. Clearly, larger Knudsen number implies more rarefied gas flow. For flows in which the Knudsen number is not negligible, some departures from the continuum gas dynamics phenomena may be expected to occur. Of course, the change from one regime to another is gradual; but to fix ideas, the flow regimes are defined by following limits (Schaaf, et al, 1961):

continuum : $Kn < 0.01$,
slip : $0.01 < Kn < 1$,
transition : $1 < Kn < 3$,
free molecular : $3 < Kn$.

When a flow is out of the continuum regime, the traditional theorems based on the continuum assumptions are no longer valid. New approaches, or the modified traditional methods, need to be considered in solving the micro-structure problems.

In a typical SDI, the air bearing spacing is about 50 *nm* and the recess depth is about 3 *μm*. If taking length of the mean free path to be 65 *nm*, then we get the Knudsen number to range from 0.02 to 1.3, or the flow is within slip or transition regime. Therefore, micro-structure treatment needs to be considered in solving the fluid and heat transfer problems in it. These methods will be discussed in details in the related chapters later.

1.5 Research Objectives

This project consists of two parts: studying the mechanism of particle contamination and studying the mechanism of the heat transfer between the slider and the SDI. Since it is very difficult to establish the experimental methods to get direct observation results, we resort to numerical simulation in our analysis.

In studying the particle contamination, we focus our work on the motion of particles in a SDI. We first develop a model describing the motion of these particles in the air bearing. Using this model, we simulate paths of particles moving in the SDI and find the factors affecting their motion. Based on the simulation results, we try to create some slider designs that are good for reducing particle contamination.

In studying the thermal asperity, we focus our work on the mechanism of the heat transfer in a SDI. As in the particle contamination problem, we first develop a model describing the heat transfer. Using this model, we simulate the heat flux through the interface of the slider and air bearing and analyze the mechanism of the heat transfer between them. Then we study a special case of a slider flying over an asperity without contact. Through these simulations, we are able to understand how the air bearing acts as a “coolant”, and how the MR readback signal fluctuates when the slider flies over an asperity without contact.

1.6 Dissertation Structure

The thesis consists of eight chapters. The first chapter is the introduction and the eighth chapter is the conclusion. Chapter 2 to Chapter 5 illustrate the study of particle contamination and Chapter 5 and 6 illustrate the study of the thermal asperity. The model related to the particle contamination is presented in Chapter 2, and the numerical approach is illustrated in Chapter 3. Chapter 4 studies the characteristics of the particle motion in a SDI, and Chapter 5 presents some slider designs for controlling particle contamination.

The heat transfer model of an air bearing is presented in Chapter 6, and the simulation results are presented in the same chapter. Chapter 7 is concerned with the modeling and simulation of the heat flux variation between a slider and air bearing when the slider flies over an asperity. The numerical approaches used in the thermal analysis are briefly presented in these two chapters.

Tables in all chapters appear in the text, while the figures are attached after the end of each chapter. The references are listed after the conclusion of the thesis.

CHARPTER 2❶

MODEL OF PARTICLE MOTION IN A SLIDER DISK INTERFACE

2.1 Introduction

Particle motion in a flow is a very complicated process because it is not only related to the ambient flow, but also related to the interaction between the different particles if particles are densely spaced in the fluid. Since the particles can be regarded as dilute in a typical SDI, we can focus our study on a single particle's motion by ignoring the interaction between different particles.

Maxey (1993) studied the motion of a single spherical particle in an unsteady ambient flow and derived the motion equation of the particle. This equation includes terms of added-mass, Faxen corrections to the quasi-steady Stokes drag and Basset history. The basset history term is associated with the gradual viscous diffusion of vorticity away from the sphere. Since there exist a history integral term in this equation, the computation in a numerical simulation can be a time consuming process.

For the contamination of a hard drive, the particles we are interested in are extremely small and usually have much larger density than that of air. Therefore, the Basset history term and added mass term are relatively small and can be neglected, and the particle motion equation can be much simplified.

---

❶ Part of this chapter has been published in Zhang, et al., (1997b).

In the following sections, we adopt a Lagrangian type analysis to express the motion equations of a particle, in which the flow related forces and body forces are included. This approach has been widely used in analyzing the particle motions in fluids by many other researchers (Shimomizuki, et al. 1993, Liang, et al., 1993, Sommerfeld, et al., 1993). As a simplification, we assume the particles are spherical and have uniform density in the following analysis. The slider/disk system as well as the related coordinates used in the following analysis are shown in Fig. 2-1

2.1 Particle Motion Equations

Using a Lagrangian approach, we can write the particle motion equations as:

$$\frac{d\mathbf{x}_p}{dt} = \mathbf{v}_p \tag{2-1}$$

$$m_p \frac{d\mathbf{v}_p}{dt} = \sum_i \mathbf{f}_i \ , \tag{2-2}$$

where m_p is the mass of the particle, $\mathbf{x}_p$ is the position and $\mathbf{v}_p$ the velocity vector of the particle in the SDI, $\mathbf{f}_i$ are forces acting on the particle. These forces may be drag force, Saffman force (Saffman, 1964), gravity force, Magnus force (Rubinow, *et al* 1961), electro-magnetic force and possibly others.

Saffman force is a lift force for a particle moving in a shear flow. Magnus force is caused by the spin of a particle in a fluid. According to Saffman's analysis (1965), Magnus force is less by an order of magnitude than Saffman force unless the rotating speed is very much greater than the rate of shear. This conclusion is true for a particle moving in a SDI (Zhang, et al., 1997a). Therefore, we neglect the Magnus force in the motion equation (2-2). For the electro-magnetic force, we assume it is only significant when the particle is very close to the slider or disk surface and will not consider it in the model. Thus, the RHS of equation (2-2) only includes three major contributions: drag force, Saffman force and gravity force.

2.2.1 Drag Force

For a rigid spherical particle moving in an airflow, the drag force can be expressed as:

$$\mathbf{f}_d = \frac{\pi}{8} C_d C_w \rho d^2 \left|\mathbf{v} - \mathbf{v}_p\right| \left(\mathbf{v} - \mathbf{v}_p\right) \tag{2-3}$$

where C_d is the drag coefficient; C_w is the coefficient of the wall effects correction which tends to one when the particle is far from the wall; d is the diameter of the sphere; ρ is the density of the air; $\mathbf{v}$ is the velocity in the air phase.

The drag coefficient C_d is usually related to the flow and physical properties of the fluid and the shape and size of the particle. Many researchers have considered C_d and obtained results, theoretically and experimentally, for various cases. For a particle moving in a viscous flow, a simplification known as the “creeping flow” approximation applies at very low Reynolds number. In this approximation, the convective terms in the momentum equation are neglected and a solution known as “Stokes Law” is obtained. For the case of a particle moving in a rarefied gas, some researchers suggest a “slip correction factor” to modify the results obtained from the assumption of continuous flow (Clift, R., *et al*, 1978).

Liu, *et al* (1965) studied the drag of a sphere in a flow of rarefied gas by using Boltzmann’s equation for Maxwellian molecules. They obtained result that is a modification to the result of a free molecular flow and is expressed as follows:

$$C_d = C_{dfm}\left[1 - \frac{B(S)}{Kn_d}\right] \tag{2-4}$$

$$C_{dfm} = \frac{2}{S^2}\left[\frac{4S^4 + 4S^2 - 1}{4S} erf(S) + \frac{e^{-s^2}}{\sqrt{\pi}}\left(S^2 + \frac{1}{2}\right)\right] + \frac{2}{3}\frac{\sqrt{\pi}}{S}\sqrt{\frac{T_w}{T_\infty}} \qquad (2\text{-}5)$$

where the speed ratio $S = |\mathbf{v}_g - \mathbf{v}_p| / (2RT_\infty)^{1/2}$; the Knudsen number $Kn_d = \lambda / d$, and λ is the mean free path of the air; $B(S)$ is a function of the speed ratio S (Liu, *et al*, 1965); C_{dfm} is the free molecular drag of the sphere (Schaaf, *et al*, 1961). The free molecular flow is a regime of extreme rarefaction in which the molecular mean free path is many times the characteristic dimension of a body located in a gas flow. The molecules which hit the surface of the body and are then reemitted, on the average, travel very far before colliding with other molecules. It is consequently valid to neglect the effect of the reemitted particles on the incident stream, at least so far as their effects on the body itself are concerned. The incident flow is therefore assumed to be entirely undisturbed by the presence of the body.

Liu, *et al* (1965), compared their calculations with Millikan's experimental results of sphere drags corresponding to the rarefied flows which cover a range of Knudsen number ($0.01 < Kn_d < 10$) at very low speed ratio ($S < 10^{-5}$). It was found that the calculated results agree very well with Millikan's experimental results over a range of ($0.2 < Kn_d < 10$)❶. It is also noted that over a wide range of speed ratio ($S < 1$), the drag coefficient ratio C_d / C_{dfm} only slightly depends on the speed ratio S. Therefore, it is reasonable to extend the validation of equation (2-4) and (2-5) to a wider range on S (say $S < 1$).

The wall effect coefficient C_w appears in different forms for particles moving parallel or perpendicular to the wall. For particles moving parallel to a single wall, Chen and

---

❶ Experimental results of sphere drags corresponding to the near-free molecular flows rarely exists except for the measurement by Millikan. Liu *et al*'s (1965) results agrees very well with Millikan's results at points over the range of Knudsen number of $0.5 < Kn_d < 10$, which can be reasonably extended to a wider range of $0.2 < Kn_d < 10$ based on the comparison of both results.

McLaughlin (1995) calculated C_w by applying Goldman *et al*'s (1967), O'Neill's (1964) and Faxen's (1923) results, respectively, for the three different regions, based on the distances of particles from the wall. That is, applying Goldman *et al*'s (1967) result for $\delta/a<0.01$, O'Neill's (1964) result for $0.01<\delta/a<10$, and Faxen's (1923) result for $\delta/a >10$. Here, $\delta = l_w - a$, where l_w and a are respectively the distance of the particle's center from the wall and the particle's radius. Wakiya (1957) calculated the drag force for viscous flow past a spheroid between two parallel plane walls. For a sphere located at one-quarter of the distance between the two planes, Wakiya obtained C_w for Poiseuille flow and Couette flow. A comparison between GOF❶ and Wakiya's results is shown in Fig. 2-2.

It is seen that when $a/l_w < 0.8$, there is little difference in C_w among the three results. When $a/l_w > 0.8$, the GOF's result becomes much larger than Wakiya's results for both Poiseuille and Couette flows and tends to infinity when $a/l_w \to 1$. For a particle moving within the mean free path (*mfp*) distance to a wall in a rarefied gas flow as in the cases in the following, this infinite wall effect correction factor can be neglected in practical application. We assume, in this thesis, that C_w is finite when particles are close to the wall.

The results in the Fig. 2-2 also show that C_w does not change very much from the one plane wall case (GOF) to the two plane wall cases (Wakiya's results) for $a/l_w < 0.8$. For the sphere closer to the wall with $a/l_w > 0.8$, we assume that Wakiya's results are better approximations to C_w. Since we are only interested in small particles around which the velocity field can be regarded as linear, we adopt Wakiya's result for Couette flow in calculating C_w, which can be expressed as:

---

❶ GOF is used to represent the combined results of Goldman *et al* (1967), O'Neill's (1964) and Faxen's (1923) results in the respective range.

$$C_{wx} = C_{wy} = \frac{1}{1 - 0.6526(a/l_w) + 0.4003(a/l_w)^3 - 0.297(a/l_w)^4}, \tag{2-6}$$

where, subscripts x and y represent the corrections for the x and y directions of motion, and l_w is taken as the closest wall distance of the sphere.

For a sphere moving perpendicularly towards a solid plane wall, Brenner (1961) obtained a correction to the Stoke's Law by solving the creeping flow equations. His result shows that the value of the correction tends to infinity when the sphere moves closer to the wall. A reason for this is that Brenner used a continuum model to solve the problem. Chen and McLaughlin (1995) argued that the Van der Waals force becomes important when the sphere moves within a distance less than the *mfp* of the air to the wall. As a simplification, they assumed that contact occurs when the sphere is within the *mfp* distance away from the wall.

In this thesis, we use Wakiya's result (1960) for a sphere moving towards to a solid plane wall. This result agrees very closely with Brenner's result for $a/l_w < 0.1$. When the sphere moves close to the wall, Wakiya's result shows a finite value for the correction instead of an infinite value as found in Brenner's result. Wakiya's wall correction is expressed as:

$$C_{wz} = \frac{1}{1 - 1.125(a/l_w) + 0.5(a/l_w)^3}, \tag{2-7}$$

where, subscript z represents the motion in the z direction.

It should be noted that the C_w's in (2-6) and (2-7) are derived from some continuous media models, while in this report, particles are regarded as moving in a rarefied gas. An ideal approach to treat these cases is to apply the C_w's derived directly from some models considering the rarefied gas or slip boundary conditions. But unfortunately, to the

Authors' knowledge, there are still no such results available in the published literature. Therefore, we use the results from continuous media models for an approximation in this thesis. The major effect due to the introduction of the wall effect is that the particle paths are closer to the streamlines (Zhang, et al., 1997a and 1997c).

2.2.2 Saffman Force

McLaughlin (1993) presented a solution for the lift force acting on a small rigid sphere that moves parallel to a flat wall in a linear shear flow. This lift force can be expressed as:

$$f_s = \frac{9}{\pi} J \mu a^2 \Delta U \left(\frac{G}{v} \right)^{1/2}, \tag{2-8}$$

where μ and v are the viscosity and kinematic viscosity of the air; ΔU is the velocity of the sphere relative to the air flow; G is the magnitude of the velocity gradient; J is an integral coefficient. For a sphere sufficiently far from the wall ($l_w \to \infty$), J converges to Saffman's value, that is, $J \to 2.255$. When the sphere is close to the wall, J will take different values depending on the ratio $\varepsilon=(Re_G)^{1/2}/Re_s$ and a non-dimensional distance $l_w^* =(G/v)^{1/2} l_w$. Here, $Re_s=\Delta Ua/v$ and $Re_G=Ga^2/v$. For sufficiently large ε and $l_w^* <1$, the value of J from McLaughlin reduces to the result obtained by Cox and Hsu (1977), which can be expressed as:

$$J = \frac{\pi^2}{16} \left(\frac{1}{\varepsilon} + \frac{11}{6} l_w^* \right). \tag{2-9}$$

For the airflow in a recessed region of a slider, the thickness dimension is usually several micro-meters, and the relative velocity ΔU is on the order of $0.1\hat{U}$. The diameter of the particles of interest here is around 200 *nm*. Thus, Re_s~0.01 and Re_G~$\hat{U}a^2/hv$~0.01

which leads to ε ~10, and l_w^* ~ 1 or less. Therefore, the conditions for applying equations (2-8) and (2-9) are satisfied.

Since the air flow in a recessed region is approximately a planar flow, its velocity component in the *z* direction is close to zero and can be neglected. By such an approximation, ΔU and *k* in (2-8) can be expressed as:

$$\Delta U = \frac{(u_p - u)u + (v_p - v)v}{\sqrt{u^2 + v^2}} \ , \tag{2-10}$$

$$k = \left| \frac{u}{\sqrt{u^2 + v^2}} \frac{\partial u}{\partial z} + \frac{v}{\sqrt{u^2 + v^2}} \frac{\partial v}{\partial z} \right| \ , \tag{2-11}$$

where (*u*, *v*, *w*) refer to the velocity components in the (*x*, *y*, *z*) directions and subscripts *p* represent the particle. This prescription is valid throughout the following analysis unless there is a special denotation. Note that the sign of (2-10) is positive when the sphere moves faster than the airflow where it is located, which causes the lift force expressed as (2-10) to be positive, or to point to the slider. This result is consistent with Saffman's prescription for the direction of the Saffman force.

2.2.3 Gravity force

The gravity force is expressed as:

$$f_g = \frac{4}{3}\pi a^3 (\rho - \rho_p) g_z \,, \tag{2-12}$$

where g_z is the component of the gravity acceleration in the *z* direction. In (2-12), buoyancy is involved although it is negligible compared to the gravity force.

It should be pointed out that the models used for calculating the various forces on the particle require that certain conditions be met for their validity. In some cases these conditions are based on a Knudsen number defined in terms of the particle size, and in others the Knudsen number is based on the minimum dimension of the flow channel. For flow in the recessed region of the slider, the channel's minimum dimension is about 3 μm, giving a Knudsen number of about 0.02, which is small enough for the continuum assumption to be valid in calculating the flow field and also is appropriate for the first order slip model used in our flow calculations. The Saffman force calculation in a continuum flow field is valid if two different Reynolds numbers are small enough and one of them is much smaller than the other. These conditions are satisfied for the flows and particles considered here. When considering the drag we note that for particles of about 350 *nm* or less in size such as those considered here the Knudsen numbers related to their dimension is on the order of 0.2 or greater, which is within the transitional flow regime. Therefore, the rarefied gas considerations are significant, and the drag force calculation based on Liu's model (1965) is preferable.

2.3 Non-dimensional Motion Equations

We have analyzed and given explicitly all the forces appearing in equation (2-2). Substituting them into equation (2-2) and rearranging the results in a non-dimensional form, we obtain the following component expressions for the motion equations of a particle:

$$\frac{dX_p}{dT} = R_l U_p \,, \tag{2-13}$$

$$\frac{dY_p}{dT} = R_l V_p \,, \tag{2-14}$$

$$\frac{dZ_p}{dT} = R_h W_p, \tag{2-15}$$

$$\frac{dU_p}{dT} = \frac{3}{4} R_h \frac{\rho}{\rho_p} \frac{C_d C_{wx}}{D} \overline{U} \left(U - U_p\right), \tag{2-16}$$

$$\frac{dV_p}{dT} = \frac{3}{4} R_h \frac{\rho}{\rho_p} \frac{C_d C_{wy}}{D} \overline{U} \left(V - V_p\right), \tag{2-17}$$

$$\frac{dW_p}{dT} = \frac{3}{4} R_h \frac{\rho}{\rho_p} \frac{C_d C_{wz}}{D} \overline{U} \left(W - W_p\right) + \frac{27}{32} \left(\frac{1}{\varepsilon} + \frac{11}{6} l_w^*\right) \times$$

$$R_h Re_h^{-1/2} \frac{\rho}{\rho_p} \frac{\tilde{U}}{D} G^{1/2} R_h \left(\frac{\rho}{\rho_p} - 1\right) \frac{h_m}{\hat{U}} g_z \tag{2-18}$$

where, $X=x/l$, $Y=y/l$, $Z=z/h_m$ are non-dimensional position variables, l is the length of the slider and h_m the initially specified height of the air bearing at the trailing edge; $U=u/\hat{U}$, $V=v/\hat{U}$ and $W=w/\hat{U}$ are non-dimensional velocity components; non-dimensional time $T=\hat{\Omega}t$, and $\hat{\Omega}$ is the rotation speed of the disk; $\overline{U} = [(U-U_p)^2 + (V-V_p)^2 + (W-W_p)^2]^{1/2}$ and $\tilde{U} = \Delta U/\hat{U}$ are non-dimensional velocities; non-dimensional diameter $D=d/h_m$; non-dimensional numbers $R_l=\hat{U}/\hat{\Omega}l$, $R_h=\hat{U}/\hat{\Omega}h_m$, and the Reynolds number $Re_h=\hat{U}h_m/\nu$.

Equations (2-13) to (2-18) are simultaneous ODE's. They can be solved for the given initial conditions. Without losing generality, we write the initial conditions as follows:

$$\begin{aligned} &X_p(0)=X_{p0}, \\ &Y_p(0)=Y_{p0}, \\ &Z_p(0)=Z_{p0}, \\ &U_p(0)=U_{p0}, \\ &V_p(0)=V_{p0}, \end{aligned} \tag{2-19}$$

$$W_p(0)=W_{p0}.$$

2.4 Air Phase Flow

To solve equations (2-13) to (2-18), we need to know the velocity field of the air flow in the SDI. This is a typical lubrication problem because the spacing of the SDI is much smaller than the length of it. The governing momentum equations for it are a set of reduced Navier-Stokes equations. The detailed derivation can be found in related document (Gross, et al., 1980) and will not be presented in this thesis. Here, we only list the results as follows:

$$\frac{\partial p}{\partial x} = \frac{\partial}{\partial z}\left(\mu \frac{\partial u}{\partial z} \right), \tag{2-20}$$

$$\frac{\partial p}{\partial y} = \frac{\partial}{\partial z}\left(\mu \frac{\partial v}{\partial z} \right), \tag{2-21}$$

$$\frac{\partial p}{\partial z} = 0 , \tag{2-22}$$

where p is the pressure in the air phase. It is clear that the pressure is independent of z and is only a function of x and y.

Based on different boundary conditions, equations (2-20)~(2-22) have different solutions. The simplest case is the so-called “no-slip” condition, which assumes that the velocity of the fluid at the boundary is equal to the velocity of the surface it is adjacent to. For the flow in a SDI, its spacing dimension is so small that the flow is regarded as in the “slip” region. The flow of this kind is often solved by conventional methods with modified boundary conditions such as “first order slip” (Burgdorfer, 1959) , “second order slip” (Hsia, *et al*, 1983), “1.5 order slip” (Mitsuya, 1993) , etc.. Some other researchers apply the Boltzmann equation to solve the flow in an ultra-thin film (Fukui and Kaneko, 1988, 1990). In this thesis, we adopt the “first order slip” condition which is expressed as follows:

$$u(z=0)=\hat{U}+a\lambda\left.\frac{\partial u}{\partial z}\right|_{z=0}, \tag{2-23}$$

$$u(z=h)=-a\lambda\left.\frac{\partial u}{\partial z}\right|_{z=h}, \tag{2-24}$$

$$v(z=0)=\hat{V}+a\lambda\left.\frac{\partial v}{\partial z}\right|_{z=0}, \tag{2-25}$$

$$v(z=h)=-a\lambda\left.\frac{\partial v}{\partial z}\right|_{z=h}, \tag{2-26}$$

where h is the height of the air bearing and $\hat{V}$ is the flying speed of the slider in the y direction, and $a=(2-\sigma_M)/\sigma_M$ and σ_M is the momentum accommodation factor.

With boundary conditions (2-23)~(2-26), we can solve equations (2-20)~(2-22), which can be expressed as follows:

$$u=-\frac{1}{2\mu}\frac{\partial p}{\partial x}\left(a\lambda h+hz-z^2\right)+\hat{U}\left(1-\frac{z+\lambda}{h+2\lambda}\right), \tag{2-27}$$

$$\upsilon=-\frac{1}{2\mu}\frac{\partial p}{\partial y}\left(a\lambda h+hz-z^2\right)+\hat{V}\left(1-\frac{z+\lambda}{h+2\lambda}\right). \tag{2-28}$$

Or in non-dimensional form:

$$U=\frac{P_0}{2\rho\hat{U}^2}\frac{h_m}{l}Re_h\frac{\partial P}{\partial X}\left(Z^2-ZH-aKn_hH\right)+\left(1-\frac{Kn_h+Z}{2Kn_h+H}\right), \tag{2-29}$$

$$V=\frac{P_0}{2\rho\hat{U}^2}\frac{h_m}{l}Re_h\frac{\partial P}{\partial Y}\left(Z^2-ZH-aKn_hH\right)+\frac{\hat{V}}{\hat{U}}\left(1-\frac{Kn_h+Z}{2Kn_h+H}\right), \tag{2-30}$$

where $P=p/p_0$, and p_0 is the ambient pressure, $H=h/h_m$ is the non-dimensional thickness of the air bearing, and $Kn_h=\lambda/h_m$ is the Knudsen number related to the height h_m.

Solutions (2-29) and (2-30) are still incomplete because the pressure P is unknown. To get P, we can solve Reynolds equation as follow:

$$\sigma \frac{\partial PH}{\partial T} = \frac{\partial}{\partial X}\left(QPH^3 \frac{\partial P}{\partial X} - \Lambda_x PH \right) + \frac{\partial}{\partial Y}\left(QPH^3 \frac{\partial P}{\partial Y} - \Lambda_y PH \right), \qquad (2\text{-}31)$$

where, $\sigma=12\mu\hat{\Omega}\, l^2/p_0h_m^2$ is the squeeze number, Q is the flow factor, Λ_x and Λ_y are the bearing numbers $\Lambda_x=6\mu\hat{U}\, l/p_0h_m^2$ and $\Lambda_y=6\mu\hat{V}\, l/p_0h_m^2$.

Equation (2-31) is actually a generalized Reynolds equation with an optional flow factor Q based on different models (Ruiz, et al, 1990a). For the continuum model, 1st order slip model, 2nd order slip model and Fukui-Kaneko model, Q has the forms as follows:

$$Q = 1, \qquad (2\text{-}32)$$

$$Q = 1 + 6a\frac{Kn}{PH}\ , \qquad (2\text{-}33)$$

$$Q = 1 + 6\frac{Kn}{PH} + 6\left(\frac{Kn}{PH}\right)^2, \qquad (2\text{-}34)$$

$$Q = f\left(\frac{Kn}{PH}\right), \qquad (2\text{-}35)$$

where $f(Kn/PH)$ is given by Fukui, et al. (1988, 1990). To solve (2-31), we can obtain the pressure distribution in the air phase, and then the velocity field by equations (2-29) and (2-30).

2.5 Summary

The motion equations of particles in a SDI are expressed in (2-13)~(2-18) by using a Largrangian approach in which the drag force, Saffman force and gravity force are considered. We will see in the following chapters that the Saffman force is important only for the relatively large particles that can fly in recessed regions. For small particles that can go in an air bearing (usually with size d<100 *nm*), the Saffman force is very small and can be neglected.

Equations (2-13)~(2-18) need to be solved simultaneously. Before solving them, the velocity field in a SDI needs to be known, which in turn requires the solution of the Reynolds equation to obtain the pressure distribution. The numerical methods for both of these calculations are presented in Chapter 3.

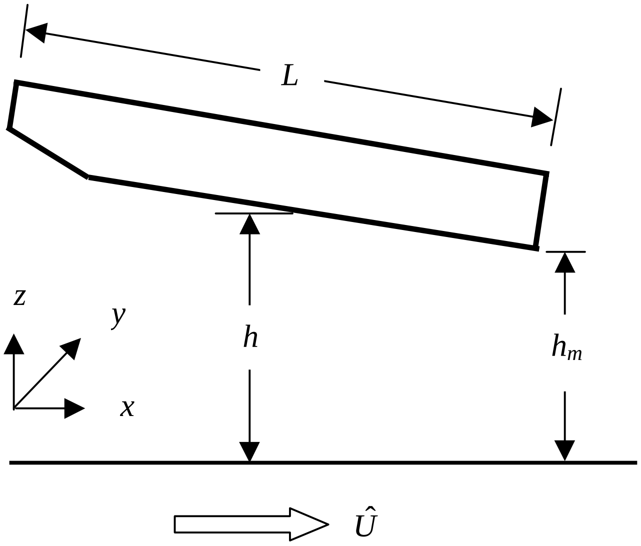

Fig. 2-1 Slider disk system and coordinates

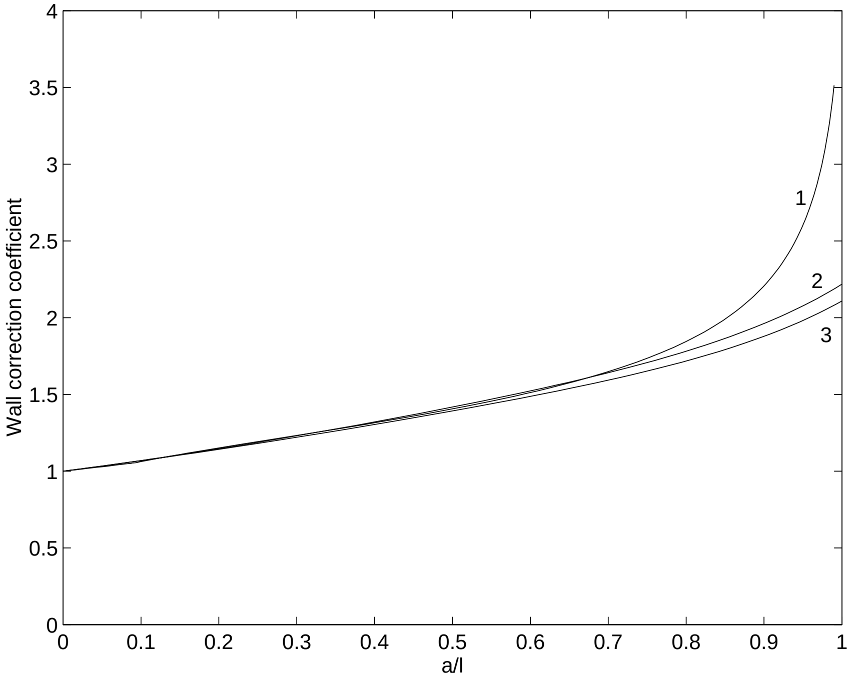

Fig. 2-2 Comparison of wall effect coefficients: 1—GOF; 2—Wakiya's, Poiseulle flow; 3—Wakiya's, Couette flow

CHAPTER 3

NUMERICAL APPROACHES

3.1 Introduction

We modeled the particle motion equations in a SDI by using a Lagrangian approach. To solve these equations, we need to calculate various forces acting on the particle, which are related to the calculation of the airflow field in the SDI. The calculation of the airflow field can be finally realized by solving the Reynolds equation to get the pressure distribution and then the velocity field.

Research on the numerical solution of air bearing slider problems has been ongoing in the Computer Mechanics Laboratory over the past decade. Garcia-Suarez *et al*. (1984) proposed a finite element method with an upwind scheme for air bearing simulations. Miu and Bogy (1986b) simulated taper-flat sliders using the factored implicit scheme of White and Nigam (1980). Ruiz and Bogy (1990a) implemented the second order slip correction and the Fukui and Kaneko (1988) model. Cha and Bogy (1995) developed a factored implicit scheme for irregular rail geometry based on a control volume formulation of the linearized Reynolds equation, and solved it using an alternating direction implicit method with time stepping. Lu and Bogy (1995) applied a control volume formulation (Patanka, 1980) to the original non-linear generalized Reynolds equation without linearization as in previous methods, and solved the problem efficiently by a combination of the alternating direction line sweeping method with a multi-grid solver.

In this chapter, we present the solution methods to the Reynolds equation and particle motion equations. We do not focus our work on improving the numerical solution of the Reynolds equation,. We will use the newest results by Lu and Bogy (1995) in our analysis. Nevertheless, we give a brief description of how the control volume method works in the solution of the Reynolds equation, so as to make the analysis in the following chapters understandable. Since we are only concerned with the mechanism of particle motion in a SDI, we restrict our study to the steady cases of air bearing flow and drop the unsteady term in the Reynolds equation. The solution procedure requires us to solve the Reynolds equation first. Then using the finite difference method and equations (2-32) and (2-33), we obtain the velocity field in the SDI. Finally, we use a 4th order Runge-Kutta method to solve the particle motion equations (2-13)~(2-18).

3.2 Integration of the Reynolds Equation

3.2.1 Reynolds Equation

Referring to equation (2-31), we can write the steady Reynolds equation as follow by dropping the unsteady term:

$$\frac{\partial}{\partial X}\left(QPH^{3}\frac{\partial P}{\partial X}-\Lambda_{x}PH\right)+\frac{\partial}{\partial Y}\left(QPH^{3}\frac{\partial P}{\partial Y}-\Lambda_{y}PH\right)=0\,. \qquad (3\text{-}1)$$

This equation can be expressed in a simply form as:

$$\frac{\partial J_x}{\partial X}+\frac{\partial J_y}{\partial Y}=0\,, \qquad (3\text{-}2)$$

where J_x and J_y are the total fluxes defined by

$$J_x \equiv \Lambda_x PH - \Gamma\frac{\partial P}{\partial X}\,, \qquad (3\text{-}3)$$

$$J_y \equiv \Lambda_y PH - \Gamma \frac{\partial P}{\partial Y}, \tag{3-4}$$

where $\Gamma = QPH^3$.

Note that the diffusion coefficient Γ is a function of the dependent variable P. Therefore, the equation (3-2) is non-linear. A typical treatment of this non-linearity in numerical fluid and heat transfer problem is to use the iteration by updating Γ with the newest value of the dependent variable.

3.2.2 Integration of the Reynolds Equation

As described in Lu and Bogy (1995), we use Patankar's (1980) control volume method to integrate the Reynolds equation. A 2-D control volume is depicted in Fig. 3-1, where the shaded area is the control volume, and ΔX and ΔY are lengths of its two edge. The capital letters E, S, W, N and P represent the grid nodes and small letters e, s, w and n represent the related control volume surfaces.

Now integrating equation (3-2) over the control volume we get

$$\int_s^n \int_w^e \frac{\partial J_x}{\partial X} dXdY + \int_s^n \int_w^e \frac{\partial J_y}{\partial Y} dXdY = 0\,. \tag{3-5}$$

If we assume the values of the fluxes are constant along each surface of the control volume, we can expand (3-5) as:.

$$J_x\big|_e \Delta Y - J_x\big|_w \Delta Y + J_y\big|_n \Delta X - J_y\big|_s \Delta X = 0\,. \tag{3-6}$$

To evaluate the values of the fluxes along each surface of the control volume, Lu and Bogy (1995) used the mean average value for the dependent variable term and the central difference for the differential term in the fluxes. The results can be expressed as:

$$J_x\big|_e = \frac{1}{2}(\Lambda_x H)_e (P_E + P_P)\Delta Y - \Gamma_e \frac{(P_E - P_P)}{(\delta x)_e} \Delta Y, \tag{3-7}$$

$$J_x\big|_w = \frac{1}{2}\left(\Lambda_x H\right)_w \left(P_W + P_P\right)\Delta Y - \Gamma_w \frac{\left(P_P - P_W\right)}{(\delta x)_w}\Delta Y, \tag{3-8}$$

$$J_y\big|_n = \frac{1}{2}\left(\Lambda_y H\right)_n \left(P_N + P_P\right)\Delta X - \Gamma_n \frac{\left(P_N - P_P\right)}{(\delta y)_n}\Delta X, \tag{3-9}$$

$$J_y\big|_s = \frac{1}{2}\left(\Lambda_y H\right)_s \left(P_S + P_P\right)\Delta X - \Gamma_s \frac{\left(P_P - P_S\right)}{(\delta y)_s}\Delta X, \tag{3-10}$$

where Γ is evaluated with the newest iteration results at each surface.

Substituting (3-7)~(3-10) into (3-6) and rearranging, we can regroup (3-6) into the following form:

$$a_P P_P = a_E P_E + a_W P_W + a_N P_N + a_S P_S + b, \tag{3-11}$$

where

$$a_E = \frac{\Gamma_e \Delta Y}{(\delta x)_e} - \frac{\left(\Lambda_x H\right)_e \Delta Y}{2}, \tag{3-12}$$

$$a_W = \frac{\Gamma_w \Delta Y}{(\delta x)_w} + \frac{\left(\Lambda_x H\right)_w \Delta Y}{2}, \tag{3-13}$$

$$a_N = \frac{\Gamma_n \Delta X}{(\delta y)_n} - \frac{\left(\Lambda_y H\right)_n \Delta X}{2}, \tag{3-14}$$

$$a_S = \frac{\Gamma_s \Delta X}{(\delta y)_s} + \frac{\left(\Lambda_y H\right)_s \Delta X}{2}, \tag{3-15}$$

$$a_P = a_E + a_w + a_N + a_S + \left[\left(\Lambda_x H\right)_e \Delta Y - \left(\Lambda_x H\right)_w \Delta Y + \right.$$

$$\left. \left(\Lambda_y H\right)_n \Delta X - \left(\Lambda_y H\right)_s \Delta X \right], \tag{3-16}$$

$$b = 0. \tag{3-17}$$

In solving a partial deferential equation numerically, an often-met problem is that of stability, which is usually related to the choice of the grid size. For example, if we choose

δx and δy too large, the coefficients a_E and a_N may become negative. The consequent iteration results may be that the value of P_P becomes unstable. Since the coefficients a_E, a_W, a_N and a_S represent the effects of the fluxes at the adjacent grids on the property at the grid P, it is required that all coefficients a_E, a_W, a_N , a_S and a_P should be positive if we use the form as (3-11). Otherwise, it will lead to a solution without physical meaning.

A variety of schemes have been devised to overcome the instability caused by the application of the central difference scheme. The resulting coefficients for these schemes (Patankar, 1980) can be summarized as:

$$a_E = \frac{\Gamma_e \Delta Y}{(\delta x)_e} A(|P_e|) + \max[-(\Lambda_x H)_e \Delta Y, 0], \tag{3-18}$$

$$a_W = \frac{\Gamma_w \Delta Y}{(\delta x)_w} A(|P_w|) + \max[(\Lambda_x H)_w \Delta Y, 0], \tag{3-19}$$

$$a_N = \frac{\Gamma_n \Delta X}{(\delta y)_n} A(|P_n|) + \max[-(\Lambda_y H)_n \Delta X, 0], \tag{3-20}$$

$$a_S = \frac{\Gamma_s \Delta X}{(\delta y)_s} A(|P_s|) + \max[(\Lambda_y H)_s \Delta X, 0], \tag{3-21}$$

$$\begin{aligned} a_P = a_E + a_w + a_N + a_S + \max\{0, [(\Lambda_x H)_e \Delta Y - (\Lambda_x H)_w \Delta Y + \\ (\Lambda_y H)_n \Delta X - (\Lambda_y H)_s \Delta X]]\}, \end{aligned} \tag{3-22}$$

$$b = \max\{0, [-(\Lambda_x H)_e \Delta Y + (\Lambda_x H)_w - \Delta Y (\Lambda_y H)_n \Delta X + (\Lambda_y H)_s \Delta X]]\}, \tag{3-23}$$

where the function $A(|P|)$ depends on the convective scheme chosen and can be found in the related documents (Patankar, 1980; Lu and Bogy, 1995).

The slider-air bearing has a geometrical peculiarity, namely, the clearance discontinuities. This poses a numerical difficulty for finite difference methods based on the differential form of the Reynolds equation. An artificial smooth function has to be used in place of the discontinuity, thus reducing the accuracy of the solution. In the present integrated control volume formulation, the clearance discontinuity does not cause any numerical difficulty. However, when a discontinuity crosses the boundary of a control volume, accuracy can be improved by using the mass flow-averaging scheme of Cha, *et al.* (1995). In this technique the mass flux on a control volume boundary with discontinuity is averaged by appropriately weighting the contribution from both sides of the discontinuity. To locate the discontinuity on the control volume boundary, Cha, et al. (1993) used an analytical method by calculating the intersection of the rail boundary and the control volume boundary. Lu, et al. (1995) used an alternative method for the general case of multiple recess levels.

3.2.3 Numerical Solver

An alternating direction line sweep method combined with a multi-grid method (Shyy, et al., 1992; Lu, et al., 1995) is implemented to solve the discretized Reynolds equation mentioned above. Compared with conventional single-grid methods, the multi-grid method solves equations on a hierarchy of grids so that all frequency components of the error are reduced at comparable rates. Inexpensive iteration on the coarse grid rapidly diminishes exactly those components of the error that are so difficult and expensive to reduce by fine grid iteration alone. This results in a dramatic reduction of solution time.

3.3 Velocity Field and Stream Function

3.3.1 Velocity Field

We need to know the velocity field of the air bearing for solving the particle motion equations (2-13)~(2-18). The velocity can be obtained by using the equations (2-29) and (2-30), in which the pressure gradient is required. We use the central difference to calculate the pressure gradient at the boundary of the control volume. For example, the pressure gradient at the "*e*" boundary is

$$\left.\frac{\partial P}{\partial X}\right|_e = \frac{P_E - P_P}{(\delta x)_e} . \tag{3-24}$$

The pressure gradients at other surfaces of the control volume can be obtained in a similar way.

Note that the location of the pressure gradient (3-24) is not coincident with any original grid points for P, as are the velocity components U and V. This is called the "staggered grids" technique which stores pressure P and velocities U and V in three different grid systems. Figure 3-2 shows how the staggered grids work, where the empty circles represent the original grids for P, solid circles represent the new grids for $\partial P/\partial X$ (or U), and solid squares represent new grids for $\partial P/\partial Y$ (or V).

3.3.2 Stream Function

Equation (3-2) is actually a mass conservation equation. Thus, there exist a stream function ψ satisfying it. By virtue of equation (3-2), we can write the stream function as:

$$J_x = \frac{\partial \psi}{\partial Y} , \tag{3-25}$$

$$J_y = -\frac{\partial \psi}{\partial X} . \tag{3-26}$$

The stream function ψ can be calculated by integrating equations (3-25) and (3-26), which in turn requires the pressure solution to get the mass fluxes (see (3-3) and (3-4)). As in calculating the velocity field, a staggered grid arrangement is applied, in which the stream function grid lines coincide with the control volume faces (Lu, 1997).

3.4 Solution of the Particle Motion Equations

We use the fourth order Runge-Kutta method to solve the particle motion equations. It is a single step method. It usually consists of an explicit method as a predictor and a implicit method as a corrector, which makes it an explicit single step method but with higher local truncation error. The fourth order Runge-Kutta method is a multi-level predictor-corrector method that uses the Forward Cauthy-Euler method (FCE), Backward Cauthy-Euler method (BCE), Mid-Point method and Simpson's method. The diagram of the 4th order Runge-Kutta method is shown in Fig. 3-3, where □ is used to denote *y*-values and • is used to denote y'-values.

Now let's turn back to the particle motion equations (2-13)~(2-18). Clearly, this is a problem of simultaneous ordinary differential equations (ODE). We can express it in a simpler form by defining two vectors $\aleph$ and $\Re$:

$$\aleph = (X_p, Y_p, Z_p, U_p, V_p, W_p)^{\mathrm{T}}, \tag{3-27}$$

$$\Re = \begin{bmatrix} R_l U_p \\ R_l V_p \\ R_h W_p \\ \frac{3}{4} R_h \, \frac{\rho}{\rho_p} \frac{C_d C_{wx}}{D} \overline{U}\left(U - U_p\right) \\ \frac{3}{4} R_h \, \frac{\rho}{\rho_p} \frac{C_d C_{wy}}{D} \overline{U}\left(V - V_p\right) \\ \frac{3}{4} R_h \, \frac{\rho}{\rho_p} \frac{C_d C_{wz}}{D} \overline{U}\left(W - W_p\right) + \frac{27}{32}\left(\frac{1}{\varepsilon} + \frac{11}{6} l_w^*\right) \times \\ R_h Re_h{}^{-1/2} \, \frac{\rho}{\rho_p} \frac{\tilde{U}}{D} G^{1/2} R_h \left(\frac{\rho}{\rho_p} - 1\right) \frac{h_m}{\hat{U}} g_z \\ \\ \end{bmatrix}, \tag{3-28}$$

where superscript “T” represents the transpose. With these definitions, we can write the particle motion equations as:

$$\frac{d\aleph}{dT} = \Re(T, \aleph). \tag{3-29}$$

Or, in a component form with initial conditions added:

$$\begin{cases} \dfrac{d\aleph_i}{dT} = \Re_i\left(T, \aleph_1, \aleph_2, \aleph_3, \aleph_4, \aleph_5, \aleph_6\right) \\ \\ \aleph_i\left(T_0\right) = \aleph_{i0} \\ \end{cases} \qquad (i{=}1, \cdots\cdots, 6). \tag{3-30}$$

For equations (3-30), the fourth order Runge-Kutta method can be written as:

$$\Phi_{i,n+1} = \Phi_{i,n} + \frac{\Delta T}{6}\left(k_{1,i} + 2k_{2,i} + 2k_{3,i} + k_{4,i}\right), \quad (i{=}1, \cdots\cdots, 6) \tag{3-31}$$

where Φ_i are the numerical solution related to the true solution $\aleph i$, and

$$k_{1,i} = \Re_i\left(T_n, \Phi_{1,n}, \ldots., \Phi_{6,n}\right), \tag{3-32}$$

$$k_{2,i} = \Re_i\left(T_n + \frac{\Delta T}{2}, \Phi_{1,n} + \frac{\Delta T}{2} k_{1,1}, \ldots., \Phi_{6,n} + \frac{\Delta T}{2} k_{1,6}\right), \tag{3-33}$$

$$k_{3,i} = \Re_i\left(T_n + \frac{\Delta T}{2}, \Phi_{1,n} + \frac{\Delta T}{2}k_{2,1}, \ldots., \Phi_{6,n} + \frac{\Delta T}{2}k_{2,6}\right), \tag{3-34}$$

$$k_{4,i} = \Re_i\left(T_n + \Delta T, \Phi_{1,n} + \Delta T k_{3,1}, \ldots., \Phi_{6,n} + \Delta T k_{3,6}\right), \tag{3-35}$$

where the subscript "n" represents the n^{th} iteration and ΔT is the integration time step. Equations (3-32)~(3-35) represent, respectively, the evaluations of the derivative parts of the FCE, BCE, mid-point and Simpson methods.

Fourth order Runge-Kutta method has an error of $(\Delta T)^4$. Theoretically, if we reduce the time step ΔT repeatedly, we may get the numerical results convergent to the true solution. But a smaller ΔT requires more computation time. In our calculation, we first choose a ΔT, say a number within 10^{-7}~10^{-6}, and obtain a solution $\mathbf{\Phi}_{\mathrm{I}}$. Then we reduce the ΔT by half and obtain another solution $\mathbf{\Phi}_{\mathrm{II}}$. If the two solutions satisfy $||\mathbf{\Phi}_{\mathrm{I}} - \mathbf{\Phi}_{\mathrm{II}}|| < \delta$, where $||\bullet||$ is a chosen norm and δ is a small number, we say the solution is convergent and we take $\mathbf{\Phi}_{\mathrm{II}}$ as the final result.

3.5 Summary

The overall procedure for solving the particle motion equations includes two parts: first solving the velocity field of the SDI, which in turn requires the solution of the Reynolds equation; then solving the motion equations (2-13)~(2-18) with the velocity field known. In this chapter, we first discussed how to use the control volume method to discretize the Reynolds equation. The discretized Reynolds equation can be solved efficiently by an alternating direction sweep method combined with a multi-grid control volume method. Then we introduced the fourth order Runge-Kutta method that will be used to solve the simultaneous ODE's (2-13)~(2-18). Note that the integration of the particle motion equations needs the values of velocity and velocity gradient in the SDI, which are stored at the separated grid nodes. If the location of a particle does not fall on one of these nodes at a integration step, say it falls inside a control volume, then the calculation at this step is finished by evaluating all the required information of the SDI using a linear interpolation. Here the staggered control volumes for pressure *P* and the velocity *U* and *V* should not be miss-used.

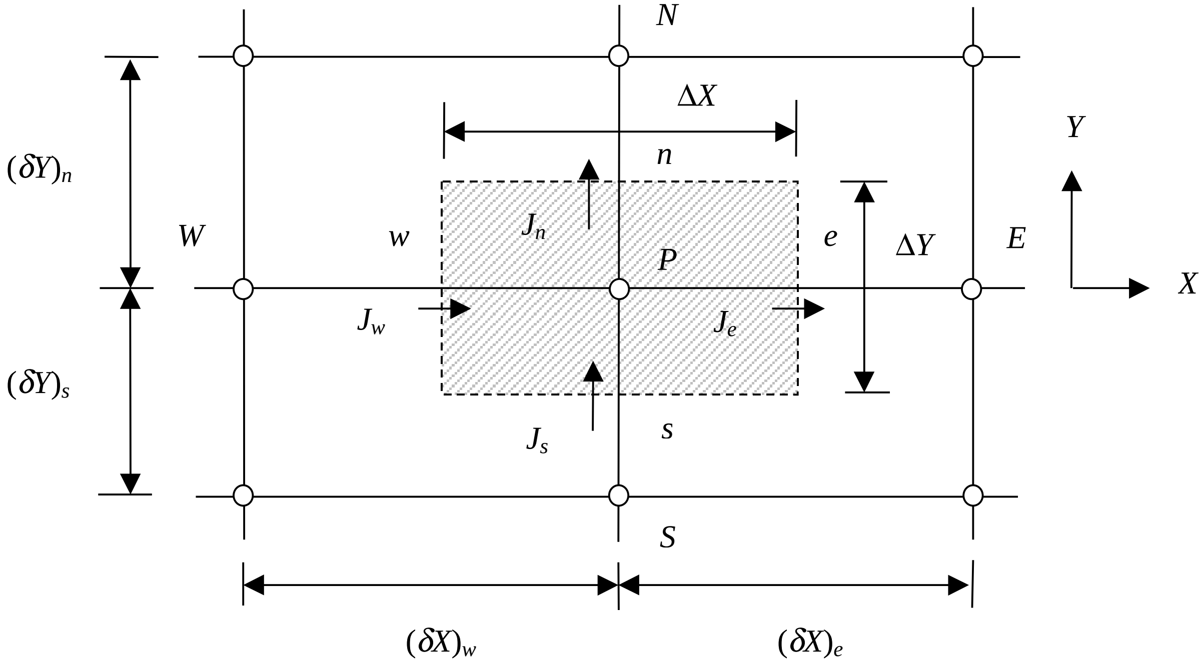

Fig. 3-1 Control volume and grid nodes

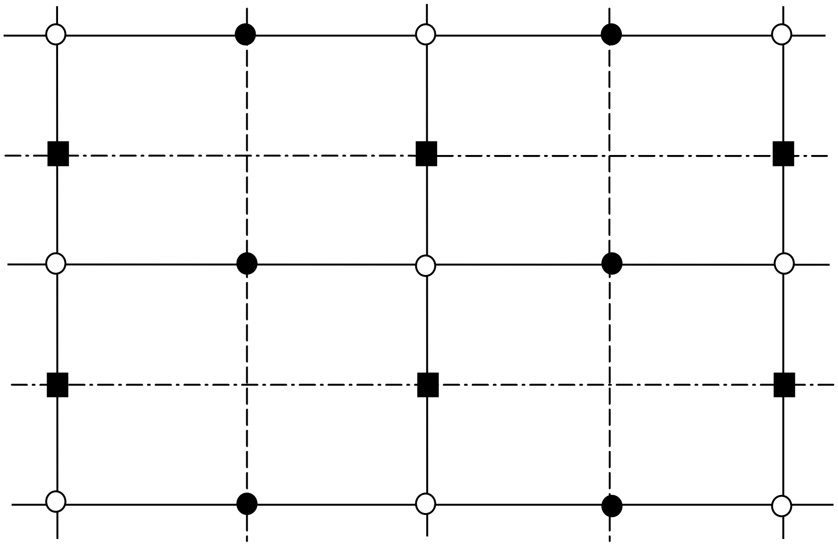

Fig. 3-2 Staggered grids

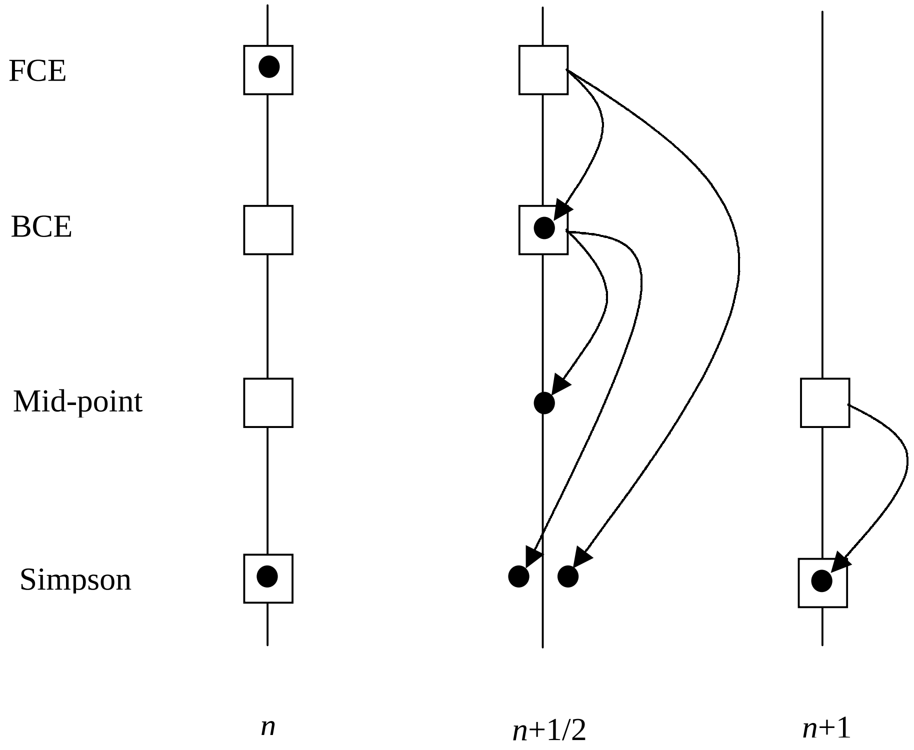

Fig. 3-3 Diagram for the 4th order Runge-Kutta method

CHAPTER 4❶

CHARACTERISTICS OF PARTICLE MOTION IN A SLIDER DISK INTERFACE

4.1 Introduction

Particle contamination on the slider is one of the major issues in the contamination of hard drives. Previous studies showed that particles often accumulate on the surfaces of rail tapers, surfaces of rails at the trailing edge and upper surfaces of cavities. These kinds of contamination are mainly contributed by the particles suspending in the air. Therefore, it is necessary to know how they move and where they go in a SDI if we want to study the mechanism of the contamination.

In the following analysis, we focus our study on the paths of a single particle moving in a SDI, so to investigate what causes them to go to the observed contamination zones mentioned above. Since the interaction of a particle with a slider surface or a disk surface is a very complicated process, we will not discuss it in this thesis and will do it in a future work. The model used in the following analysis is that presented in the Chapter 2. It is solved by two steps: velocity field solution and particle motion solution. The velocity field of the SDI is calculated by the CML Air Bearing Simulator (Lu, et al., 1995), in which Partanka's control volume method combined with a multi-grid control volume is used to solve the Reynolds equation. With the velocity field known, the particle motion

---

❶ Part of this chapter has been published in Zhang, et al. (1997c).

equations are solved using a fourth order Runge-Kutta method. All these methods have been experienced in the Chapter 3.

4.2 Effects of the Saffman Force on the Motion of Particles

We will see later that the Saffman force is important only for the relatively large particles. Therefore, to study the effects of the Saffman force, we need only consider those particles moving in a recessed region. To study the characteristics of particles moving in a recessed region, one encounters the problem of how to treat the irregular surfaces of the sliders, which usually cause complicated flow in the region. Since we are only interested in the motion characteristics of the particles, we can consider a simple slider which causes a simple flow close to that in a recessed region of a real slider. For convenience, we adopt an "infinitely wide, no-rail slider" with some parameters fixed close to those of a recessed region, for example, with $h_m = 3.05\mu m$, l=2.05 *mm*, pitch angle=150 μrad. The reason for taking $h_m = 3.05\mu m$ is that the recessed height is usually about 3 μm for a real slider and the flying height is about 50 *nm*. Using the CML Air Bearing Simulator, we obtain the pressure profile for this case, which is shown in Fig. 4-1.

4.2.1 Effects of Particle Sizes

From equation (2-18), we know that the Saffman force is sensitive to the particle size because its magnitude is proportional to the square of the particle radius. In this case, we simulate four particles with the same density of $\rho_p = 8000$ kg/m_3 and different diameters of 200 *nm*, 300 *nm*, 330 *nm*, and 340 *nm* respectively. All of them enter the recessed region with initial velocity of U_{p0} =1 and initial vertical position of Z_{p0}=0.2. The simulation results are shown in Fig. 3-2.

The particles with the given initial velocity usually move faster than that of the air flow in the recessed region, which makes the Saffman force point to the slider. It is seen that all four particles, which are acted by the upward Saffman force, go up when they enter the recessed region. The particle with d = 200 *nm* rises only a small distance and then goes almost parallel to the disk surface, while the particle with d = 340 *nm* goes up sharply and hits the surface of the slider. This implies that the Saffman force has a more significant effect on the motion of large particles.

In our previous studies (Zhang and Bogy, 1996), we assumed that the motion of small particles (<100 *nm*) was two dimensional, or planar. Based on the current simulation results, we see that this assumption is reasonable, because the lift force has little effect on the motion of small particles in a SDI. Another interesting phenomenon is that the particles have sharp upward motion when they just enter the recessed region, and then move smoothly after a short time except for particle 4, which hits the surface of the slider. The reason for this may be that the magnitudes of the relative velocity (relative to the airflow) of the particles are very large at the entrance, which affects the Saffman lift force significantly.

4.2.2 Effects of the Relative Velocity

From Saffman's analysis (Saffman, 1965), we know that the direction of the Saffman force depends on the direction of the velocity gradient and the sign of the relative velocity of the particle with respect to the airflow. For the fixed velocity gradient such as the case in our study, the direction of the Saffman force points to the slider if the particle moves faster than the airflow, or points to the disk if the particle moves slower than the airflow. To study the effects of the relative velocity, we simulate four particles with the same diameter d=340 *nm* and density ρ_p=8000 kg/m^3 but with different initial velocities of U_{p0}=0.2, 0.4, 0.6, 0.8. The simulation results are shown in Fig. 4-3.

It is seen that the particle with high (or low) initial velocity, which implies large magnitude of relative velocity, goes up (or down) sharply when it enters the recessed region. The larger the magnitude of the relative velocity, the more sharply the particle moves up or down.

Note that a particle usually has a large magnitude of relative velocity when it just enters the recessed region. Afterwards, it is accelerated or decelerated by the action of the drag force and moves gradually close to the velocity of the local air flow. In other words, its magnitude of relative velocity gradually decreases towards zero. Since the airflow for a real slider usually has lower velocities in a recessed region, the relative velocities of particles have positive signs. Therefore, the particles entering it are acted on by an upward Saffman force to bring them to the slider surface. Thus, it is predicted that contamination should occur at the corners between the rail and the upper surface of the recessed region. As mentioned, this is often observed.

A similar situation occurs for the particles entering the air bearing under a taper. For this case, the Saffman force also gives a strong lift. This, at least partially, explains why the contamination easily concentrates on tapers.

4.2.3 Effect of Particle Density

To study the effects of the particle density, we simulated four particles with densities of 2000, 4000, 6000 and 8000 kg/m^3. All of them have the same diameter of 340 *nm*, and they enter the recessed region with the same initial velocity of $U_{p0} = 1$ at the same initial height of $Z_{p0} = 0.2$. The simulation results are shown in Fig. 4-4.

It is seen that the particles with larger density go up more sharply than those with lower density. In other words, the Saffman force has a more significant effect on the vertical motion of a particle with higher density. This phenomenon is actually the result of the fact that the relative velocity makes a significant contribution to the Saffman force. Note that a particle usually has a large magnitude of relative velocity when it just enters the recessed region. If its density is very small, the drag will have strong effects to cause the particle to reach the velocity of airflow quickly (see (2-16)~(2-17)), or the relative velocity goes to zero rapidly. Under such a situation, only during a short time does the Saffman force show large values to push the particle up or down. But if the density is high, the inverse results occur. To check this mathematically, we artificially divided the drag terms in equations (2-16)~(2-18) by 3 and simulated the cases with the same given conditions as mentioned above. The simulation results are shown in Fig. 4-5.

It is clear that the particle shows close paths for different densities this time, which is much different from the case with the original drag. Also, the particle goes up more sharply for the lower density instead of the higher density as in the original case. This implies that the smaller drag forces make the Saffman lift force contribute more to the vertical motion of the particle.

4.3 Planar Motion of Small Particles in a SDI

In this section, we focus our study on the small particles which can move in an air bearing. We know that the Saffman force is negligible for the small particles, therefore their motion can be regarded as planar. For convenience, we choose a 50% slider ($2mm\times1.6mm$) as an example in the analysis. The slider has a recess depth of 3 μm and taper length and angle of 0.2 mm and 0.01 *rad*, respectively, and is loaded by 3.5 *g*. Except for some specially denoted cases, the slider is assumed to fly at the position r=23 *mm* from the center of the disks while the disk rotates at 5400 *rpm*. The slider rails (shaded) are shown in Fig. 4-6. Its air bearing pressure profile is shown in Fig. 4-7 and its major flying characteristics are given in Table 4-1.

Table 4-1. Flying Characteristics

Position *r* (*mm*)	Skew (degree)	Pitch (μ *rad*)	Roll (μ *rad*)	FH-CTE[✝] (*nm*)
23	0.0°	188.2	0.0	34.2

✝Flying height at the central trailing edge

4.3.1 Effects of the Particle Density

To study the effects of the density, we consider these quite different values: ρ_p=1000 and 8000 kg/m^3. The diameter of the particle is chosen to be 30 *nm*, and the initial velocities are $U_{p0} = 1$ and $V_{p0} = 0$. Seven particles enter the interface from the leading edge. The simulation results are shown in Fig. 4-8, where solid lines denote the particle paths for ρ_p=1000 kg/m^3 and dashed lines denote the particle paths for ρ_p=8000 kg/m^3. It is seen that the particle paths coincide for particles with different densities. This fact implies that the density does not influence the particle motion significantly if the particle size is small and the density varies in a practical range.

4.3.2 Effect of the Initial Velocity

We also choose seven particles in this case, each with density ρ_p = 8000 kg/m^3 and diameter d = 30 nm , entering the interface of the slider from the leading edge as shown in Fig. 4-9. For each particle, we assign two different initial velocities (U_{p0} , V_{p0}) = (1, 1) and (0, -1), respectively. It is seen that the particle paths change slightly with the variation of the initial velocities. Only when the particles reach the central rail at the trailing edge do the paths depart a significant amount. This implies that the variation of initial velocity affects the particle paths more than the variation of the density within a practical variation interval. But generally, its affect is still weak for small particles, even if the particles have significant differences in U_{p0} and V_{p0}.

4.3.3 Effects of Particle Size

At the beginning of this section, we mentioned that we would focus our studies on small particles (say 30 nm) because we are only interested in particles that can go through the air bearing. However, for some special cases, for instance those particles moving in the recessed regions, it is desirable to consider larger particles. Note that we keep the $d \leq 200$ nm so we can ignore the effect of Saffman force in the analysis. We do not treat the effects of collisions of the particle with the surfaces of the slider. Therefore, the calculation is stopped when the particle hits the rails.

Figures 4-10 and 4-11 show the effects of density with different particle sizes. In Fig. 4-10, the particle diameter is chosen to be d = 30 nm and the initial velocity is U_0 = 1, V_0 = 0. It is seen that the paths of particles with ρ_p = 1000 and 8000 kg/m^3, which are denoted by solid lines and dashed lines respectively, show little difference for this diameter. In Fig. 4-11, we changed the particle diameter to d = 200 nm and kept the same initial velocities. This time, the particle paths for ρ_p = 1000 and 8000 *kg/m*^{3} show obvious differences as compared to the case with d = 30 *nm*. This implies that inertia plays a more significant role in the particle motion for larger particles. Similar results can be seen for changing the initial velocities with different particle sizes in Figs. 4-12 and 4-13, which show the results for d=30 and 200 *nm*, respectively. For each particle size, two initial velocities are used, that is, (U_0 , V_0) = (1, -1) and (0, 1). The density is chosen as ρ_p=8000 *kg/m*^{3} for both cases. The paths of particles show little difference for different U_0 and V_0 for d=30 *nm* (Fig. 4-12). But for d = 200 *nm*, their paths show significant difference for different U_0 and V_0. Therefore, the variation of the initial velocity will have an important effect on the particle motion for large particles.

4.3.4 Particle Paths and Streamlines

Seven particles, each with diameter d=30 *nm*, density ρ_p=4000 *kg/m*^{3} and initial velocities $U_0 = \hat{U}$ and $V_0 = 0$, enter the SDI from the leading edge in this case (Fig. 4-14). The particle paths are drawn in wide lines to be distinguished from thin lines that represent the "stream lines" of the air flow. Here, the "stream lines" are drawn based on stream functions defined by (3-25) and (3-26). It can be seen that the streamlines are relatively dense in the recessed regions. This is because the mass flow rate is much higher due to the large spacing in the recessed regions. It is also shown that the streamlines in the recessed regions largely follow the contour of the rail shape, because only a small portion of the flow can squeeze into or out of the bearing area. Looking at particle paths, we see that all particles follow the streamlines very well, and most of them leave the SDI from the sides for this slider. This provides an idea to design a slider for reducing the particle contamination, which will be presented in the next chapter.

4.4 Summary

We studied the characteristics of the particles moving in a SDI by considering various forces acting on them. Through simulations for various cases, we obtained the following results:

(1) Particle size is an important parameter affecting the Saffman force. For a small particle ($d \leq 200$ *nm*), Saffman force is relative small and can be neglected;

(2) The magnitude of the relative velocity affects the Saffman force, or vertical motion of a particle, significantly. Since the air flow has a lower velocity in the recessed region, the relative velocity usually has a large magnitude with positive sign when a particle enters it, which causes a relatively strong Saffman force pointing to the slider. Therefore, the corners between the rail and the upper surface are likely to attract the particles that result in the contamination. Similarly, the contamination on tapers is caused, at least partially, by the large relative velocity of the particles entering the air bearing under the tapers;

(3) The particles with higher densities go up or down more sharply than the particles with lower densities. This is because the larger density will reduce the contribution of the drag to the motion of the particle, so as to make particles move with a high magnitude of relative velocity (or high Saffman force) during a longer time;

(4) Small particles follow the streamlines very well. The inertia effect increases with the increase of the particle sizes.

(5) For some specific slider designs, more particles leave the SDI from sides instead of from the trailing edge.

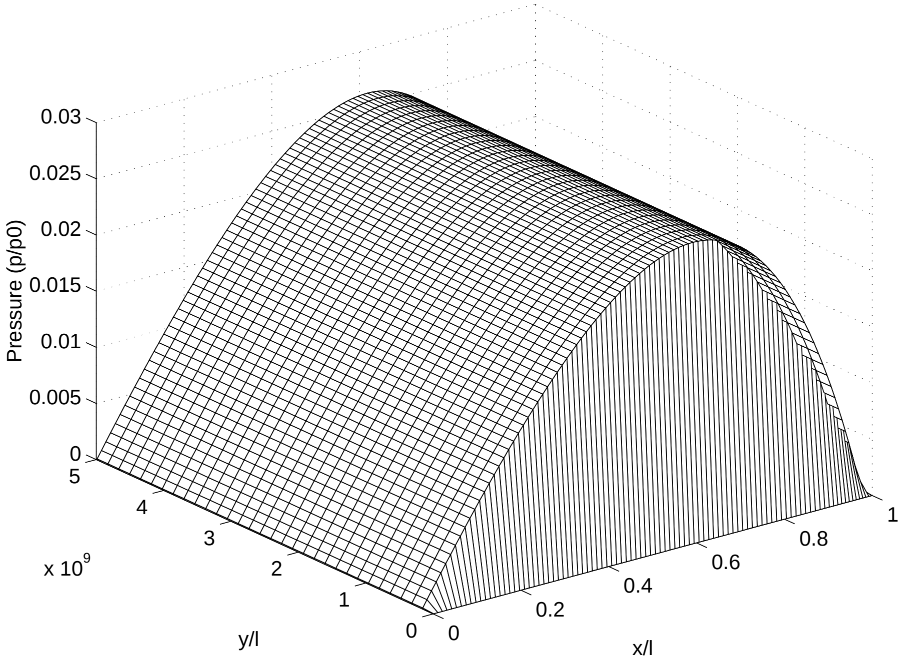

Fig. 4-1 Pressure profile of the 2-D SDI

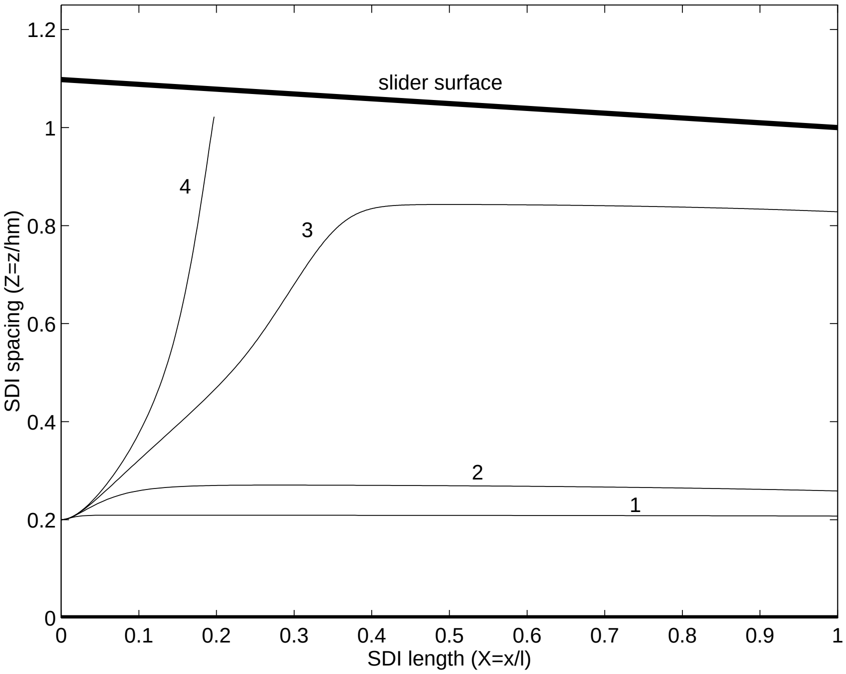

Fig. 4-2 Effects of the particle sizes on the vertical motion of the particles: 1–*d*=200 *nm*; 2–*d*=300 *nm*; 3–*d*=330 *nm*; 4–*d*=340 *nm*.

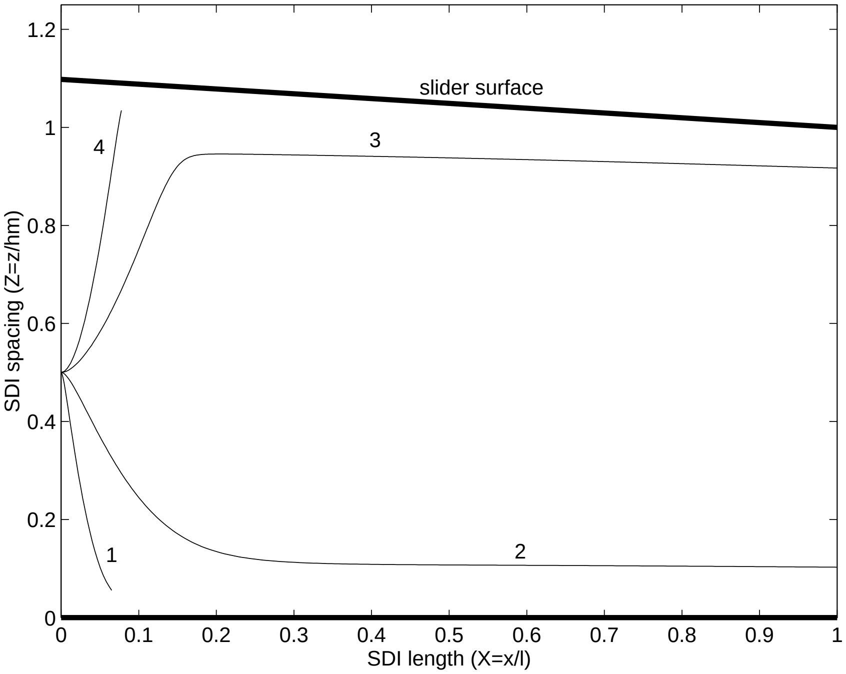

Fig. 4-3 Effects of the initial velocity (or relative velocity) on the vertical motion of the particles: 1–U_{p0}=0.2; 2– U_{p0}=0.4; 3– U_{p0}=0.6; 4– U_{p0}=0.8.

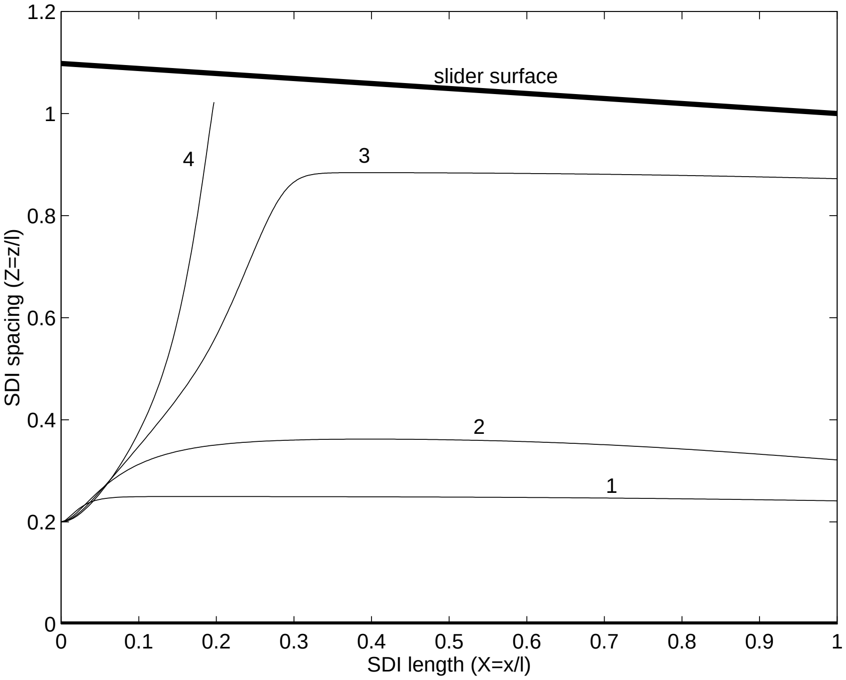

Fig. 4-4 Effects of the particle density on the vertical motion of the particles: 1–ρ_p=2000 kg/m^3; 2–ρ_p=4000 kg/m^3; 3–ρ_p=6000 kg/m^3; 4–ρ_p=8000 kg/m^3.

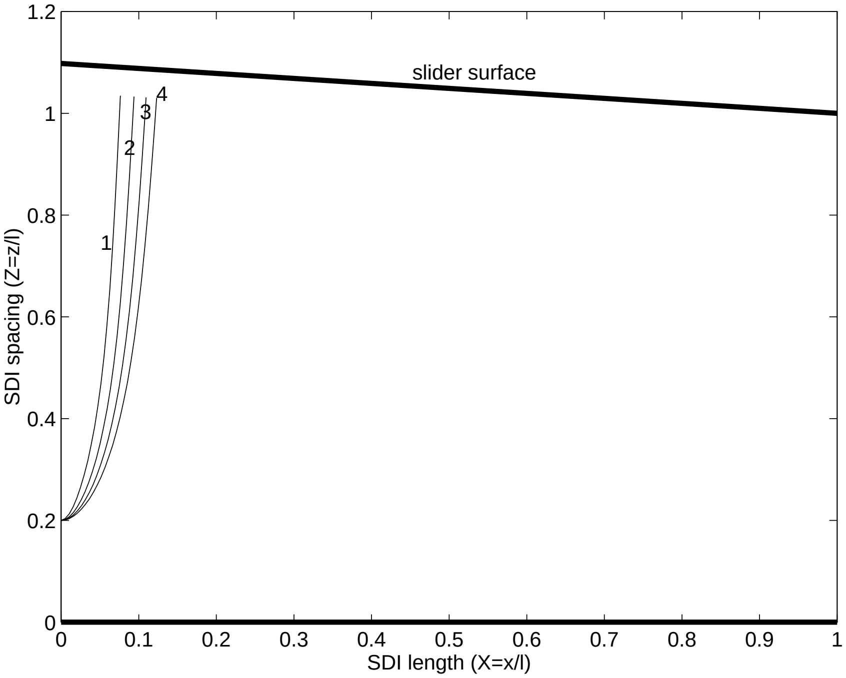

Fig. 4-5 Effects of the particle density on the vertical motion of the particles by "1/3 reduced drags": 1–ρ_p=2000 kg/m^3; 2–ρ_p=4000 kg/m^3; 3–ρ_p=6000 kg/m^3; 4–ρ_p=8000 kg/m^3

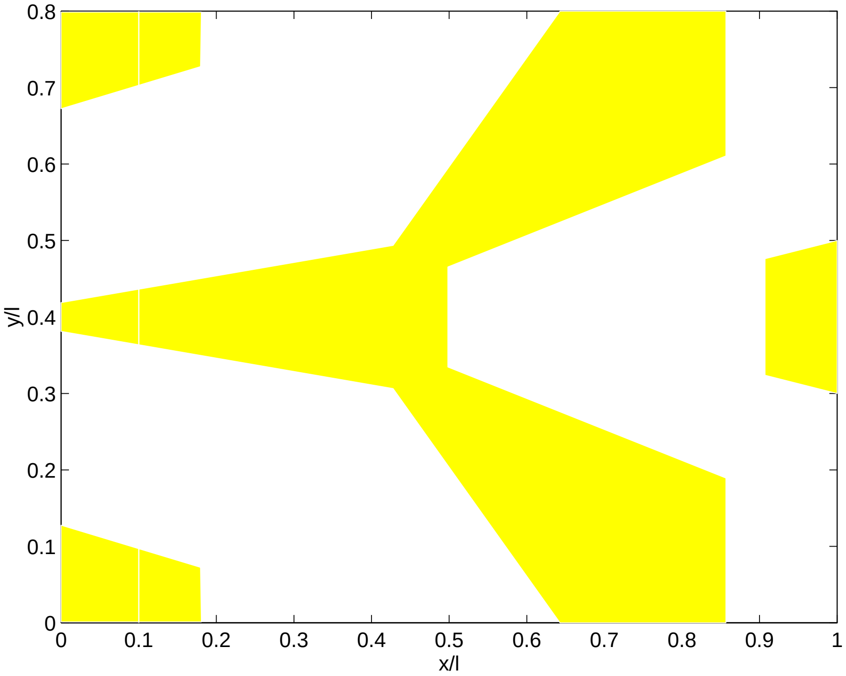

Fig. 4-6 Rail shape of a sample slider

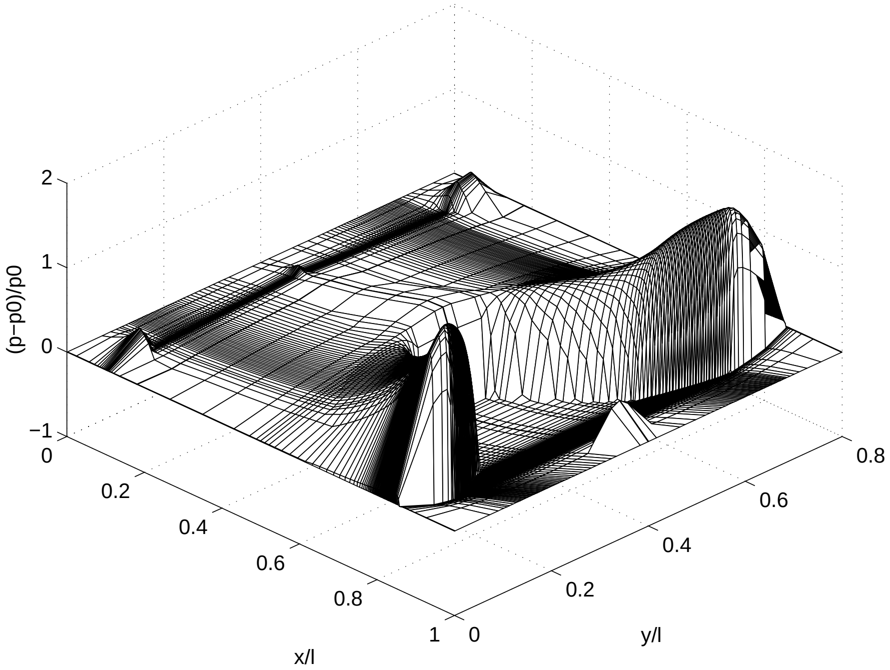

Fig. 4-7 Pressure profile of the air bearing for the sample slider

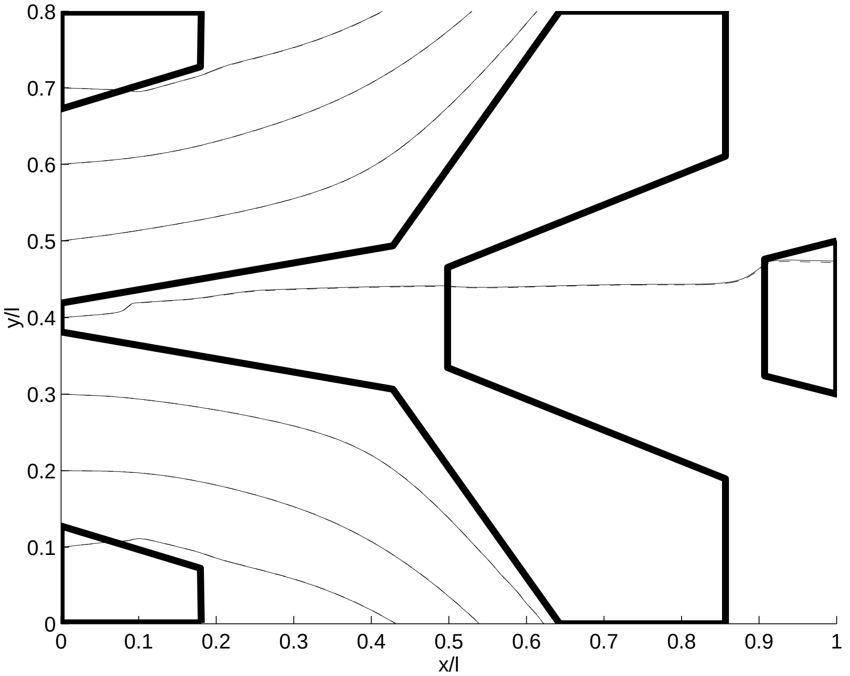

Fig. 4-8 Effects of the particle density on the particle paths: 1–ρ_p=1000 kg/m^3; 2-- ρ_p=8000 kg/m^3

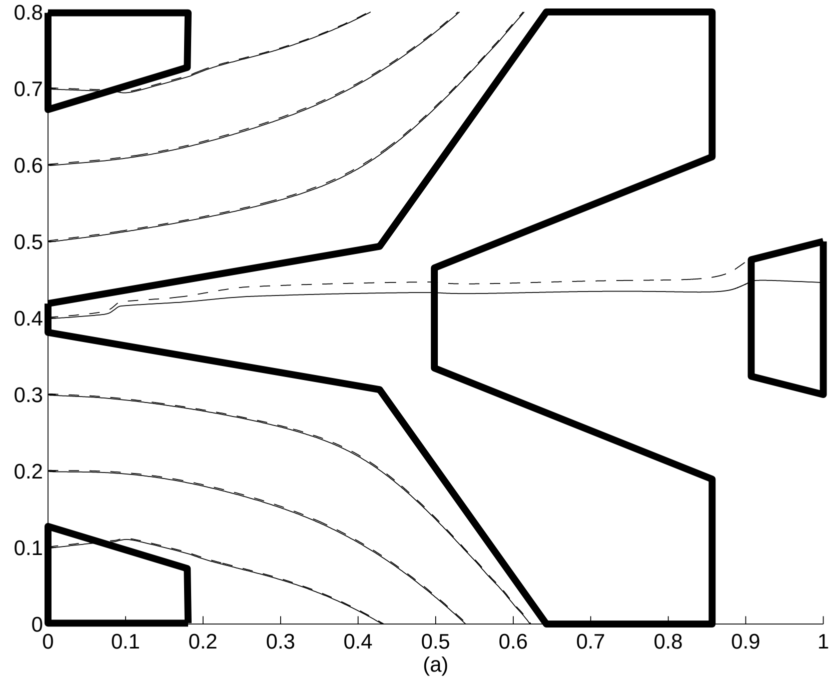

Fig. 4-9 Effects of the initial velocities on the particle paths: 1–(U_{p0}, V_{p0})=(1,-1); 2--(U_{p0}, V_{p0})=(0,1)

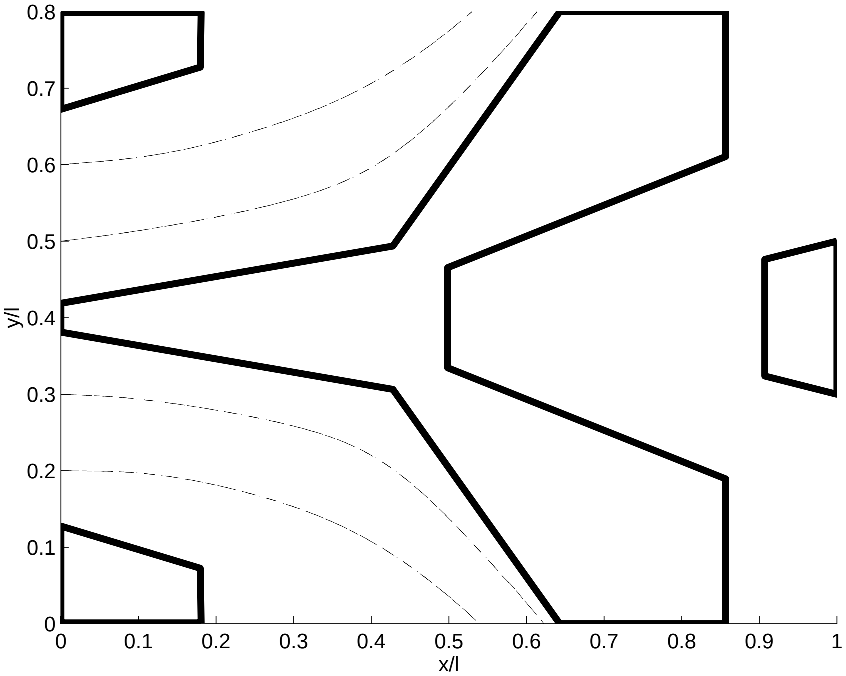

Fig. 4-10 Effects of the particle density on the particle paths (d=30 nm): 1–·ρ_p=1000 kg/m^3; 2--ρ_p=8000 kg/m^3

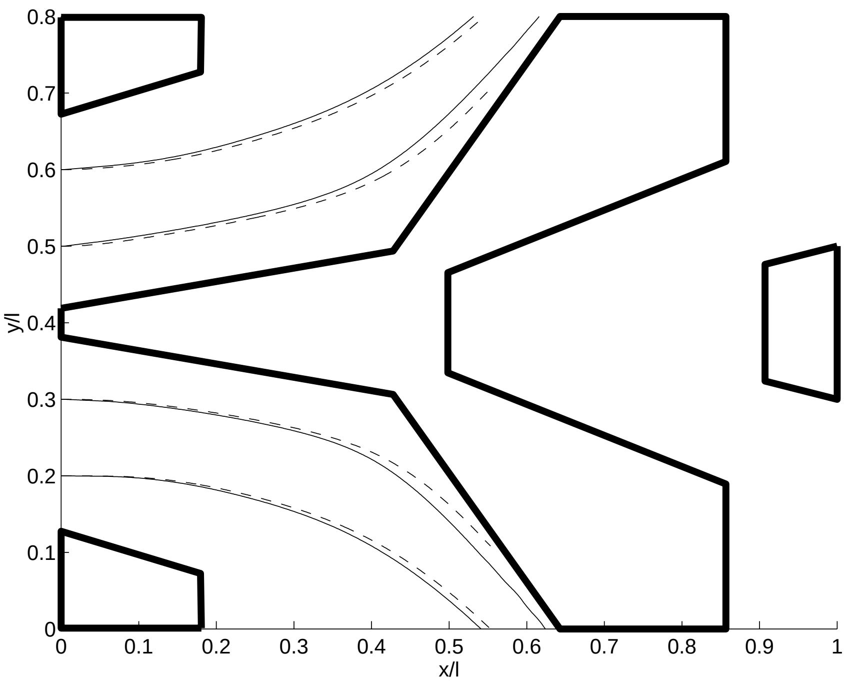

Fig. 4-11 Effects of the particle density on the particle paths (d=200 nm) : 1–ρ_p=1000 kg/m^3; 2--ρ_p=8000 kg/m^3

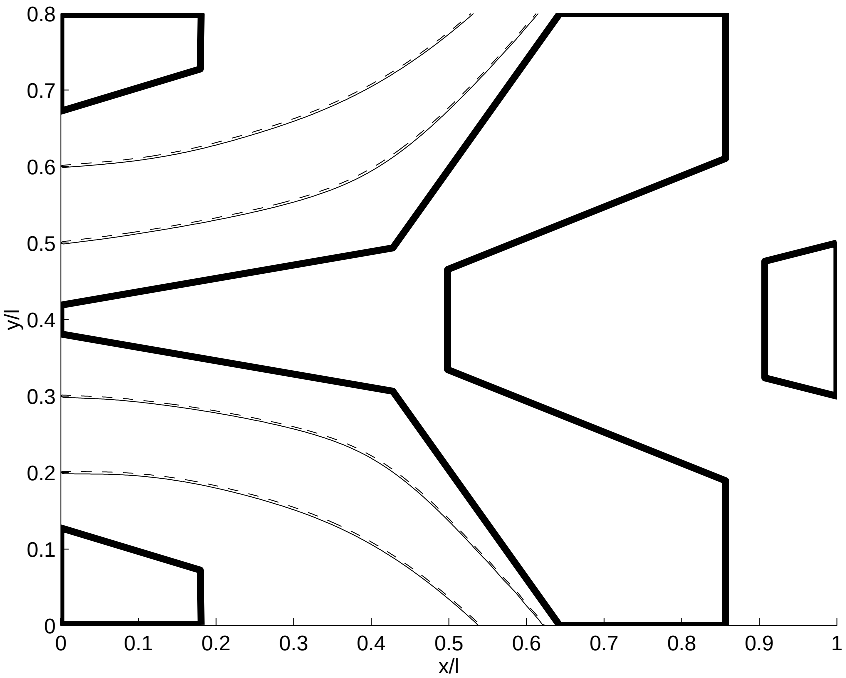

Fig. 4-12 Effects of the initial velocity on the particle paths (d=30 nm): 1–(U_{p0}, V_{p0})=(1,-1); 2--(U_{p0}, V_{p0})=(0,1)

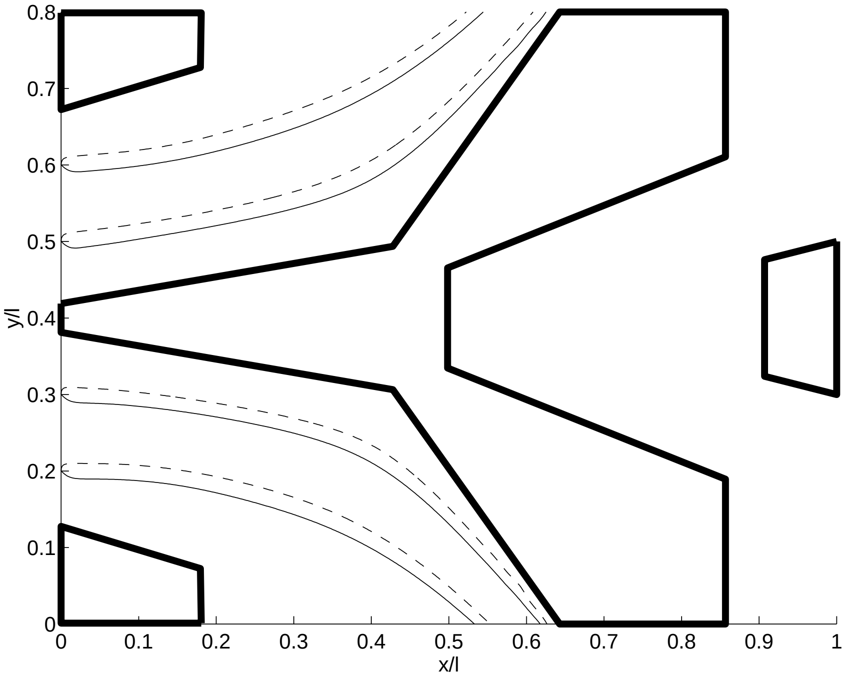

Fig. 4-13 Effects of the initial velocity on the particle paths (d=200 *nm*): 1‒(U_{p0}, V_{p0})=(1,-1); 2--(U_{p0}, V_{p0})=(0,1)

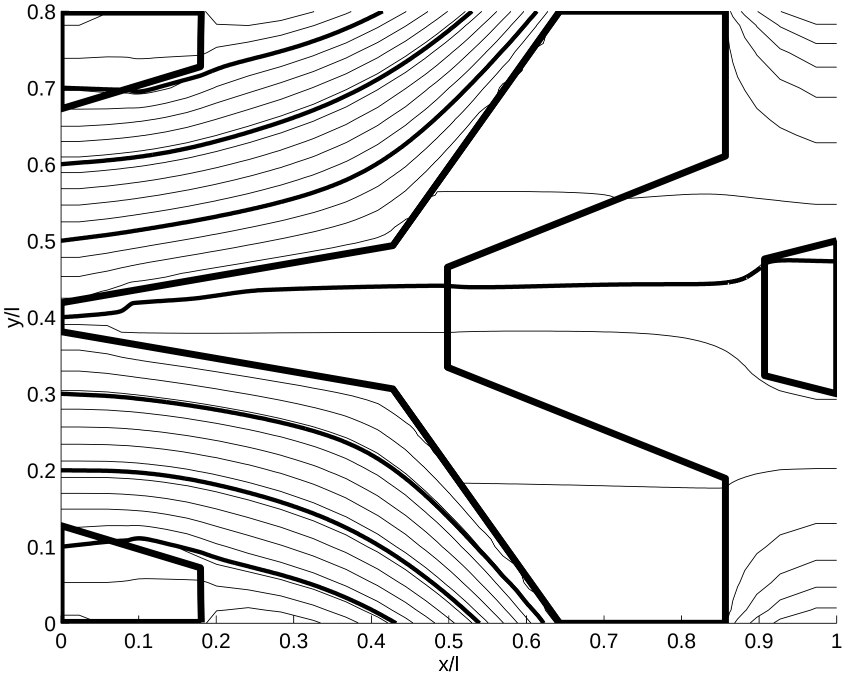

Fig. 4-14 Particle paths vs. streamlines for the sample slider

CHAPTER 5❶

SLIDER DESIGNS FOR CONTROLLING PARTICLE CONTAMINATION

5.1 Introduction

Previous studies by other researchers (Hiller, et al. 1991; Koka, et al., 1991) showed that the taper surface at the trailing edge and the rail surface at the trailing edge are the two main zones for producing contamination on a slider. The latter plays a key role because it not only collects particles itself, but also indirectly contributes to the particle deposition on the taper surfaces. An efficient way of reducing the particle contamination is to reduce the contamination on the rail surfaces at the trailing edge, which also helps to reduce the particle contamination on the taper surfaces simultaneously. A strategy for realizing this is to find ways to make as many particles as possible leave the SDI from its two sides instead of from the trailing edge. Seen from another perspective, this strategy is reasonable for reducing particle contamination because if we can make most of the particles leave the SDI from the sides, we actually reduce the time for them to stay in the SDI. The less time a particle spends in an air bearing, the less chances there are for it to be deposited on the slider.

From Chapter 4, we know that the small particles that can move in an air bearing follow the streamlines very well. This suggests the use of the airflow in a SDI to blow the particles out from its sides, which we call the “inherent cleaning process” or “self

---

❶ Part of this chapter has been published in Bogy, et al. (1996).

cleaning process”. Note that we already have such a slider design (Fig. 4-6) with this required property (Fig. 4-14). The characteristic of this slider is that it has two small rails at the leading corners and one large rail at the center. The main advantage of these two small rails is they construct two “channels” together with the central rail to produce the airflow in the SDI to “lead” particles out of the SDI from the two sides. In addition, their existence also provides two tapers that are beneficial to the taking off of the slider and increases the flying stability. The rail at the trailing edge provides a “secondary channel” with two ends of the central rail, which has a similar function as the “first channel”. Clearly, most of the particles entering into the SDI from the leading edge leave it from its sides for this special design (Fig. 4-14), which is what needed for reducing the particle contamination.

In this chapter, we will make a detailed analysis of this design and explain its properties. Since we are only interested in the small particles that can move in air bearings, we neglect the lift force and gravity force in the simulation. For convenience of illustration, we call our sample slider (Fig. 4-6) “Sample-I”, which distinguishes it from the modified designs later. We also choose a tri-pad slider and study the motion patterns of particles in its SDI, and compare its results with those of our sample sliders. We will also explain how to improve the design to make it more efficient for reducing particle contamination.

5.2 Slider Designs for Controlling Particle Contamination

5.2.1 Effects of the Rail Shapes

For the convenience of comparison, we choose a 50% design for both the tri-pad slider and Sample-I slider. Both have the same taper angle and length of 0.01 *rad* and 0.2 *mm*, and recess depth of 3 μm. They fly at the radial position of 23 *mm* (MD) from the center of the disks while the disks rotate at 5400 *rpm*. The rail shapes are shown in Fig. 5-1 and the pressure profiles are shown in Fig. 5-2. Their flying characteristics are shown in Table 5-1.

Table 5-1. Flying Characteristics of the Tri-pad and Sample-I Sliders

	Position (*mm*)	Skew (degree)	Pitch (μ rad)	Roll (μ rad)	FH-CTE (*nm*)
Tri-pad	23	0.0	210.6	8.6	33.8
Sample-I	23	0.0	188.2	2.1	34.2

Figure 5-3 shows the comparison of particle paths for the two designs. For both cases, we place seven particles of diameter 30 *nm*, initial velocity $\hat{U}$ (or U_{p0}=1) in the x direction and density 4000 kg/m^3 along the leading edges. It is seen that all particles move through the SDI and leave it from the trailing edge for the tri-pad slider (Fig. 5-3(a)), which provides more chances for the particles to be deposited on the slider surface. For the Sample-I slider, it is seen that most of the particles are blown out of the SDI from the two sides (Fig. 5-3(b)). Therefore, less particles have chances to deposit on the rail surface at the trailing edge and less time is spent for most of particles in the SDI. All of these are regarded as beneficial to the reduction of the particle contamination.

The Sample-I slider is not perfect in that there is one particle passing through the air bearing of the rail at the trailing edge (Fig. 5-3(b)), which may increase the probability for it to deposit there. As a improvement, it is suggested to sharpen the leading edge of a rail or broaden the back corners of a rail to make the airflow more smoothly carry the particles out of the SDI. Following this strategy, we designed a new slider based on the Sample-I slider and we call it the Sample-II slider. The rail shape and pressure profile of the Sample-II are shown, respectively, in Fig. 5-4 and Fig. 5-5, and its flying characteristics are given in Table 5-2. The flying height of the new slider is close to the two old ones.

Table 5-2. Flying Characteristics the Sample-II Slider

Position r (mm)	Skew (degree)	Pitch (μ rad)	Roll (μ rad)	FH-CTE (nm)
23	0.0°	266.4	8.9	31.3

We also place seven particles, all having the same diameter of d=30 nm and density of ρ_p=4000 kg/m^3, along the leading edge. The initial velocities for these particles are given by $U_{p0} = 1$ and $V_{p0} = 0$. Since the particles may enter the interface from the two sides when the slider moves radially over the disk, we also put seven particles at each side and give them a non-zero V_{p0}, that is, $U_{p0} = 1$ and $V_{p0} = 0.5$ for those from the inner side, and $U_{p0} = 1$ and $V_{p0} = -0.5$ for those from the outer side.

Obviously, most of particles entering the interface from the leading edge leave the interface from the two sides. The particles starting from the two sides have less chances to go a long distance in the interface. The particle from the central leading edge goes through the interface and leaves the trailing edge by passing around the end rail instead of going through the air bearing under it as in Fig. 5-6. This demonstrates the advantage of the modified slider.

5.2.2 Effects of the Slider Position (ID or OD)

We know that small particles follow the streamlines very well. If the flow field changes, for instance when the slider moves to the OD or ID resulting in a non-zero skew angle, how will the motion of the particles be affected? Is the Sample-II slider still good for reducing the particle contamination? To study the effects of the slider position, we examine two cases for the Sample-II slider, at the ID with *r* = 15 *mm* and skew = –7.5° and at the OD with *r* = 31 *mm* and skew = 7.5°. Here, the minus sign corresponds to the case when the flow comes from the outer leading edge towards the inner trailing edge. The flying characteristics for the two cases are shown in Table 5-3.

Table 5-3. Flying Characteristics for the Sample-II Slider at ID and OD

Position *r* (*mm*)	Skew (degree)	Pitch (μ rad)	Roll (μ rad)	FH-CTE (*nm*)
15	–7.5°	475.5	9.8	40.8
23	0.0	266.4	8.9	31.3
31	7.5°	98.4	6.5	20.1

The particles simulated for both cases are the same as in the section 5.2.1 except for the particle size which we take as *d* = 20 *nm* for the ID case and 30 *nm* for the OD case, because we want the particle size to be consistent with the flying height at the central trailing edge. As in the last case, seven particles are placed along the leading edge and each of the two sides. The simulation results are shown in Figs. 5-7 and 5-8. For both cases, most of particles from the leading edge leave the interface from the two sides, which is qualitatively the same as the MD case. For particles from the inner or outer side, one more particle, compared with the MD case in Fig. 5-6, enters the interface from positions close to the trailing edge. Since this particle travels a short distance through the recessed region at the end corners, it has less chance to deposit on the end rail than those that enter the interface from the leading edge and leave from the trailing edge through or close to the air bearing under the end rail. Therefore, the Sample-II slider still retains its advantage for reducing particle contamination at the ID and OD.

5.3 Optimal Design

Flying stability is an important consideration in slider designs for proximity recording. One requirement in stability design is to reduce the flying height variation for the slider across the radius of a disk. From Table 5-3, we see that the Sample-II slider can not meet this requirement satisfactorily. Since the flying characteristics are significantly affected by the air bearing surface, we can optimize a slider design by changing the geometry of its air bearing surface to make it be much less sensitive to changes in radius. This work can be done by using the CML Air Bearing Optimization Program (O’Hara, et. al., 1995).

The objective function of this problem is to minimize the difference in flying height over the radius of the disk. The simulated annealing method is employed as explained the optimization algorithm (O’Hara, et al., 1996). This technique minimizes the expense of calculating derivatives in gradient-based optimization algorithms and handles the high number of parameters efficiently. Additionally, it can achieve globally optimal solutions for multi-term objective functions. The optimization of the Sample-II slider was performed by Mathew O'Hara, and the result is given here. We call the optimized shape the Sparrow slider. Figure 5-9 shows its rail structure and Fig. 5-10 shows the pressure profile of its air bearing at the MD. Its flying characteristics are shown in Table 5-4. Clearly, the flying height difference across the disk radius for the Sparrow slider is much less that for the Sample-II slider (Table 5-3).

Table 5-4. Flying Characteristics of the Sample-II Sliders

Position r (mm)	Skew (degree)	Pitch (μrad)	Roll (μrad)	CTFH* (nm)
23.0	0.0	255.0	2.7	28.0
31.0	–7.5	313.0	–32.0	22.0
15.0	7.5	178.0	33.0	27.4

To study the characteristics of the particle motion in the SDI of the Sparrow slider, we placed seven particles with d=22 nm, ρ_p=4000 kg/m^3 and U_{p0}=1 and V_{p0}=0 along the leading edge for the MD case. The results (Fig. 5-11) show that most of the particles leave the SDI from the sides, which is beneficial to the reduction of the particle contamination.

The particle paths are also simulated for the OD and ID cases. Figure 5-12 shows the OD case for skew=7.5° and radial position r=31 mm, and Fig. 5-13 shows the ID case with skew=–7.5° and radial position r=15 mm. Seven particles with d=20 nm enter the SDI from the leading edge and each of the two sides. It is seen that most of the particles from the leading edge leave the SDI from the sides. Two of them, together with some from the two sides, leave the SDI from the trailing edge by passing around the rail there. Therefore, the characteristics of reducing contamination for the Sparrow slider still remains for the OD and ID cases.

5.4 Summary

A strategy for reducing the particle contamination on a slider is to make as many particles as possible leave the SDI from its sides, instead of leaving the SDI from the trailing edge. This not only may reduce the particle contamination on the surface of the trailing edge rail and tapers, but also reduces the time for a particle to stay in a SDI, which in turn reduces the probability for the particle to deposit on the slider surface. Since the particles suspending in the air are one of major sources causing the contamination, it may be helpful to employ the airflow in the SDI to blow the particles out of it from the two sides, which we call “inherent cleaning” or “self cleaning”. This strategy may be realized by specially designing the geometry of the air bearing. Through simulating various cases, we designed some sliders that have the desired characteristics. After the optimization calculation, we designed a sparrow-like slider that not only has the anti-contamination characteristics, but also has good performance in flying stability across the radius of the disk.

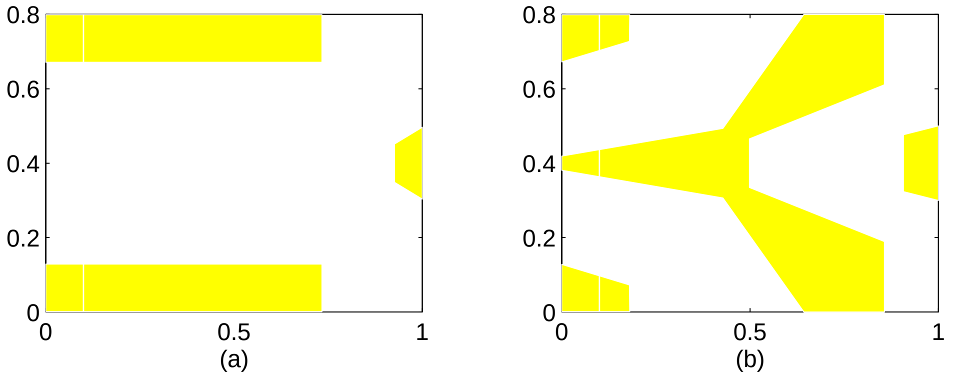

Fig. 5-1 Rail shapes for the Tri-pad and Sample-I sliders: (a) tri-pad; (b) sample-I

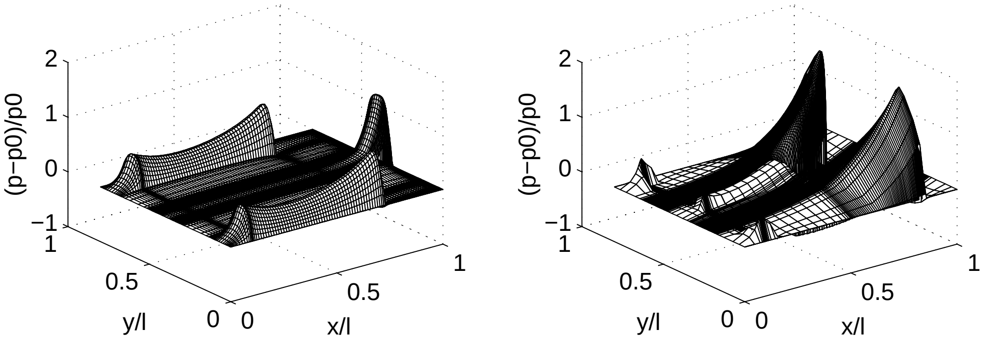

(a) (b)

Fig. 5-2 Pressure profiles for the Tri-pad and Sample-I sliders: (a) tri-pad; (b) sample-I

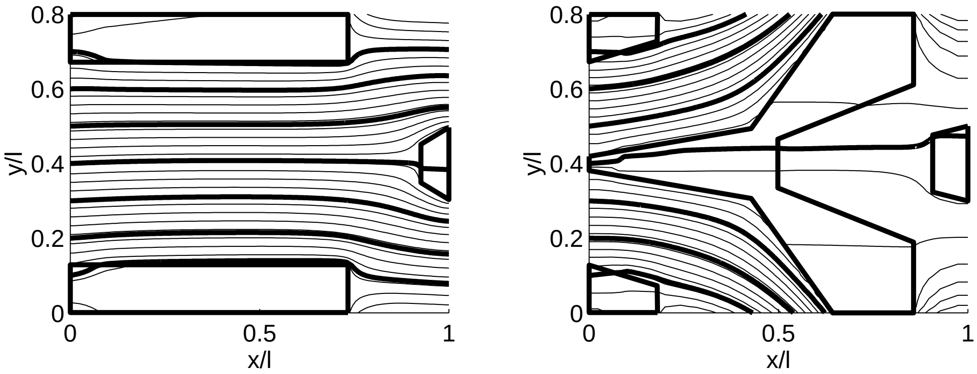

(a) (b)

Fig. 5-3 Comparison of the particle paths in the SDIs of Tri-pad and Sample-I sliders: (a) tri-pad; (b) sample-I

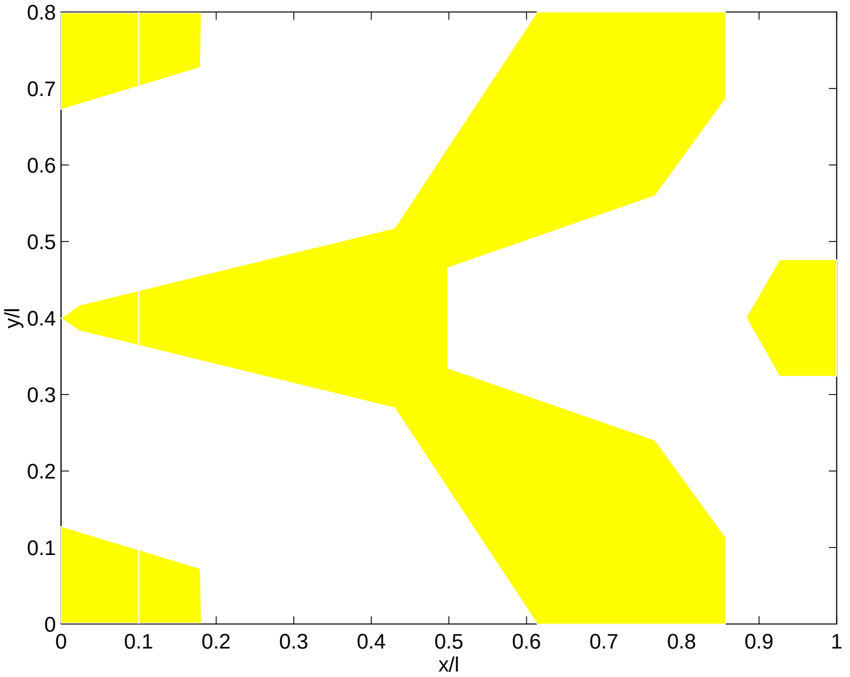

Fig. 5-4 Rail shape of the Sample-II slider

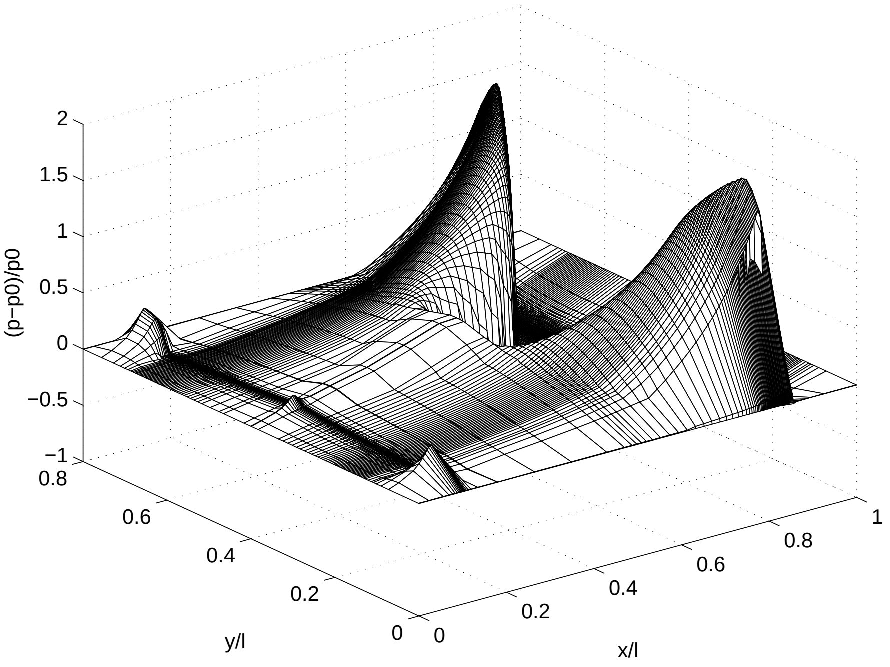

Fig. 5-5 Pressure profile of the air bearing of the Sample-II slider

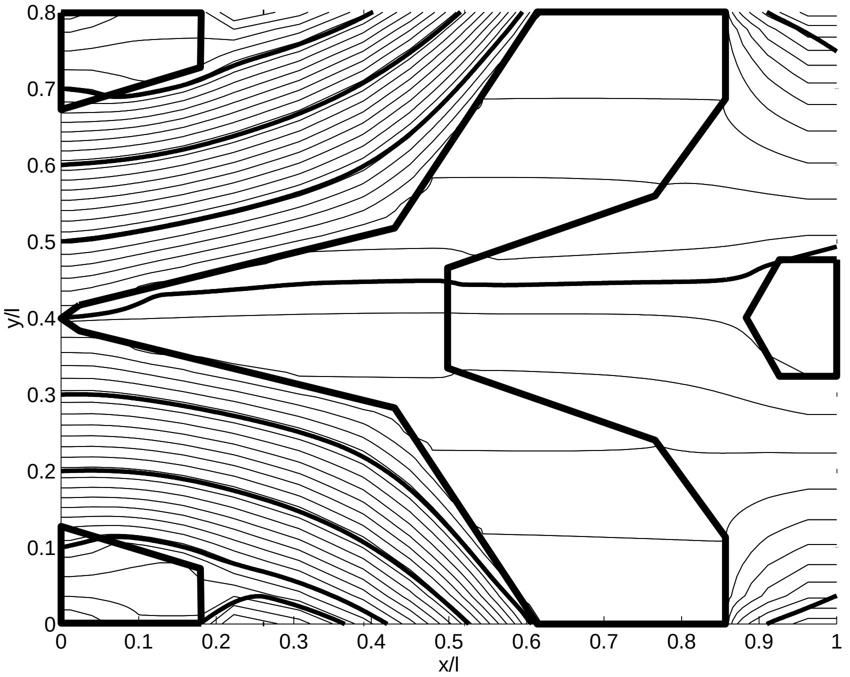

Fig. 5-6 Particle paths in the SDI of the Sample-II slider: MD case

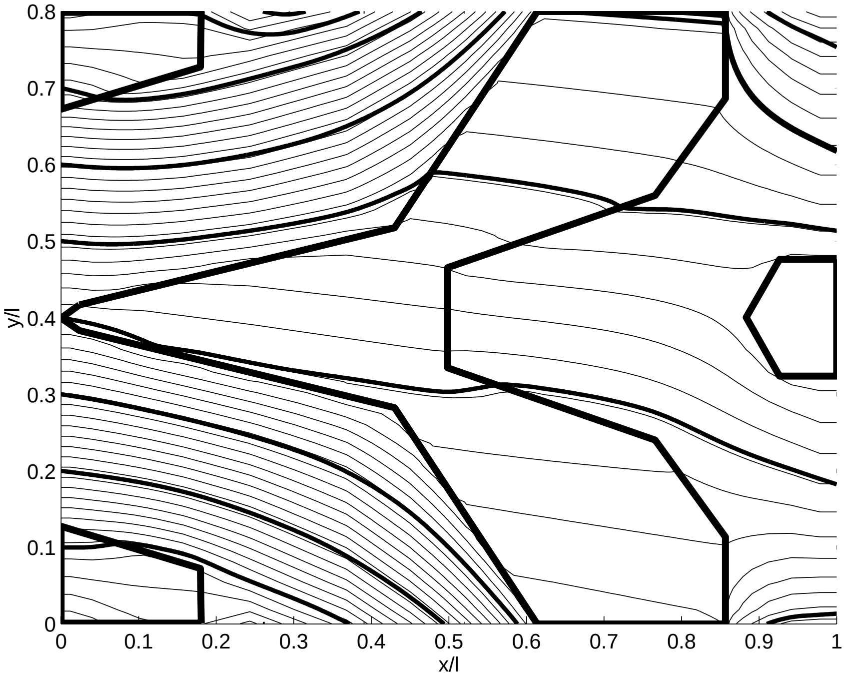

Fig. 5-7 Particle paths in the SDI of the Sample-II slider: ID case

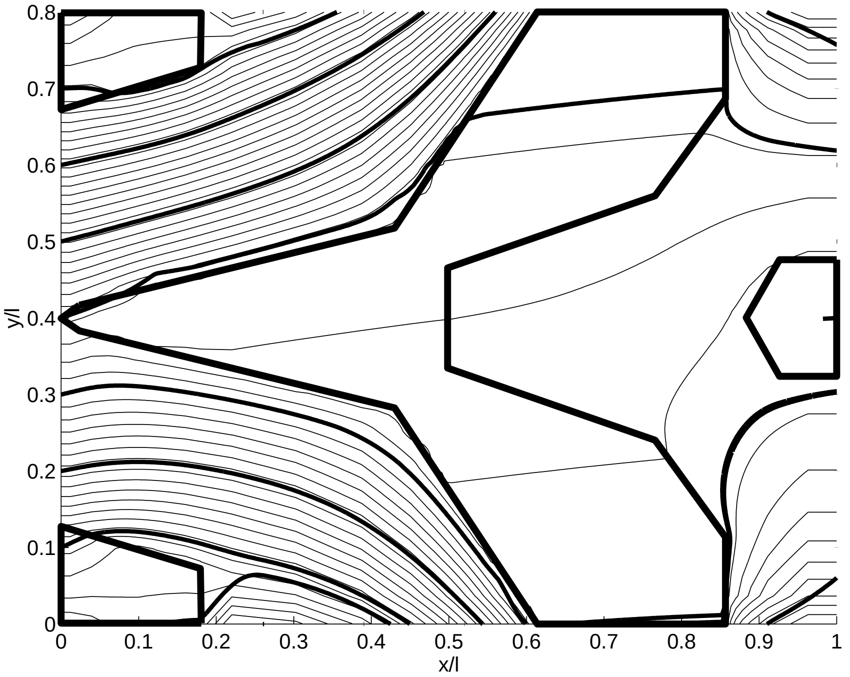

Fig. 5-8 Particle paths in the SDI of the Sample-II slider: OD case

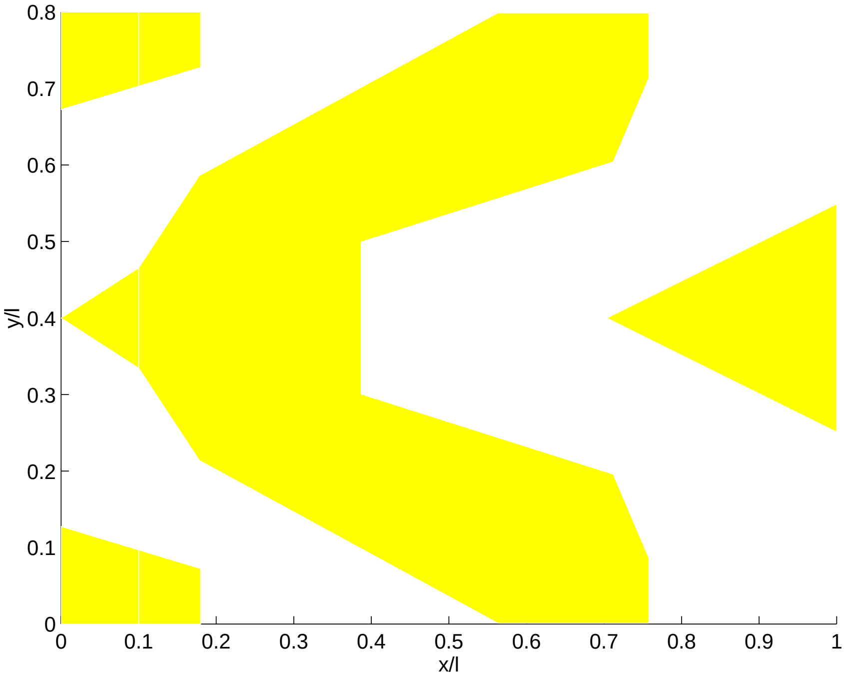

Fig. 5-9 Rail shape of the Sparrow slider

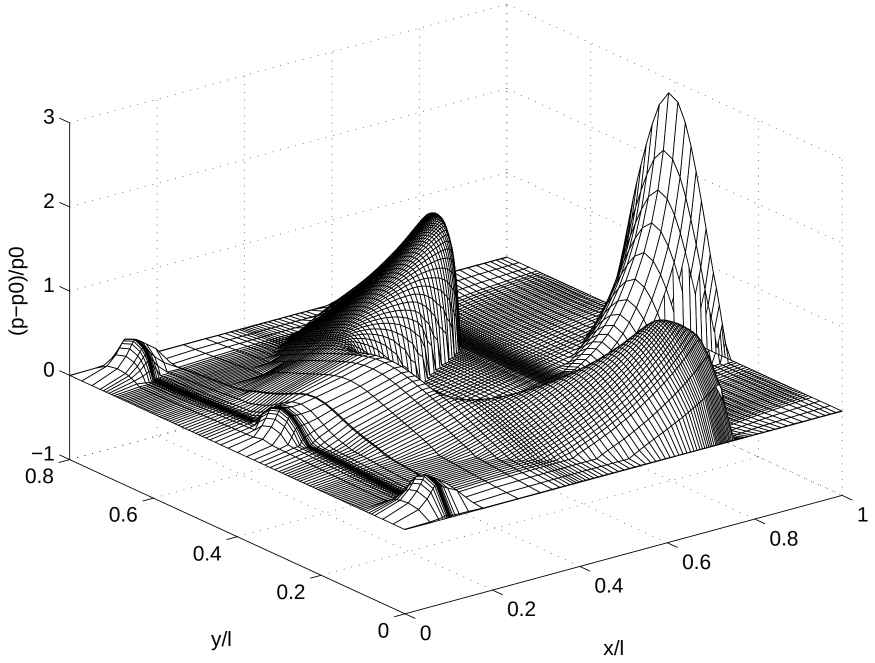

Fig. 5-10 Pressure profile of the air bearing of the Sparrow slider

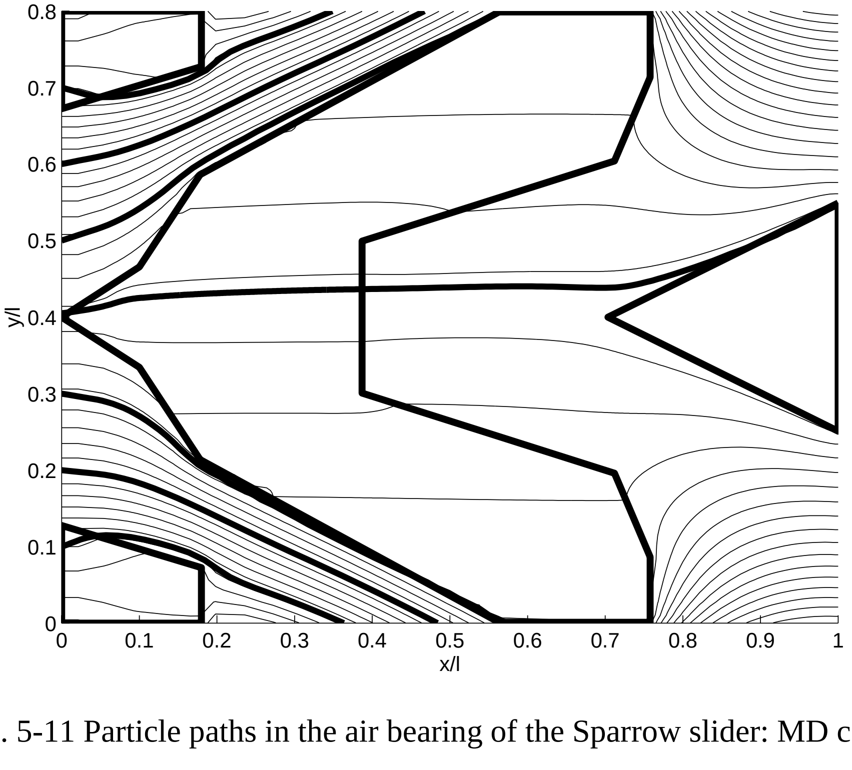

Fig. 5-11 Particle paths in the air bearing of the Sparrow slider: MD case

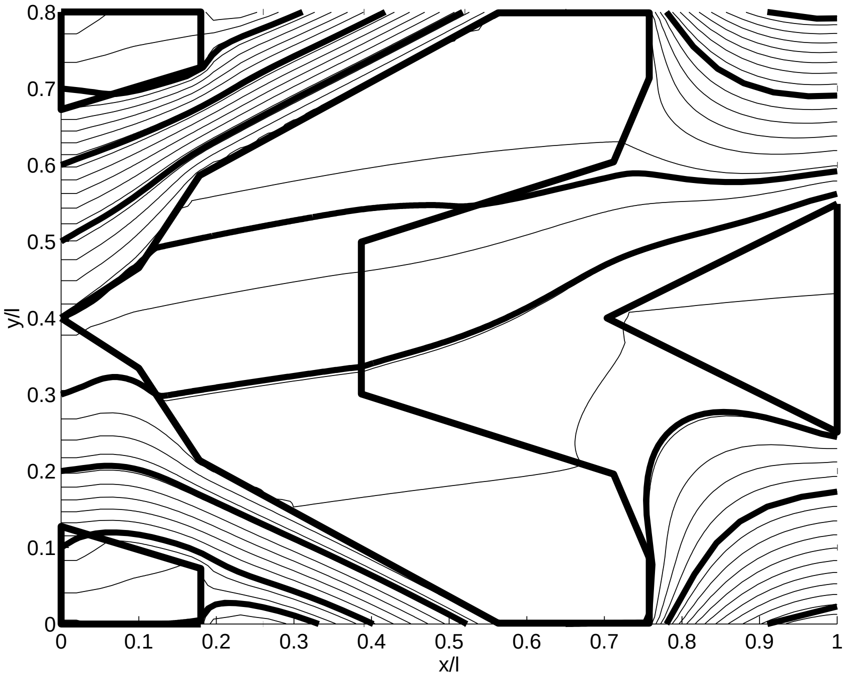

Fig. 5-12 Particle paths in the air bearing of the Sparrow slider: ID case

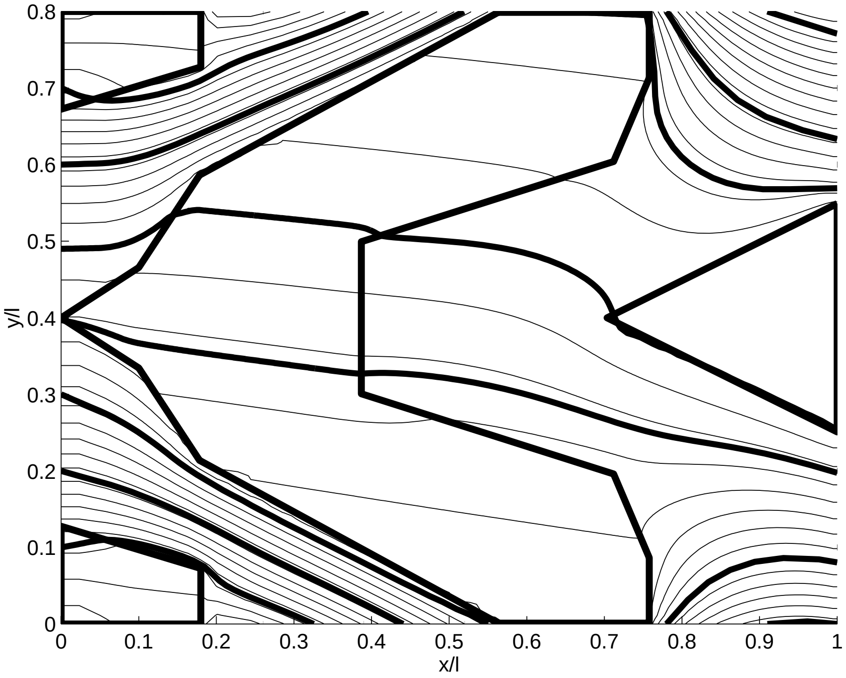

Fig. 5-13 Particle paths in the air bearing of the Sparrow slider: OD case

CHAPTER 6[1]

A HEAT TRANSFER MODEL FOR THE THERMAL FLUCTUATIONS IN A THIN SDI

6.1 Introduction

The magnetoresistive (MR) transducer was developed (Hunt, 1971) using the principle that its resistance varies with the variation of the ambient magnetization. A problem with the MR head is that it is very sensitive to temperature variation because the resistance is also temperature dependent. One such phenomenon is that the MR readback signal fluctuates with the fluctuation of the flying height when the slider flies over an asperity without contact (Tian, et al., 1997). It is concluded that the heat transfer in the air bearing makes a significant contribution to the fluctuation of the MR readback signal, and the air bearing acts as coolant. In this chapter, we conduct a theoretical study of the heat transfer in the air bearing to find the mechanism of this "cooling" effect.

One important issue in solving the heat transfer problem between a slider and the air bearing is that the traditional lubrication theory, which is based on the continuum assumption, is not valid when the air bearing is very thin. For example, the flying height of a typical MR head, which usually has a recessed depth of 3 μm, is around 50 *nm* in today's hard disk drive. The Knudsen number $Kn=\lambda/h$, where λ is mean free path of the air and h is the spacing of the slider/disk interface, is between 0.02 to 1 under this

---

[1] Part of this chapter has been published in Zhang, et al. (1997d).

condition. The air flow with such a Knudsen number is regarded as within the slip and transition regimes, and far out of the continuum region of $Kn<0.01$ (Schaaf, S.L., et al., 1963). One approach to solve the heat transfer problems in these regimes is to apply the Maxwell-Boltzman equation of the kinetic theory of gases. However, solving a complete Maxwell-Boltzman equation requires very large computation time. Another approach is to assume that the continuum-based governing equations, such as Navier-Stokes (N-S) equation and the energy equation, are still usable. As a modification, the discontinuous boundary conditions are applied (Kennard, E.H., 1938). These methods have been used previously in solving for the velocity distribution in an air bearing by several researchers (Burgdorfer, A., 1959; Gans, R., 1985; Fukui, et al., 1988).

Another important issue in solving the heat transfer problems is that the continuity equation, momentum equation and energy equation, if we use the method mentioned above, need to be solved simultaneously, because the physical properties of air depend on the temperature, which usually makes the problem more complicated, and leads to the need of more computation time in the numerical analysis. A simple approach is to assume the properties are constant if the temperature variation is not too large, so we can evaluate the properties at a certain reference temperature, say the average temperature of the two surfaces. With such an approximation, the momentum and energy equations can be decoupled for solution. Since the temperature difference between the slider and disk surfaces is expected to be very small, it is reasonable to apply a constant property assumption in an air bearing. Thus, we can solve the momentum and energy equations separately.

In the following analysis, we first simplify the N-S and energy equations by dimensional analysis. Then we solve the reduced N-S equation with slip boundary condition to get the velocity distribution and solve the energy equation with jump boundary conditions to get the temperature distribution in the air bearing. Using Fourier's law, we obtain an expression for the heat flux between a slider and air bearing. A computer program is implemented to simulate the heat flux for several cases. The slider/disk system as well as the related coordinate system used in the analysis are the same as that used in the contamination analysis (Fig. 2-1).

6.2 Governing Equations in the SDI

In the following analysis we focus on the steady case, so the time dependent terms in the related equations disappear. Using dimensional analysis, we reduce these equations to simpler forms.

6.2.1 Navier-Stokes (N-S) Equation

The simplification of the N-S equation in an air bearing has been performed by many researchers (Gross, W.A., et al., 1980). The results have been used in Chapter 2 for the solution of the velocity field in a SDI. For the completeness of the analysis, we list the reduced N-S equation again here:

$$\frac{\partial p}{\partial x} = \mu \frac{\partial^2 u}{\partial z^2}, \tag{6-1}$$

$$\frac{\partial p}{\partial y} = \mu \frac{\partial^2 \upsilon}{\partial z^2}, \tag{6-2}$$

$$\frac{\partial p}{\partial z} = 0, \tag{6-3}$$

where u, υ, p and μ are respectively velocities in the x and y directions, pressure and the viscosity of the air, which are the same as in Chapter 2. For simplification, we assume μ is uniform in the air bearing.

6.2.2 Energy Equation

As in the N-S equation, the energy equation can also be simplified by using dimensional analysis in the air bearing. Since the magnitudes $|\partial/\partial x| \sim |\partial/\partial y| << |\partial/\partial z|$, we neglect the relative small terms and write the energy equation as:

$$\rho c_p u \frac{\partial T}{\partial x} + \rho c_p \upsilon \frac{\partial T}{\partial y} - u \frac{\partial p}{\partial x} - \upsilon \frac{\partial p}{\partial y} = k \frac{\partial^2 T}{\partial z^2} + \mu \left(\frac{\partial u}{\partial z} \right)^2 + \mu \left(\frac{\partial \upsilon}{\partial z} \right)^2 , \qquad (6\text{-}4)$$

where ρ is the density, c_p is the specific heat, k is the heat conductivity and is assumed uniform in the air bearing, and T is the temperature of the air.

As in simplifying the N-S equation, we use the characteristics of the air bearing to reduce the energy equation (6-4). Let's first define the non-dimensional variables: $u^*=u/\hat{U}$, $\upsilon^*=\upsilon/\hat{U}$, $T^*=T/\Delta T$, $p^*=p/P_0$, $x^*=x/L$, $y^*=y/L$, $z^*=z/L$, where $\hat{U}$ is the disk velocity, ΔT is the temperature difference between the slider and disk surfaces and P_0 is the reference pressure (say the ambient pressure), L is the length of the slider and h is the thickness of the air bearing. Substituting these variables into equation (6-4) we obtain the following expression:

$$\frac{\hat{U}h^2}{\alpha L} \left(u^* \frac{\partial T^*}{\partial x^*} + \upsilon^* \frac{\partial T^*}{\partial y^*} \right) - \frac{P_0 \hat{U} h^2}{k L \Delta T} \left(u^* \frac{\partial p^*}{\partial x^*} + \upsilon^* \frac{\partial p^*}{\partial y^*} \right) = \frac{\partial^2 T^*}{\partial z^{*2}} +$$

$$\frac{\mu \hat{U}^2}{k \Delta T} \left[\left(\frac{\partial u^*}{\partial z^*} \right)^2 + \left(\frac{\partial \upsilon^*}{\partial z^*} \right)^2 \right], \qquad (6\text{-}5)$$

where $\alpha = k/\rho c_p$ is the thermal diffusivity.

For a typical head/disk air bearing, we can take $\rho \sim 1\ kg/m^3$, $c_p \sim 10^3\ W{\cdot}s/kg{\cdot}K$, $k \sim 0.03\ W/m{\cdot}K$, $\mu \sim 10^{-5}\ kg{\cdot}m/s$, $\hat{U} \sim 15\ m/s$, $L \sim 2\ mm$, $h \sim 50\ nm$, $T_0 \sim 300\ K$, and $P_0 \sim 10^5\ kg/m{\cdot}s^2$. The temperature difference ΔT depends on the value of resistance of the MR transducer and the electrical current passing through it, and it usually has a magnitude of 10 °*C*. Tian, et al. (1997) measured❶ the ΔT of three MR heads with resistance ranging from 27 Ω to 33 Ω and electrical current of 13 *mV*. They obtained the temperature difference ΔT changing between 30 °C and 45 °C for the three cases. Here we choose $\Delta T \sim 20$ °*C*. Thus $\hat{U}h^2/\alpha L \sim PrRe(h/L) \sim 10^{-6}$, $(P_0\hat{U}h^2)/(kL\Delta T) \sim (PrReM^2)(T_0/\Delta T)(h/L)(p_0/\rho\hat{U}^2) \sim 10^{-5}$, and $\mu\hat{U}^2/k\Delta T \sim PrM^2(T_0/\Delta T) \sim 10^{-2}$, where Pr is the Prandtl number defined by $Pr = \mu c_p/k$, Re is the Reynolds number defined as $Re = \hat{U}h/\nu$, M is the Mach number defined by $\hat{U}/(\gamma RT_0)^{1/2}$, and T_0 is a reference temperature. Therefore, compared with the conduction term in equation (6-5), the non-linear terms in the LHS are small and can be neglected. The energy equation is thus reduced to:

$$k\frac{\partial^2 T}{\partial z^2} + \mu\left(\frac{\partial u}{\partial z}\right)^2 + \mu\left(\frac{\partial \upsilon}{\partial z}\right)^2 = 0\,. \tag{6-6}$$

Strictly speaking, this equation is valid only when $PrRe(h/L) \ll 1$, $(PrReM^2)(T_0/\Delta T)(h/L) \times (p_0/\rho\hat{U}^2) \ll 1$ and $h/L \ll 1$. Fortunately, these conditions are usually satisfied in a slider/disk air bearing.

---

❶ The temperature was not measured directly in Tian, et al's paper. They first measured the voltage across the MR transducer to determine the changes of the MR resistance. Then they used a correlation obtained by experiment to estimate the temperature change of the MR transducer.

6.2.3 Boundary Conditions

We assume that the disk has a non-zero velocity $\hat{U}$ in the x direction and zero velocity $\hat{V}$ in the y direction, which is approximately the case of a slider flying at a middle radius of the disk. As for the temperature, considering the disk has a much larger size than the air bearing and rotates with high speed, we assume that it has a constant and uniform surface temperature that is the same as that of the ambient air flow. We also assume that the slider's surface temperature is uniform. Introducing the slip condition for the velocity and the jump condition for the temperature at the boundaries of the air bearing (Schaaf, S.L., et al., 1963; Kennard, E.H., 1938), we can write the boundary conditions for velocity and temperature as:

$$u(0) = \hat{U} + \frac{2-\sigma_M}{\sigma_M}\lambda \left.\frac{\partial u}{\partial z}\right|_{z=0}, \tag{6-7}$$

$$u(h) = -\frac{2-\sigma_M}{\sigma_M}\lambda \left.\frac{\partial u}{\partial z}\right|_{z=h}, \tag{6-8}$$

$$\upsilon(0) = \frac{2-\sigma_M}{\sigma_M}\lambda \left.\frac{\partial \upsilon}{\partial z}\right|_{z=0}, \tag{6-9}$$

$$\upsilon(h) = -\frac{2-\sigma_M}{\sigma_M}\lambda \left.\frac{\partial \upsilon}{\partial z}\right|_{z=h}, \tag{6-10}$$

$$T(0) = T_d + 2\frac{2-\sigma_T}{\sigma_T}\frac{\gamma}{\gamma+1}\frac{\lambda}{Pr}\left.\frac{\partial T}{\partial z}\right|_{z=0}, \tag{6-11}$$

$$T(h) = T_s - 2\frac{2-\sigma_T}{\sigma_T}\frac{\gamma}{\gamma+1}\frac{\lambda}{Pr}\left.\frac{\partial T}{\partial z}\right|_{z=h}, \tag{6-12}$$

where σ_M is the momentum accommodation coefficient and σ_T is the thermal accommodation coefficient, γ is the ratio of c_p to c_v, which are specific heats at, respectively, constant pressure and constant volume, T_s and T_d are , respectively, the slider surface temperature and disk surface temperature. For convenience, we write $a=(2-\sigma_M)/\sigma_M$ and $b=2(2-\sigma_T)\gamma/\sigma_T\,(\gamma+1)Pr$ in the following analysis.

6.3. Heat Transfer between the Slider and the SDI

To get the heat transfer in a SDI, we need to know the temperature distribution in it. This requires us to solve the N-S equation and the energy equation. Because of the approximation of constant properties of the air, we can decouple the N-S and the energy equations and solve them separately.

6.3.1 Velocity Distribution

The velocity distribution can be obtained by integrating the reduced N-S equations (6-1) ~ (6-3) with boundary conditions (6-7)~(6-10). The procedure is straight forward and was done by other researcher (Burgdorfer, A., 1959; Mitsuya, Y., 1993). Here we list the results of the solution:

$$u=-\frac{1}{2\mu}\frac{\partial p}{\partial x}\left(a\lambda h+hz-z^2\right)+\hat{U}\left(1-\frac{z+a\lambda}{h+2a\lambda}\right), \tag{6-13}$$

$$\upsilon=-\frac{1}{2\mu}\frac{\partial p}{\partial y}\left(a\lambda h+hz-z^2\right). \tag{6-14}$$

These results are the same as those used in Chapter 2, except that the velocity component $\hat{V}$ is taken as zero.

In the RHS of equation (6-13), the first term is the contribution of the Poiseuille flow and the second term is the contribution of the Couette flow. While in (6-14) only the Poiseuille flow result is involved because we take the *y*-component of the disk velocity

$\hat{V}$ =0. Clearly, these results are not complete because we still do not know the pressure gradient in the *x* and *y* directions. To finish the solution we need to solve the Reynolds equation, which comes from the integration of the continuity equation (Burgdorfer, A., 1959; Fukui, et al., 1988), to obtain the pressure distribution first. To get the solution, a numerical method is required (Cha, E.T., et al., 1995; Lu, S., et al., 1994).

6.3.2 Temperature Distribution

Substituting the velocity solutions (6-13) and (6-14) into the energy equation (6-6) and integrate it, we obtain the temperature distribution in the air bearing

$$\begin{aligned}T = T_d &- \frac{1}{k}\Bigg\{\frac{1}{12\mu}\left[\left(\frac{\partial p}{\partial x}\right)^2+\left(\frac{\partial p}{\partial y}\right)^2\right]z^4 - \frac{1}{3}\left\{\frac{h}{2\mu}\left[\left(\frac{\partial p}{\partial x}\right)^2+\left(\frac{\partial p}{\partial y}\right)^2\right]+\frac{\partial p}{\partial x}\frac{U}{h+2a\lambda}\right\}z^3 + \\ &\frac{\mu}{2}\left[\left(\frac{h}{2\mu}\frac{\partial p}{\partial x}+\frac{U}{h+2a\lambda}\right)^2+\frac{h^2}{4\mu^2}\left(\frac{\partial p}{\partial y}\right)^2\right]z^2\Bigg\}+\Bigg\{\frac{T_s-T_d}{h+2b\lambda}+ \\ &\frac{1}{k}\left[\frac{h^3}{24\mu}\left\{\left(\frac{\partial p}{\partial x}\right)^2+\left(\frac{\partial p}{\partial y}\right)^2\right\}+\frac{\mu U^2 h}{2(h+2a\lambda)^2}+\frac{Uh^3}{6(h+2a\lambda)(h+2b\lambda)}\frac{\partial p}{\partial x}\right]\Bigg\}(z+b\lambda).\end{aligned}$$

(6-15)

As in the velocity solutions, the temperature *T* also consists of contributions from the Poiseuille flow and Couette flow. In addition, extra terms exist which are the combined effects of the both flows.

6.3.3 Heat Transfer

Using Fourier's Law $q=-k\partial T/\partial z$ at $z=h$ and the temperature solution (6-15), we can obtain the heat transfer into the slider as follows:

$$q = -k\frac{T_s - T_d}{h + 2b\lambda} + \frac{h^3}{24\mu}\left[\left(\frac{\partial p}{\partial x}\right)^2 + \left(\frac{\partial p}{\partial y}\right)^2\right] + \frac{\mu U^2 h}{2(h + 2a\lambda)^2} -$$

$$\frac{Uh^3}{6(h + 2b\lambda)(h + 2a\lambda)}\frac{\partial p}{\partial x}. \qquad (6\text{-}16)$$

We can also write the heat transfer equation (6-16) in a non-dimensional form as:

$$\frac{qh}{\mu U^2} = -\frac{T_s - T_d}{(\gamma - 1)PrM^2 T_0\left(1 + 2b\frac{\lambda}{h}\right)} + \frac{1}{2\left(1 + 2a\frac{\lambda}{h}\right)^2} +$$

$$\frac{1}{24}Re^2\left(\frac{h}{L}\right)^2\left(\frac{P_0}{\rho U^2}\right)^2\left[\left(\frac{\partial p^*}{\partial x^*}\right)^2 + \left(\frac{\partial p^*}{\partial y^*}\right)^2\right] -$$

$$\frac{1}{6}Re\frac{h}{L}\frac{P_0}{\rho U^2}\frac{1}{\left(1 + 2b\frac{\lambda}{h}\right)\left(1 + 2a\frac{\lambda}{h}\right)}\frac{\partial p^*}{\partial x^*}. \qquad (6\text{-}17)$$

6.4. Analysis and Discussion

We know that the velocity field obtained by equations (6-13) and (6-14) is the result of the Couette flow and Poiseuille flow. It is natural to think that the heat transfer in the SDI is also related to the two flows. In order to reveal the physical meaning of each term in the heat flux equation (6-16), we study the heat transfer for the single Couette flow and Poiseuille flow between two plane plates, respectively. The velocity fields for the two types of flows are shown in Figs. 6-1 and 6-2.

6.4.1 Couette flow

Using the linear expression for the Couette flow, in which the velocity is unidirectional (say in the *x* direction), and the boundary conditions (6-7) and (6-8), we can obtain the velocity distribution as:

$$u = \hat{U}\left(1 - \frac{z + a\lambda}{h + 2a\lambda}\right). \tag{6-18}$$

Substituting this velocity solution into the energy equation (6-6) and integrating it, we obtain the temperature distribution and then the heat transfer between the upper plane and the air flow by Fourier's Law:

$$T = T_d - \frac{\mu \hat{U}^2}{2k(h + 2a\lambda)^2} z^2 + \left[\frac{T_s - T_d}{h + 2b\lambda} + \frac{\mu \hat{U}^2 h}{2k(h + 2a\lambda)^2}\right](z + b\lambda), \tag{6-19}$$

$$q = -k \frac{T_s - T_d}{h + 2b\lambda} + \frac{\mu \hat{U}^2 h}{2(h + 2a\lambda)^2}\,. \tag{6-20}$$

We can also write this heat transfer equation in a non-dimensional form as:

$$\frac{qh}{\mu \hat{U}^2} = -\frac{T_s - T_d}{(\gamma - 1) Pr M^2 T_0 \left(1 + 2b\frac{\lambda}{h}\right)} + \frac{1}{2\left(1 + 2a\frac{\lambda}{h}\right)^2}\,. \tag{6-21}$$

A similar expression as equation (6-21) can also be found in Schaaf's (1961), in which no derivation is given out. Comparing equation (6-20) with equation (6-16), we see that the second term in the RHS of (6-16) is the contribution from the viscous dissipation by Couette flow.

6.4.2 Poiseuille Flow

The velocity field in the Poiseuille flow is also unidirectional and can be obtained by integrating equation (6-1) and applying the boundary conditions (6-4) and (6-5) with $\hat{U}$ =0. The solution is:

$$u = -\frac{1}{2\mu}\frac{\partial p}{\partial x}\left(a\lambda h + hz - z^2\right). \tag{6-22}$$

In a similar way as used with the Couette flow, we can express the temperature distribution and the heat transfer between the upper plane and the air flow as:

$$T = T_d - \frac{1}{4k\mu}\left(\frac{1}{3}z^4 - \frac{2}{3}hz^3 + \frac{1}{2}h^2 z^2\right)\left(\frac{\partial p}{\partial x}\right)^2 +$$

$$\left[\frac{T_s - T_d}{h + 2b\lambda} + \frac{h^3}{24k\mu}\left(\frac{\partial p}{\partial x}\right)^2\right](z + b\lambda), \tag{6-23}$$

$$q = -k\frac{T_s - T_d}{h + 2b\lambda} + \frac{h^3}{24\mu}\left(\frac{\partial p}{\partial x}\right)^2. \tag{6-24}$$

Or in the non-dimensional form:

$$\frac{qh}{\mu\hat{U}^2} = -\frac{T_s - T_d}{(\gamma - 1)PrM^2 T_0\left(1 + 2b\frac{\lambda}{h}\right)} + \frac{1}{24}Re^2\left(\frac{h}{L}\right)^2\left(\frac{P_0}{\rho\hat{U}^2}\right)^2\left(\frac{\partial p^*}{\partial x^*}\right)^2. \tag{6-25}$$

Comparing equation (6-24) with equation (6-16), we see that the third term in the RHS of (6-16) is the contribution from the viscous dissipation of Poiseuille flow. Clearly, the fourth term is a combined contribution of both Couette flow and Poiseuille flow.

6.4.3 Heat Conduction

The first term in the RHS of equation (6-16) is the contribution of heat conduction. Due to the introduction of the temperature jump at the boundary, the effect of the heat conduction is reduced by a factor of (1+2$b\lambda/h$) compared to the continuum case. Note that because of the effect of viscous dissipation, the heat transfer between the slider and air bearing is not zero when the temperature difference between the slider surface and the disk surface vanishes,.

6.5 Simulation Results

In this section, we compute several cases for sliders flying close to the disk surface. We assume that the slider has a surface temperature either equal to that of the disk or higher than that of the disk because of an electrical current that goes through the MR transducer (Tian, et al., 1997). For convenience, we choose a 50% (2*mm*×1.6*mm*) tri-pad slider with taper length and angle of 0.2 *mm* and 0.01 *rad*, respectively, and with a recessed depth of 3μm. The load is given by 3.5 *g*. The slider is fixed at a radial position *r*=23 *mm*. The rail shape of it is shown in Fig. 6-3. Note that this slider has a slight difference in rail size compared with that used in the contamination study (Fig. 5-1), because we want a higher flying height that is close to that for a typical MR head used today.

6.5.1 "Cooling" Effects of the Air Bearing

In this case, we choose the disk rotation Ω=6400 *rpm*. With this rotation, the pressure distribution of the air bearing is solved by using the CML Air Bearing Simulator (Lu, S., et al., 1995) and shown as in Fig. 6-4, and the flying characteristics are shown in Table 6-1. We know that the viscous dissipation term is about 10^{-2} of the heat conduction term in magnitude with the temperature difference $\Delta T=(T_s-T_d)$~20 °*C*. For the convenience of comparing the relative relation of the two terms, we take a smaller temperature difference ΔT~1 °*C* in the analysis of this chapter. The heat flux for this ΔT is calculated and shown in Fig. 6-5. Note that positive values mean that heat is transferred from the slider to the air bearing.

Table 6-1 Flying Characteristics

Disk rotation (*rpm*)	Pitch angle (μrad)	Roll (μrad)	CTE-FH☨ (*nm*)
6400	176	8	44

☨ Central trailing edge flying height

It is seen that even at a small temperature difference ΔT=1 °C, the heat conduction still dominates the overall heat transfer and results in a net heat flux from the slider to the air bearing, except at some points around the edges of end rail, where the viscous dissipation is comparable to the heat conduction. Figure 6-6 shows the simulation result for ΔT=0 °C, in which only viscous dissipation exists. For convenience, we use the positive value to represent the heat flowing into the slider in this case. It is seen that the heat flux takes negative values and has larger magnitude at the corners of end rail. The reason for this maybe that the pressure at these points has larger gradient (Fig. 6-4), which makes the magnitude of the heat flux increase sharply there (referring to equation (6-16)). Comparing Fig.6-5 with Fig.6-6, we easily conclude that the viscous dissipation has a smaller magnitude than the heat conduction, except for some points around the edge of the end rail and some cases in which the temperature difference is very close to zero.

6.5.2 Effect of the Flying Height and Disk Speed

From Fig.6-5, we see that heat flux shows different values in the air bearing and recessed region, which implies that the heat flux changes with the SDI spacing. In the following cases, we study the relation of the heat flux to the CTE-FH. Note that to change the flying height, we have to change the disk rotation speed simultaneously if we keep the other parameters the same. Therefore, the heat flux is actually affected by both the disk rotation speed and the flying height. Table 6-2 shows the related flying characteristics for different cases.

The heat flux for ΔT=1 °C at a single point (5 μm inside the CTE) is plotted in Fig.6-7. The average heat flux over the surface of the end rail, which is important for the temperature variation of the MR transducer, is plotted in Fig.6-8. It is seen that both the single point and average heat flux increase with the decrease of the flying height under the given temperature difference (T_s–T_d=1 °*C*). This means that more heat is transferred to the air bearing when the slider flies closer to the disk surface.

Table 6-2. Flying characteristics for different *rpm*

Disk rotation (*rpm*)	Pitch angle (μrad)	Roll (μrad)	CTE-FH (*nm*)
4000	126.5	4.8	15.7
4500	139.0	5.4	20.0
5000	150.4	6.1	25.2
5500	160.0	6.7	32.1
6000	169.3	7.5	39.0
6500	176.9	8.2	47.2
7000	183.7	8.9	56.3
7500	189.4	9.8	66.4
8000	193.9	10.4	77.2
8500	197.3	11.4	88.5

Two similar cases are simulated for ΔT=0 °*C* and plotted in Figs. 6-9 and 6-10, in which negative value means the heat is transferred to the slider because of viscous dissipation. As in Fig. 6-7 and 6-8, the heat flux for both the single point and the averaged value over the surface of the end rail decreases in magnitude with the decrease of the flying height. In other words, if only viscous dissipation exists, less heat will be transferred to the slider when the slider flies closer to the disk surface. Combining this result with that for ΔT=1 °*C*, we can say that the overall “cooling” effect increases with the decrease of the flying height. This conclusion is identical to the experimental result by Tian, et al. (1997). Since the flying height is proportional to the disk speed (Table 6-2), we can also say that the “cooling” effect of the air bearing increases with the decrease of the disk speed.

Figure 6-11 shows the maximum heat flux in the SDI for ΔT=0. Note that the “maximum” here means the maximum magnitude, or maximum heat flux into the slider. It is seen that this maximum heat flux increases with the decrease of the flying height. A reason for it may be that the pressure profile at some points such as the trailing corners of the rear rail (Fig. 6-4), where usually there exists a drastic pressure variation at the low flying heights, becomes smoother at the higher flying height.

Figure 6-12 is the maximum heat flux for ΔT=1 °K. Since the heat conduction dominates the heat transfer in this case, it is seen that the maximum heat flux increases with the decrease of the flying height.

6.6 Summary

We solve the N-S and energy equations with discontinuous boundary conditions to get the heat transfer between a slider and an air bearing. In solving these equations, we make an assumption that the air properties remain the same across the air bearing because the temperature variation is not significant, so we can decouple the N-S equation and energy equation and integrate them separately. The results show that the heat transfer between the slider and air bearing depends on both the heat conduction, which transfers heat to the air bearing if the slider has a higher surface temperature than the disk, and viscous dissipation, which transfers heat to the slider. In most cases heat conduction dominates the heat transfer, and therefore the net result is that heat is transferred from the slider to the air bearing. Under this situation, the air bearing is regarded as a coolant. But when the temperature difference is nearly equal to zero, viscous dissipation dominates the heat transfer and heat is transferred into the slider, so the air bearing acts as a heater. Since the magnitude of the viscous dissipation is not large, this heating effect is not significant. Simulation results also show that the heat conduction effect increases with the decrease of the flying height (or disk rotation speed), but the viscous dissipation effect decreases with the decrease of the flying height (or disk rotation speed). In other words, the “cooling” effect increases with the decrease of the flying height (or disk rotation speed).

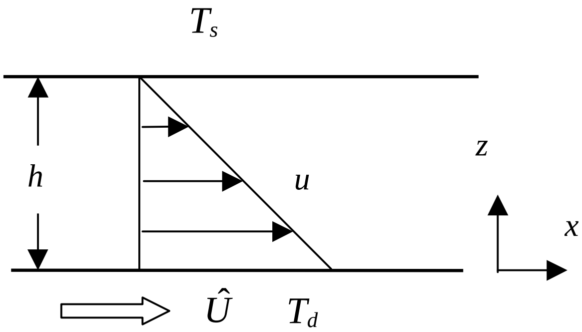

Fig. 6-1 Diagram for Couette flow

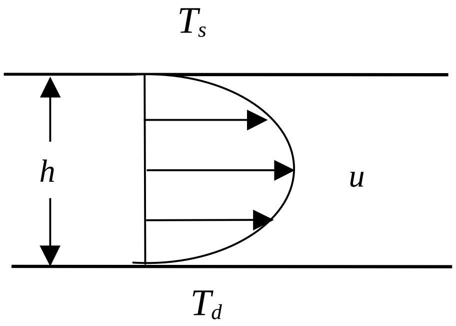

Fig. 6-2 Diagram for Poiseuille flow

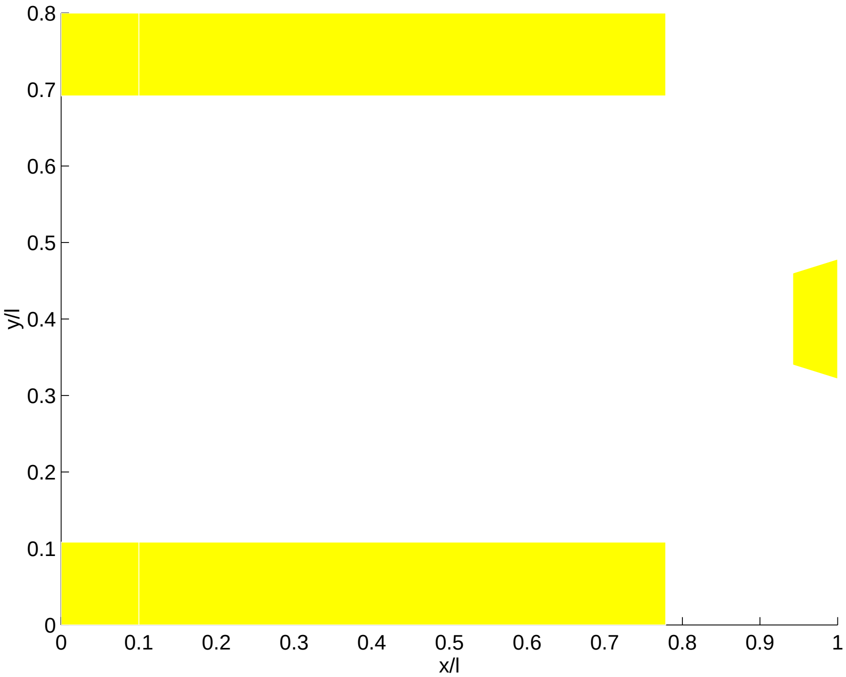

Fig. 6-3 Rail shape of a tri-pad slider

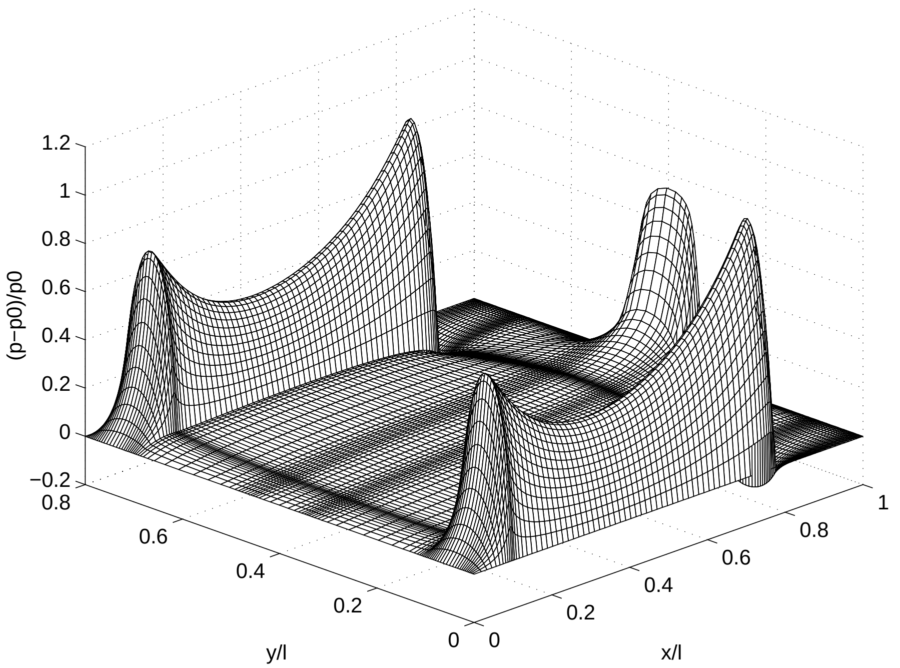

Fig. 6-4 Pressure profile of the air bearing of the tri-pad slider

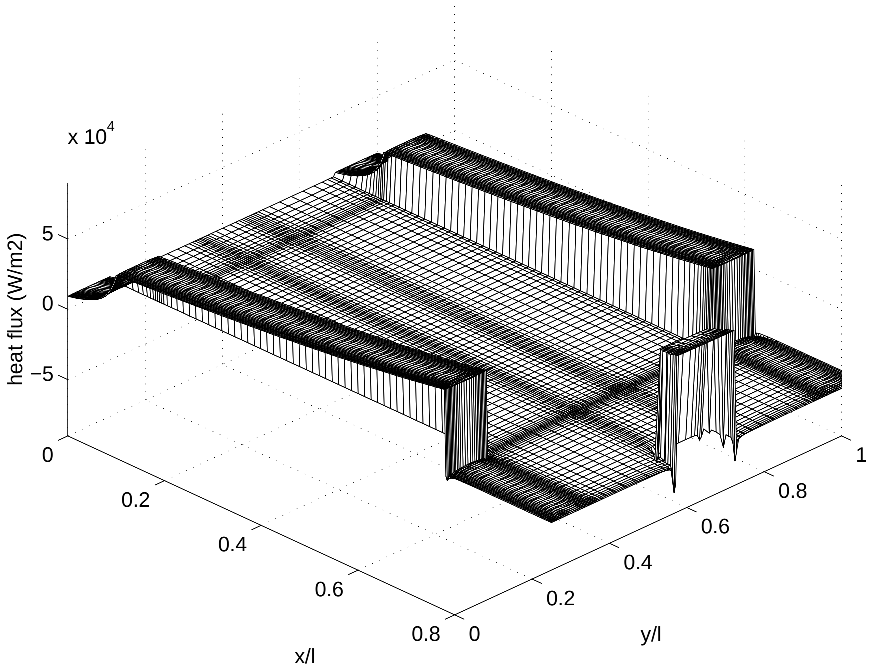

Fig. 6-5 Heat flux between the tri-pad slider and SDI: ΔT=1 °K

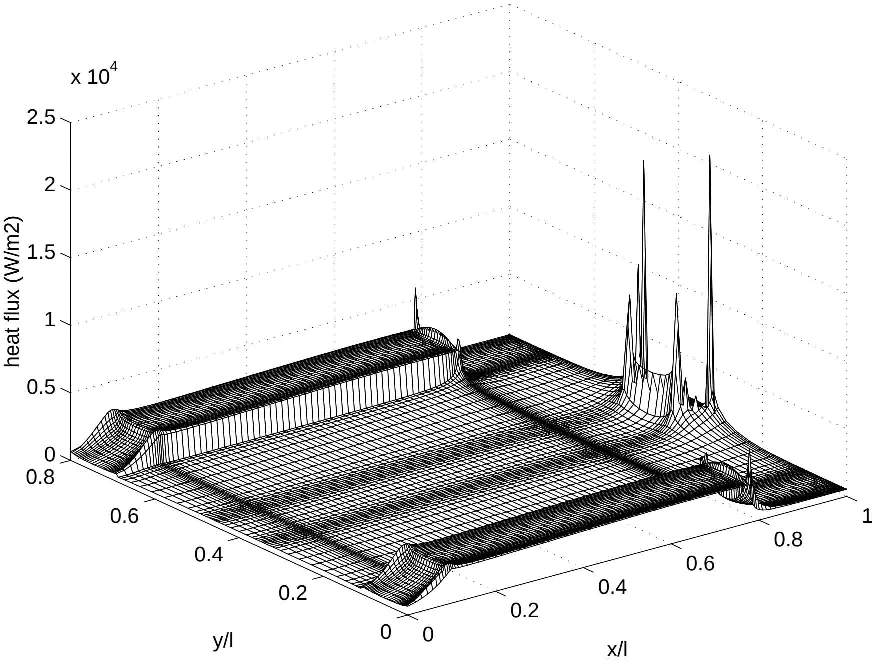

Fig. 6-6 Heat flux between the tri-pad slider and SDI: Δ*T*=0 °*K*

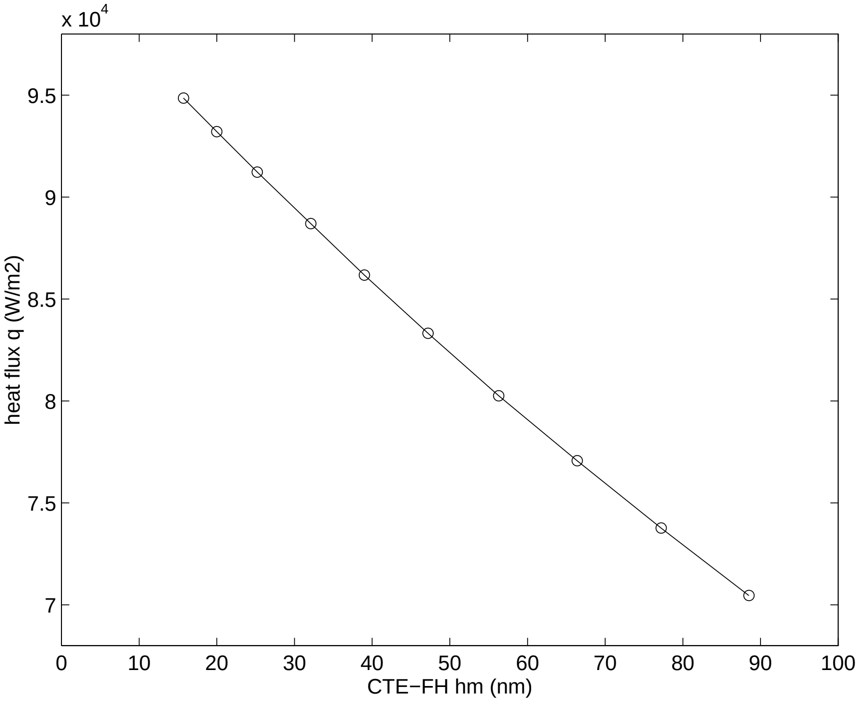

Fig. 6-7 Single point heat flux vs. central trailing edge flying height: Δ*T*=1 °*K*

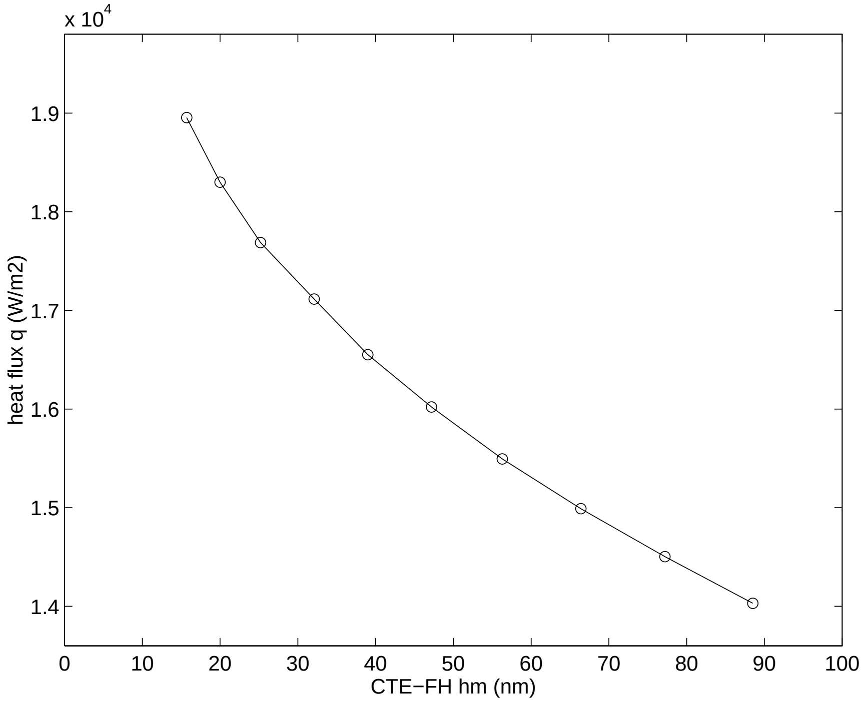

Fig. 6-8 Average heat flux over the surface of trailing edge rail vs. central trailing edge flying height: Δ*T*=1 °*K*

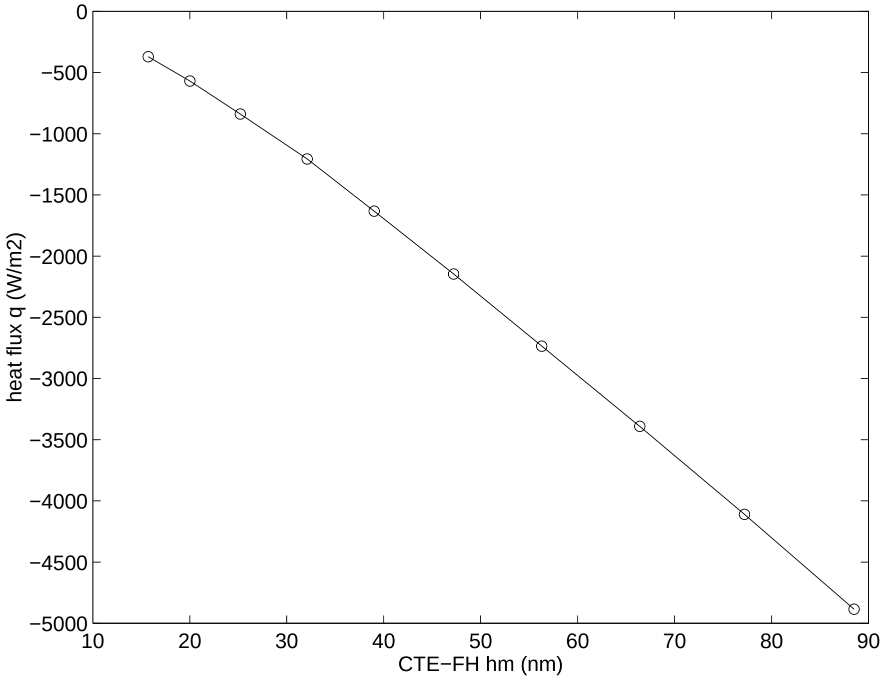

Fig. 6-9 Single point heat flux vs. central trailing edge flying height: Δ*T*=0 °*K*

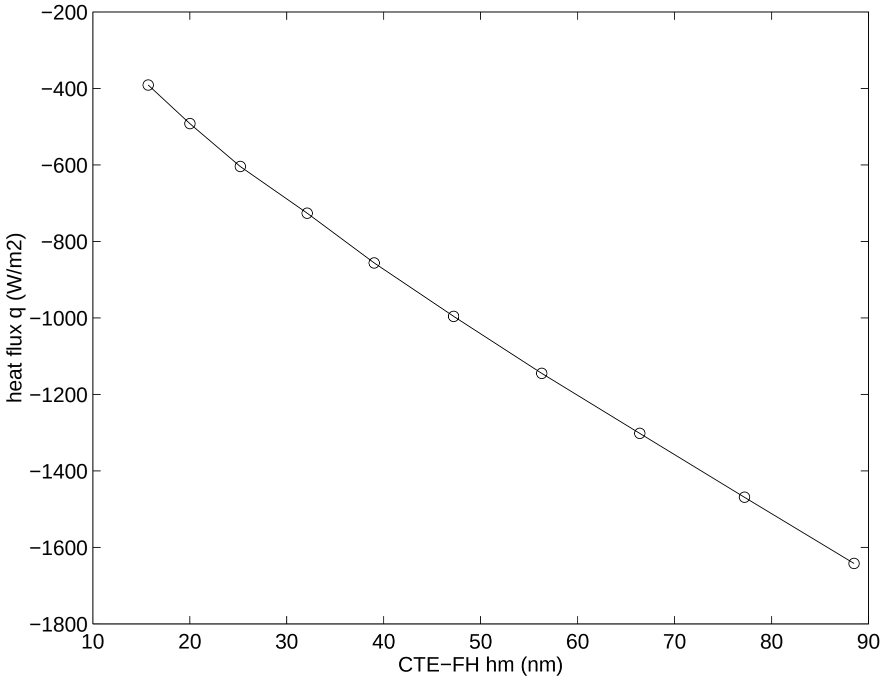

Fig. 6-10 Average heat flux over the surface of trailing edge rail vs. central trailing edge flying height: ΔT=0 °K

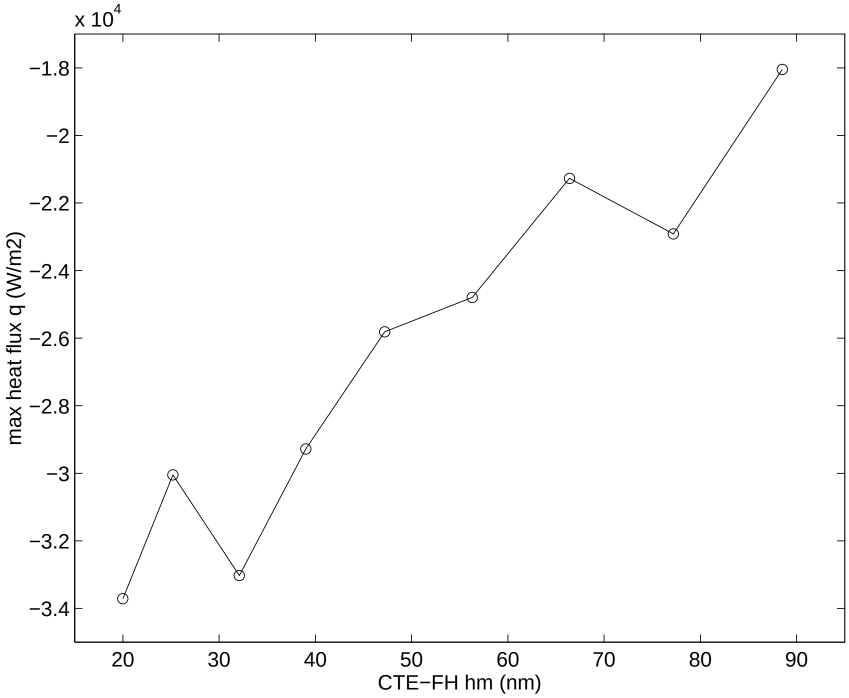

Fig. 6-11 Maximum heat flux in the SDI vs. central trailing edge flying height: ΔT=0 °K

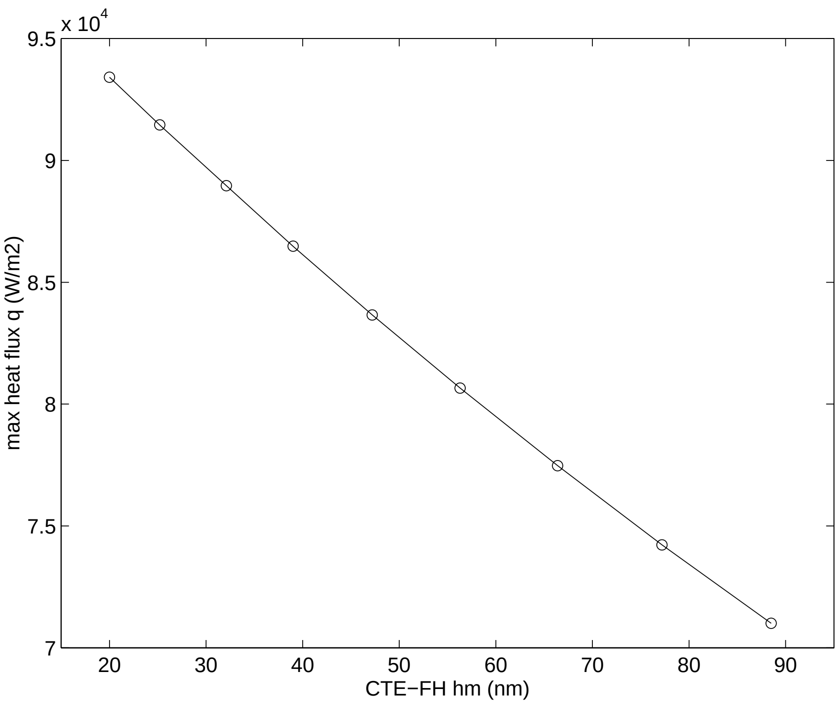

Fig. 6-12 Maximum heat flux in the SDI vs. central trailing edge flying height: ΔT=1 °K

CHAPTER 7[❶]

VARIATION OF THE HEAT FLUX IN A SDI AND ITS EFFECTS ON THE MR READBACK SIGNAL

7.1 Introduction

Tian, et al. (1997) showed that the MR readback signal fluctuates following the fluctuation of the flying height when the slider flies over an asperity without contact. They concluded that the signal fluctuation was mainly caused by the fluctuation of the heat transfer in the air bearing, and that the air bearing acted as a “coolant”. To investigate the “cooling” effect of the air bearing, we developed a steady model for the heat transfer in a SDI (Chapter 6), and we found that the “cooling” effect exists. That is, the heat transferred to the air bearing increases with a decrease of the flying height (or disk rotation speed) when the slider has a higher surface temperature than the disk.

Note that the above conclusion is obtained based on the simulation of a steady model. When we want to decrease the slider flying height using this model, we need to decrease the rotation speed of the disk simultaneously. The latter also affects the heat transfer in the air bearing (Fig. 6-16). Therefore, when we say the heat transferred to the air bearing increases with a decrease of the flying height we mean that the heat transferred to the air bearing increases with a decrease of both flying height and disk rotation speed. Now we ask: if we change the flying height for a fixed disk rotation speed, as in Tian et al.’s

---

[❶] Part of this chapter has been published in Zhang, et al. (1997e).

paper, can we still obtain the result that the air bearing is a “coolant”? What kind of modification we need to do for the model?

In this chapter, we expand the analysis in the Chapter 6 to the case of a slider flying over an asperity, and we introduce a dynamic model that determines the heat transfer fluctuation in an air bearing. With this dynamic heat transfer model, we study the mechanism which causes the fluctuation of the MR readback signals. As in the Chapter 6, we still assume the physical properties of the air are uniform in the SDI.

7.2 Model

The heat flux between a slider and the air bearing is influenced by the slider’s flying height, pressure distribution in the air bearing and the disk rotation speed. When a slider flies over an asperity or a bump, its flying height fluctuates, which causes the pressure and the heat transfer in the air bearing to also fluctuate. Therefore, the whole problem is actually an unsteady problem, and the heat transfer is related to the pressure and velocity distribution in the air bearing for each transient flying state. The solution of this problem needs not only the solution of the air bearing flow field, but also the solution of the dynamic state of the slider.

7.2.1 Dynamics of the Slider

The two-dimensional equations of the motion of a slider flying over a rotating disk are:

$$m\frac{d^2z}{dt^2} = F_s + \int_A (p - P_0)dA, \qquad (7\text{-}1)$$

$$I_\theta \frac{d^2\theta}{dt^2} = M_{s\theta} + \int_A (p - P_0)(x_g - x)dA, \qquad (7\text{-}2)$$

$$I_\phi \frac{d^2\phi}{dt^2} = M_{s\phi} + \int_A (p - P_0)(y_g - y)dA, \tag{7-3}$$

where *m* is the slider's mass, *z* is the slider's vertical displacement, θ and φ are the slider's pitch and roll angles, I_θ and I_φ are the slider's moments of inertia, x_g and y_g are the coordinates of the slider's center of gravity. F_s, $M_{s\theta}$ and $M_{s\varphi}$ are the force and moments exerted on the slider by the suspension, *p* is the pressure distribution in the air bearing, and P_0 is the ambient air pressure.

Dynamic analysis of a slider flying over a rotating disk requires simultaneous solution of the slider motion equation (7-1) ~ (7-3), Reynolds equation (2-31) and the suspension motion equation. When the slider is disturbed from its steady flying state, its suspension applies a time-dependent loading force F_s, and moments $M_{s\theta}$ and $M_{s\varphi}$ to the slider. Thus, the slider's motion is determined by the balance of the air bearing pressure, suspension force and the inertia. The suspension force can be represented using either the flexure stiffness and damping coefficients or the suspension dynamics. One efficient approach is to use modal analysis (Cha, et al., 1995). The eigenvalue solution of the suspension is first sought using the finite element method, then the dynamic response of the suspension assembly is represented by a truncated linear combination of mode shapes.

7.2.2 A Quasi-steady Heat Transfer Model in the Air Bearing

When a slider flies over an asperity, its flying height fluctuates with time. The same is true of the pressure and heat transfer in the air bearing. Therefore, strictly speaking, the heat transfer in the air bearing in this case is an unsteady problem.

Extending the energy equation (6-6) to the unsteady case, we obtain the result:

$$\rho c_p \frac{\partial T}{\partial t} = k\frac{\partial^2 T}{\partial z^2} + \mu\left(\frac{\partial u}{\partial z}\right)^2 + \mu\left(\frac{\partial \upsilon}{\partial z}\right)^2, \tag{7-4}$$

where ρ, c_p, k and μ are, respectively, the density, specific heat, heat conductivity and viscosity of the air, T is the temperature, and u and υ are velocity components of the airflow.

Note that an important characteristic of a slider air bearing is that its thickness is ultra-thin. For example, a typical thickness dimension for a hard drive using MR head is about 50 *nm* or less. For such a small thickness, we can expect that any small thermal disturbance may cause a transient change in the temperature distribution, or the temperature distribution may shift to a new equilibrium very quickly. To justify this view, let's look at the transient term (LHS) and the conduction term (1st term in RHS) in Eq. (7-4). If we assume the magnitude of the temperature variation in the conduction term is ΔT_{cond}~T_s–T_d, where T_s and T_d are the temperatures of the slider and disk surfaces, then the magnitude of the temperature variation in the transient term can be approximated as ΔT_{tran}~$(\Delta h/h)\ \Delta T_{cond}$, where Δh is the variation of the flying height. Usually, $\Delta h/h$ is smaller than 1 for a flying slider. If we further assume that t~$L/\hat{U}$ and z~h, we can write the ratio of the transient term to the conduction term as: $(\Delta h/h)(h^2\hat{U}/L\alpha)$ ~$PrRe_h h/L$, where $\alpha=k/\rho c_p$, $Pr=\nu/\alpha$ and $Re_h=\hat{U}h/\nu$. For the air bearing and slider studied in this report, Pr~0.7, h~5×10^{-8} *m*, L~10^{-3} *m*, $\hat{U}$ ~15 *m/s*, ν~10^{-5} m^2/s. Thus $PrRe_h h/L$ has a magnitude of 10^{-6}, or the transient term is negligible compared with the conduction term. Dropping the transient term in (7-4), we can write the energy equation as:

$$0 = k\frac{\partial^2 T}{\partial z^2} + \mu\left(\frac{\partial u}{\partial z}\right)^2 + \mu\left(\frac{\partial \upsilon}{\partial z}\right)^2. \tag{7-5}$$

This equation is a quasi-steady expression of the energy equation.

We can also simplify the N-S equation in a similar way. Here we use its x component as an example:

$$\rho \frac{du}{dt} = -\frac{\partial p}{\partial x} + \mu \frac{\partial^2 u}{\partial z^2} . \tag{7-6}$$

Using the dimensional analysis and values of the related physical properties, we obtain the ratio of the transient term (LHS) to the diffusion term (2nd on the RHS) as: $Re_h h/L \sim 10^{-7}$. Thus, we can drop the transient term in (7-6) and get:

$$\frac{\partial p}{\partial x} = \mu \frac{\partial^2 u}{\partial z^2} . \tag{7-7}$$

Similarly, we can reduce the y component of the N-S equation. Note that equations (7-5) and (7-7) have the same forms as equations (6-6) and (6-1). Solving them by applying the slip condition for velocity and the jump condition for temperature, we can obtain the temperature distribution and then the heat flux between the slider and the air bearing. The results have been solved in Chapter 6. For convenience of analysis, we write it out here again:

$$q = -k \frac{T_s - T_d}{h + 2b\lambda} + \frac{h^3}{24\mu}\left[\left(\frac{\partial p}{\partial x}\right)^2 + \left(\frac{\partial p}{\partial y}\right)^2\right] + \frac{\mu U^2 h}{2(h + 2a\lambda)^2} - \frac{U h^3}{6(h + 2b\lambda)(h + 2a\lambda)} \frac{\partial p}{\partial x} , \tag{7-8}$$

where all the variables and parameters are the same as in the Chapter 6.

7.3 Solution Approaches

The solution of the heat flux is decoupled from the solution of the dynamic slider air bearing because of the introduction of the quasi-steady heat transfer approximation. The unsteady Reynolds equation, which needs to be solved first, is discretized using Partanka’s (1980) control volume method and solved by an alternative directional sweep method combined with a multi-grid control volume method. Equations (7-1)~(7-3) are integrated directly. At each iteration, the pressure profile is obtained by solving the Reynolds equation for a given flying height. Then the pressure profile is used to solve equations (7-1) ~ (7-3) to obtain the new displacements of the slider. The new displacements are compared with the previous ones to check if further iteration is needed. The detailed description of these approaches can be found in the related documents (Cha and Bogy, 1995; Lu and Bogy, 1994; Hu, 1996) and will not be presented here.

With the pressure distribution and the air bearing spacing obtained, the pressure gradient can be calculated and then the heat flux between the slider and air bearing is obtained using equation (7-8) for each flying state (or each iteration step). Note that the air bearing spacing used in solving the Reynolds equation is evaluated by considering the height of the asperity, bump, or any other roughness on the disk surface. This spacing is also used in solving the heat transfer in the air bearing. The whole solution procedure is implemented by using a thermal analysis code combined with the CML Air Bearing Dynamic Simulator (Hu and Bogy, 1995).

7.4 Simulation Results and Discussions

For convenience, we choose a 50% (2*mm*×1.6*mm*) tri-pad slider (Fig. 6-3) as used in Chapter 6, as an example, in the analysis. The slider has all given conditions as before and is fixed at a radial position r=23 *mm* with a disk rotation speed 6400 *rpm*. The pressure profile is shown in Fig. 6-4, and the steady state flying height is 44 *nm*.

In the following analysis, unless otherwise stated we use the convention that a positive heat flux means the heat is transferred out of the slider.

7.4.1 Slider Flying Over a Square Asperity

In this section, we study the heat transfer between a slider and the air bearing when the slider flies over a rectangular asperity. The asperity used is 30 *nm* in height, 150μm in length and 300μm in width. Since the slider usually has a higher temperature than the ambient air or disk, we take T_s–T_d=20 °C and we assume that these temperatures remain constant through the whole process. Figure 7-1 shows the variation of the air bearing thickness at a single point close to the central trailing edge (about 5 μm away from it), and Fig. 7-2 is the related heat flux. We also plot the heat conduction and viscous dissipation components in Fig. 7-3 and 7-4 separately to see their contribution to the total heat flux. From these figures it is clear that the heat conduction dominates the heat transfer in this case.

When the tri-pad slider flies over the asperity located along its centerline, the air bearing thickness does not change until the asperity reaches and passes under the trailing edge rail (TER) (Fig.7-1). This is because the slider's flying state is affected by the pressure profile in the air bearing, which does not change much when the asperity goes through the recessed region. When the asperity gets close to the TER, the air bearing thickness first slightly increases, which is caused by the increase of the slider’s flying height, and then decreases sharply as the TER passes over the asperity. Note that the air bearing thickness here is a combined result of the increase of the flying height and the reduction of the asperity height. When the asperity leaves the trailing edge, the air bearing thickness increases sharply and then decreases and starts to vibrate around its steady value.

Corresponding to the variation of the air bearing thickness, the heat conduction decreases slightly at first and then increases sharply (Fig. 7-3) when the asperity reaches the TER. When the asperity leaves the trailing edge, it goes down sharply and then goes up and starts to vibrate afterwards. Comparing Fig. 7-3 with Fig.7-1, we see that the variation of the heat conduction follows inversely the air bearing thickness almost exactly. That is, the heat conduction increases with a decrease of the air bearing thickness and decreases with an increases of the air bearing thickness. In other words, more heat is transferred out of the slider when the air bearing thickness is smaller. This is a natural conclusion because the smaller the thickness, the smaller the thermal resistance for conduction.

From the results of the viscous dissipation (Fig.7-4), we draw the same conclusion as for the heat conduction. But here the heat flux takes negative values, which means the heat is transferred from the air bearing to the slider. Therefore, less heat is dissipated into the slider with the decrease of the air bearing thickness.

The total heat flux is the sum of the above two portions of heat transfer (Fig.7-2). Its profile is the same as that in Fig.7-3 and 7-4. Combining all these results, we can say that the “cooling” effect increases with a decrease of the air bearing thickness. This conclusion is similar to the results in the Chapter 6, in which the variation of the heat flux was obtained for various steady cases by changing the flying height through changing the disk rotation speed.

In the above analysis, we studied the mechanism of the heat flux variation for a single point. But a MR sensor is actually affected by the heat flux over a finite surface area around it. To study this overall thermal effect, we use the same case as above but we focus on the average values of the heat flux determined over the air bearing surface of the TER. We also shift to compare them with the flying height at the central trailing edge (FH-CTE) instead of with the local air bearing thickness at a point. Simulation results for flying height, heat flux, heat conduction component and heat dissipation components are, respectively, shown in Fig. 7-5 to 7-8. It is seen that the FH-CTE does not change before the asperity reaches the TER (Fig.7-5). When the asperity reaches the TER and goes through the air bearing, the FH-CTE increases sharply and then decreases when the asperity leaves the trailing edge, after which it vibrates around the steady state flying height. Corresponding to the variation of the FH-CTE, the response of the average heat conduction can be divided into two intervals as shown in Fig.7-7. In the interval I, the average heat conduction increases when the asperity begins to occupy the air bearing of the TER, which leads to a decrease of the average air bearing thickness. After that, the heat conduction decreases due to the increase of the average air bearing thickness contributed by the asperity leaving the TER air bearing. In the interval II, since the effect of the asperity height vanishes, the variation of the air bearing thickness directly follows that of the flying height. Therefore, the average heat conduction increases with the decreases of the FH-CTE, and decreases with the increases of the FH-CTE.

It is interesting to note that the average viscous dissipation decreases when the asperity begins to occupy the air bearing of the TER, or more heat is dissipated into the slider when the average air bearing thickness decreases (Fig. 7-8). This result is opposite to that for a single point analyzed (see Fig.7-4). It may be related to the effects of the maximum heat dissipation in the SDI. In Chapter 6, we point out that the maximum viscous dissipation increases in magnitude as the FH-CTE, or the average air bearing thickness, decreases. The reason for this may be that the pressure profile at the corners of the TER, where there exists more drastic pressure variations at the smaller air bearing thickness, becomes steeper at the smaller air bearing thickness, which increases the pressure gradient and also the magnitude of the viscous dissipation at these points. Due to the contribution of these points, the magnitude of the average viscous dissipation increases when the asperity goes through the air bearing under the TER. After the asperity leaves the trailing edge, the average viscous dissipation fluctuates with a small magnitude.

The average heat flux is shown in Fig.7-6. Its profile is close to that of the heat conduction because the heat conduction dominates the heat transfer in this case. Clearly, more heat is transferred out of the slider when the FH-CTE becomes lower, except for during a small period in interval I.

7.4.2 Initial Impulse

An often-met case for a working hard drive is that the drive is acted on by a sudden external impact, which causes the flying height to fluctuate drastically. To study the corresponding heat flux variation, we give an initial impulse to a steadily flying slider. For simplification, we only give a non-zero value w_{g0}=0.001 m/s to the initial vertical velocity at the gravity center of the slider. The simulation results are shown in Figs. 7-9~7-11.

It is seen that the flying height has a deflection away from its steady value at the beginning, then it vibrates and damps to its steady flying state (Fig.7-9). Since there is no effect of asperities, the variation of the flying height reflects the variation of the air bearing thickness. Following the variation of the flying height, the heat flux at a single point (same point as in the asperity case) increases with the decrease of the flying height (Fig.7-10). Similarly, the average heat flux also increases with the decrease of the FH-CTE (Fig. 7-11).

7.4.3 Effect of the Heat Flux Variation on the MR Readback

We know that the MR read-back signal is very sensitive to the temperature variation in the MR sensor, which is affected significantly by the heat transferred in or out of the MR sensor. Therefore, the variation of the heat flux caused by the fluctuation of the air bearing thickness will affect the temperature in the MR sensor, and hence its signal output. To evaluate the magnitude of this effect, we introduce a simple heat transfer model for the MR sensor, in which we assume that the MR sensor, together with its shields, is a thin plate (Fig. 7-12). The plate has an uniform temperature caused by balancing the heat generated by the current through it and the heat transfer between the plate and the air bearing. When the slider flies over an asperity, the heat flux between the plate and the air bearing changes, which in turn changes the heat balance in the sensor and causes a variation of the temperature in it. This change can be approximated as:

$$\rho_s c_s h_s \Delta T_s \approx \Delta q \Delta t \tag{7-9}$$

where ρ_s, c_s and h_s are, respectively, the density, specific heat and thickness of the MR sensor, ΔT_s is the temperature variation in the MR sensor, Δq is the variation of the heat flux between the sensor and air bearing and Δt is the heating time.

For a typical MR sensor, we can take ρ_s~8000 kg/m^3, c_s~400 $J/kg\cdot K$ and h_s~2 μm. We also have Δq~7×10^4 W/m^2 and the related Δt~10^{-5} sec (Fig. 7-7) for the slider flying over an asperity. Thus, we obtain the temperature variation ΔT_s~0.11 °C by equation (7-9). Based on a correlation between the temperature and resistance (Tian, et al, 1997), we obtain the resistance variation in the MR sensor as: $\Delta R_s = \alpha R_s \Delta T_s \approx 0.00239 \times 30 \times 0.11 \approx 0.008\ \Omega$, where R_s is the resistance of the MR sensor which is about 30 Ω and ΔR_s is its variation, and α is a coefficient obtained by experiment. Note that the typical resistance variation during MR readback is about 0.5% (Waldera, 1997). So the flying height variation caused by a slider flying over an asperity can result in about 5% of the variation of the MR readback signal.

7.4 Summary

We introduced a quasi-steady model for the heat transfer in the air bearing combined with a dynamic air bearing design model in this chapter. Using this model, we studied the mechanism of the variation of the heat flux when a slider flies over an asperity and when a slider is given an initial impulse. The simulation results show that the heat flux is related to the air bearing thickness. That is, a decrease in the air bearing thickness will increase the heat transferred out of the slider. When a slider flies over an asperity, its flying height fluctuates, which causes the air bearing thickness and the heat flux between the slider and the air bearing to fluctuate simultaneously. Since a decrease of the flying height usually causes a decrease of the air bearing thickness, it therefore increases the heat transferred out of the slider.

A similar result is obtained for a flying slider given an initial impulse, which causes the fluctuation of the flying height and then causes a variation of the heat flux between the slider and the air bearing.

Based on a simple heat transfer model for the MR sensor, we estimate the temperature variation caused by the fluctuation of the slider’s flying height to be about 0.1 °C, which causes the MR signal output to vary by about 5%.

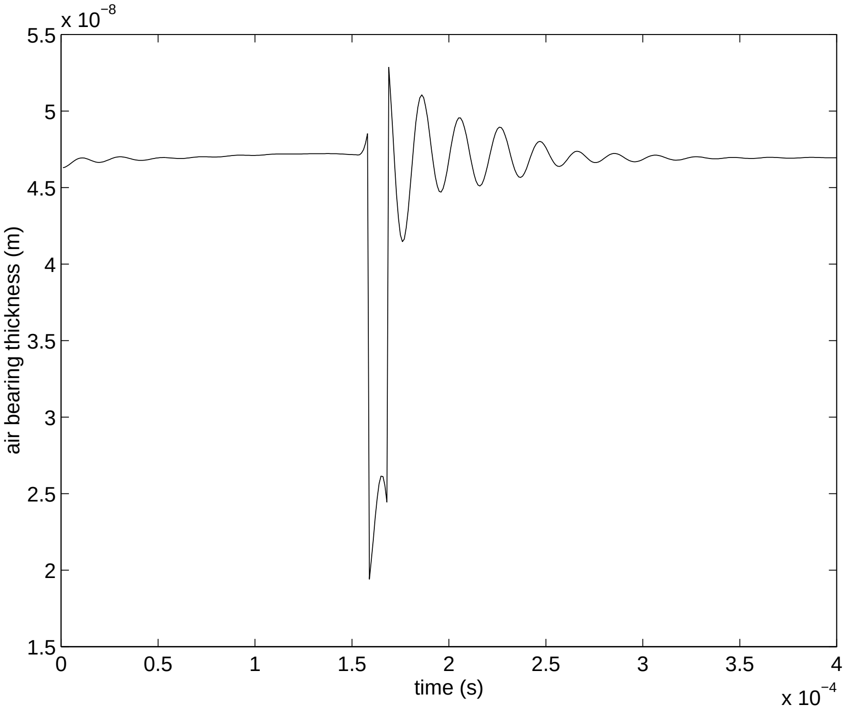

Fig. 7-1 Variation of the air bearing thickness (single point located at 5 μm from the CTE) for a tri-pad slider passing over an asperity

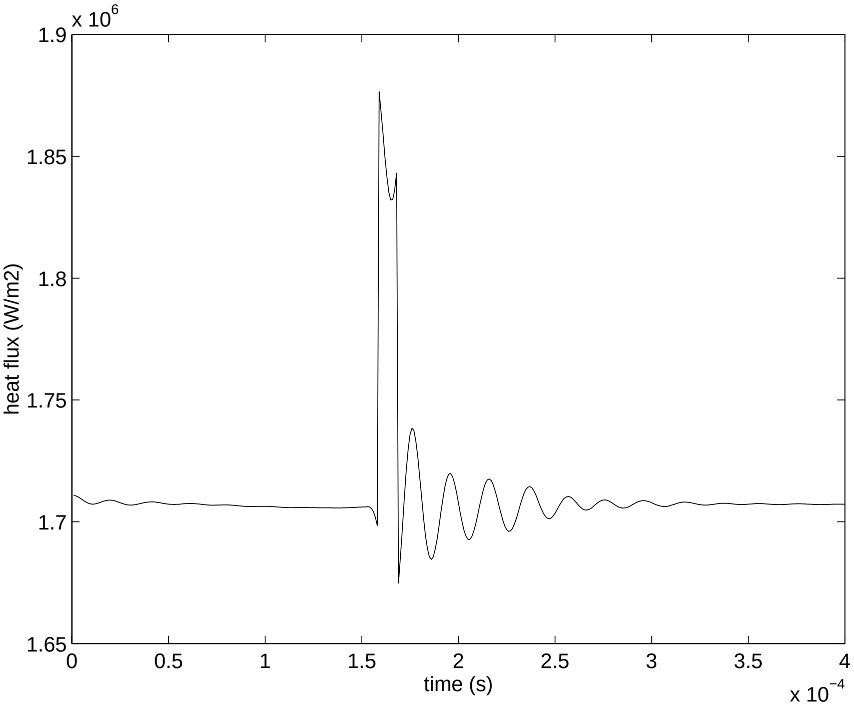

Fig. 7-2 Variation of the heat flux (single point located at 5 μm from the CTE) for a tri-pad slider passing over an asperity

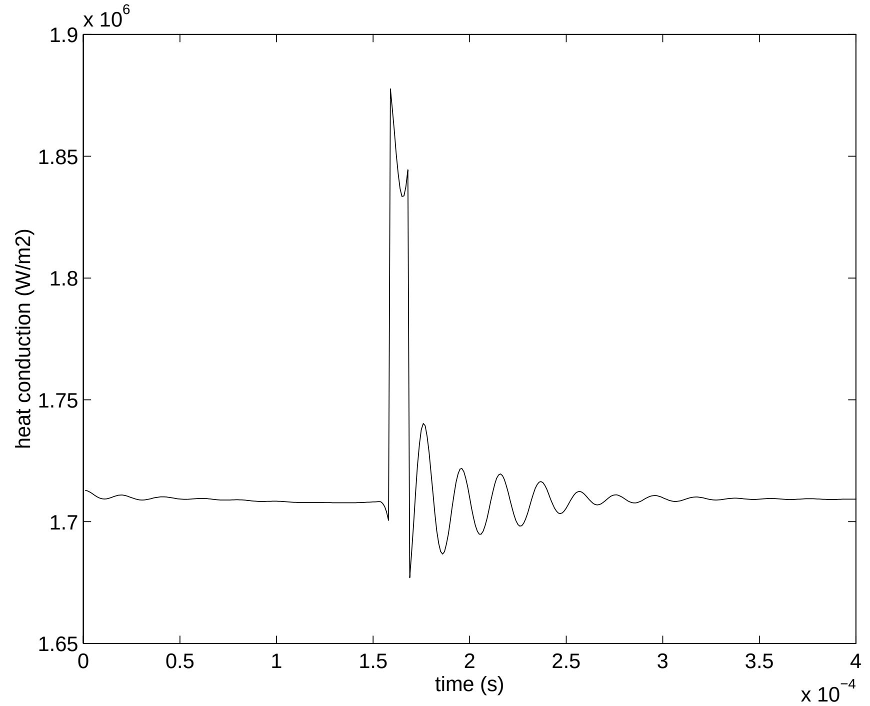

Fig. 7-3 Variation of the heat conduction component (single point located at 5 μm from the CTE) for a tri-pad slider passing over an asperity

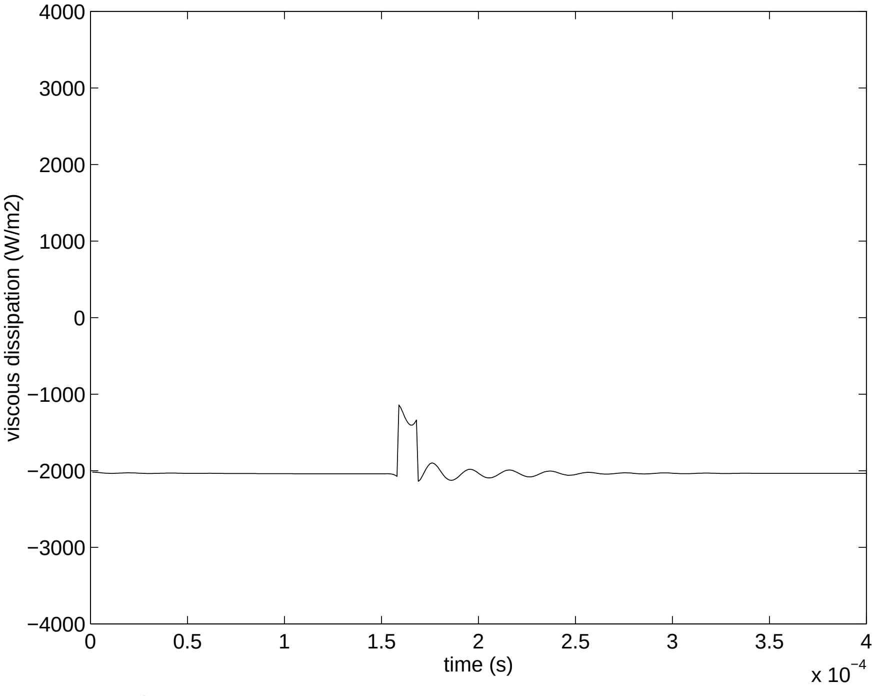

Fig. 7-4 Variation of the heat dissipation component (single point located at 5 μm from the CTE) for a tri-pad slider passing over an asperity

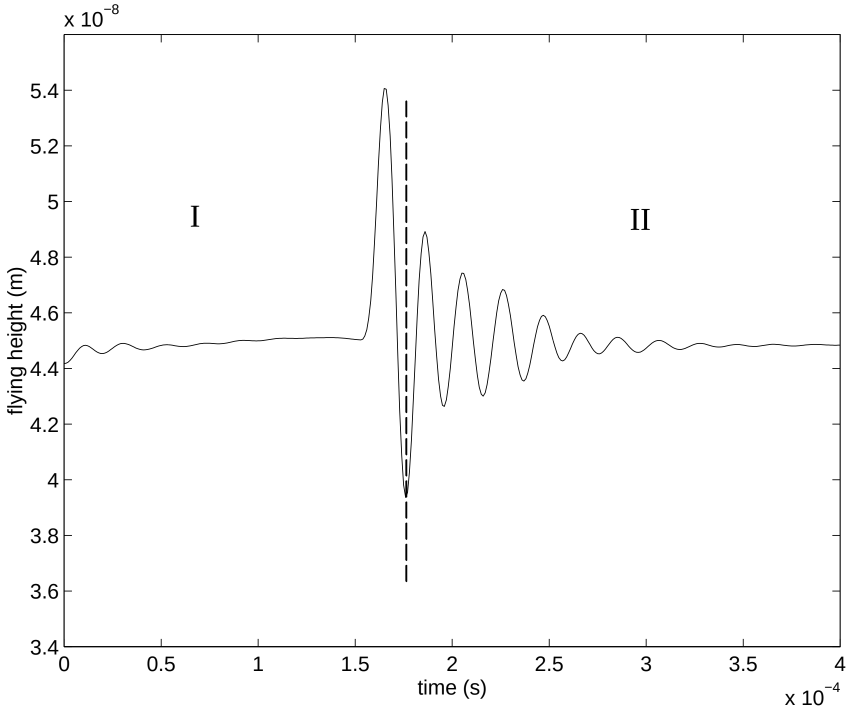

Fig. 7-5 Variation of the flying height for a tri-pad slider passing over an asperity

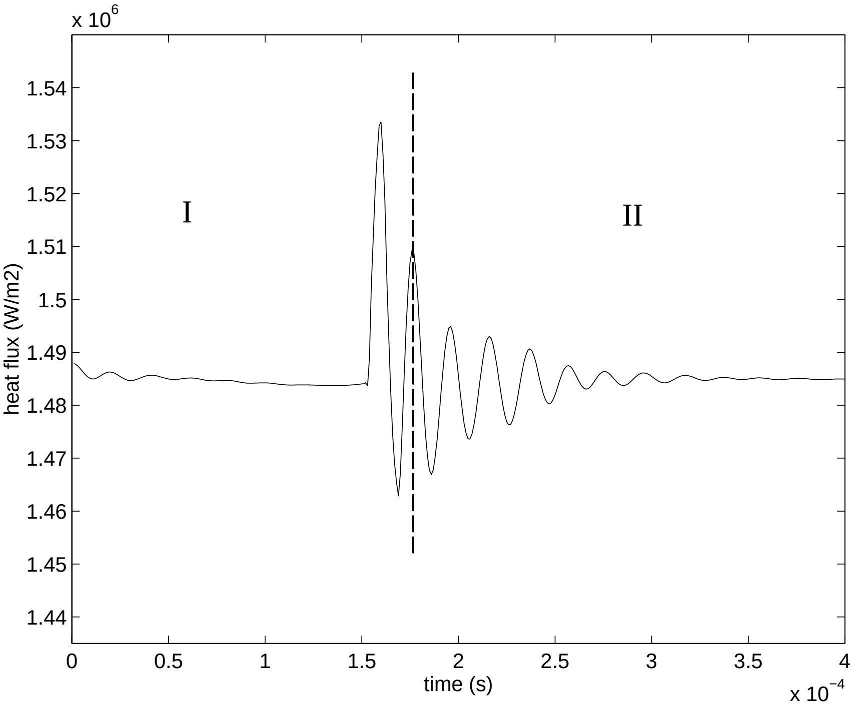

Fig. 7-6 Variation of the heat flux (averaged value over the TER) for a tri-pad slider passing over an asperity

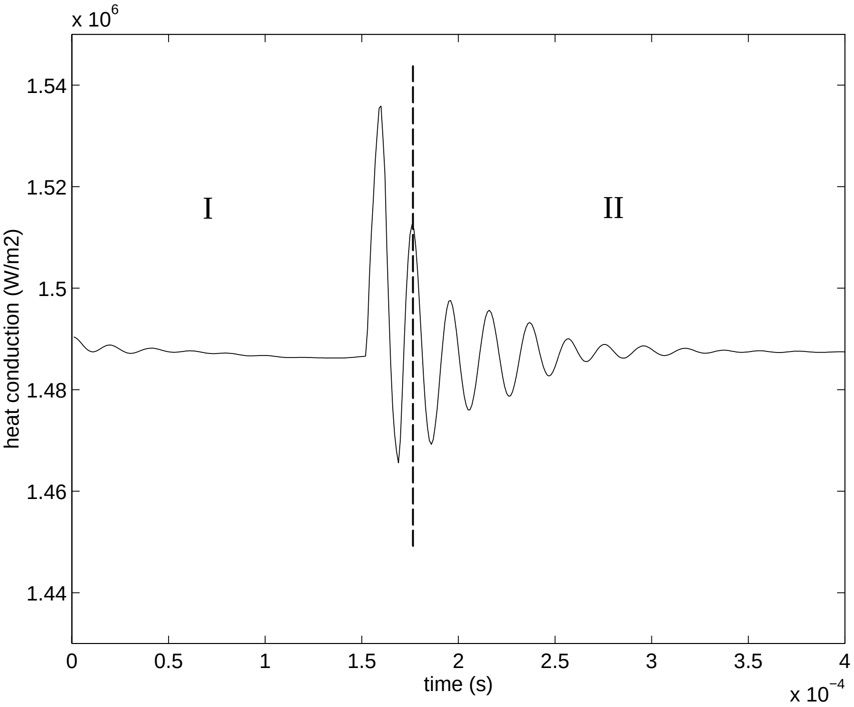

Fig. 7-7 Variation of the heat conduction component (averaged value over the TER) for a tri-pad slider passing over an asperity

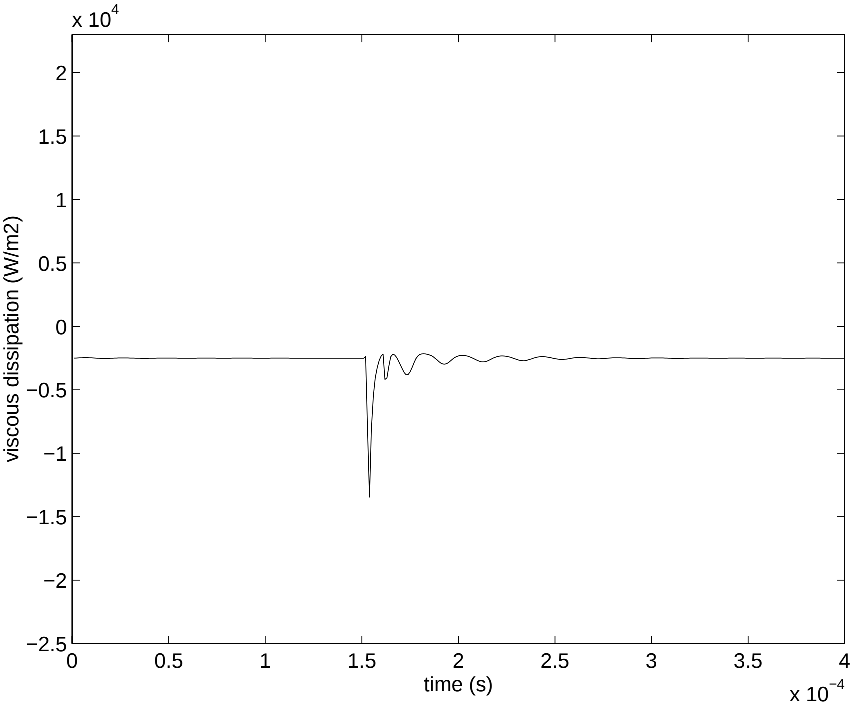

Fig. 7-8 Variation of the heat dissipation component (averaged value over the TER) for a tri-pad slider passing over an asperity

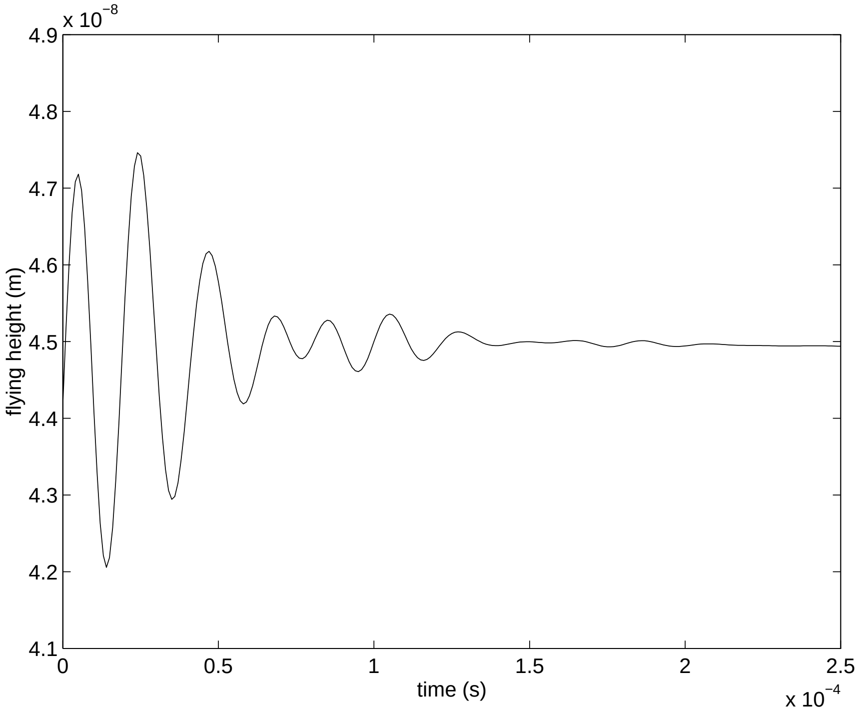

Fig.7-9 Variation of the flying height for a tri-pad slider given an initial impulse

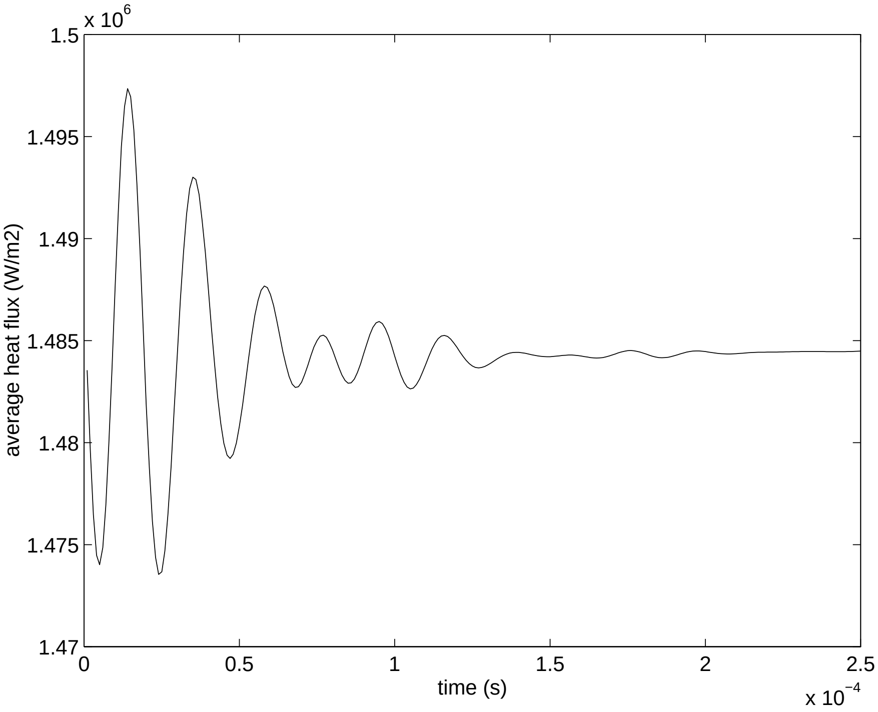

Fig.7-10 Variation of the heat flux (averaged value over the TER) for a tri-pad slider given an initial impulse

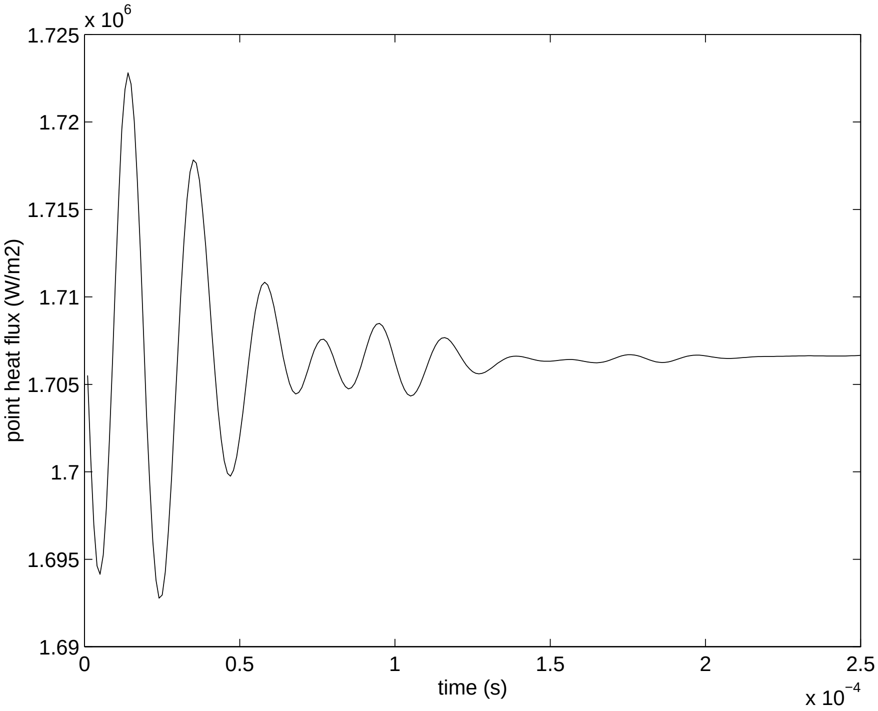

Fig.7-11 Variation of the heat flux (single point located at 5 μm from the CTE) for a tri-pad slider given an initial impulse

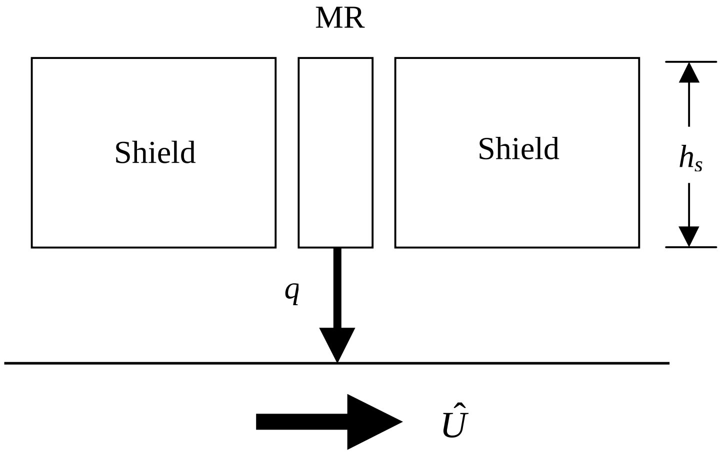

Fig. 7-12 Diagram of the heat transfer model for the MR sensor

CHAPTER 8

CONCLUSION

Particle contamination and thermal asperity are two concerns in proximity recording in the hard drive industry. The former may cause SDI failures, resulting in loss of data on the disk media; the latter is detrimental to the MR head and may disturb the feedback loops for gain and timing control and cause the signal amplitude to exceed the dynamic range of the circuit, resulting in device saturation and signal clipping. Both of these phenomena reduce the reliability of the operations of hard drives. In this thesis, we studied, separately, the mechanism of the particle contamination in a SDI, cooling effect of the air bearing and the thermal effect on the MR readback when a slider flies over an asperity without contact.

8.1 Particle Contamination

We develop a model describing the motion of particles in a SDI using a Lagrangian approach. We focus our study on a single particle since the particles are dilute in a real SDI, so that the interaction between different particles is negligible. Various forces, such as drag, Saffman lift and gravity forces, are considered in the model. The Saffman force arises when the particle moves in a shear flow, and it acts on the particle in a direction perpendicular to the local air flow. The motion equations are simultaneous ODE's and the overall solution of them includes two steps: first, solving the velocity field in the SDI, which involves solving the Reynolds equation using a multi-grid control volume method combined with a alternative direction sweep method; second, solving the motion equations by a fourth order Runge-Kutta method. The computation is implemented by a FORTRAN program.

Through simulations of various cases, we obtained the following characteristics for a particle moving in a SDI:

(1) Saffman force is significant for larger particles, and is negligible for the particles with size d<200 *nm*;

(2) Large particles with higher relative velocity are acted on by a larger Saffman force pointing to the slider surface. Since the air flow has a lower velocity in a recess region, the particles entering into the recess region usually have a high relative velocity and are brought by the Saffman force to the slider surface. Therefore, contamination is prone to occur on the surface of a cavity or a recess region;

(3) Small particles follow the streamlines very well. Changes in density and relative velocity do not result in significant changes in their motion paths.

Based on the above results, we designed an anti-contamination slider. The principal concept of this design is that the particle contamination on a slider can be reduced if we can make as many particles as possible leave the SDI from its sides, instead of from its trailing edge. This requirement can be realized by using the flow in the SDI to blow particles out of it from sides, which we call the “inherent cleaning process”.

Since flying stability is also a requirement in designing a slider, we modified the anti-contamination slider by using the CML Optimization Program to make it fly stably (with minimum variation in flying height) from ID to OD. The new slider is named the

“Sparrow” slider because it has a sparrow-like rail shape. Simulation results show that the anti-contamination characteristics still remain for the “Sparrow” slider.

Particle contamination in a SDI is a very complicated process. It is not only related to the motion characteristics of a particle, but also related to the interaction modes of a particle with the disk surface or slider surface, which in turn is related to the momentum exchange, deformation, material properties, and dynamic characteristics of the slider. In this thesis, we focus our study on the motion of a single particle in a SDI to investigate the mechanism of the contamination by simulating the particle paths without considering the interaction of the particle with disk or slider surface. Since the latter is also an important issue in particle contamination, we need to expand this study in a future project.

8.2 Thermal Asperity

Thermal asperity was proposed originally to describe the thermal effect on the MR readback by the contact between the MR head and roughness points on the disk surface. A recent paper (Tian, et al., 1997) showed that there exists another thermal effect when a slider flies over an asperity without contact. It was concluded that the air bearing acted as a coolant in this situation. To study the mechanism of the cooling effect of the air bearing is the motivation of this project.

We first develop a steady heat transfer model in a SDI. This is a micro-structure heat transfer problem because the spacing of the SDI is comparable to the mean free path of the air. In developing this model, we choose a simple approach by assuming that the governing equations which are based on the continuum assumption are still valid. As a modification, we apply the discontinuous boundary conditions for both the N-S equation and energy equation. We also assume that the physical properties of the air are constant throughout the SDI because the velocity of the air flow is much smaller than the sound speed and the temperature variation across the spacing is also much smaller than the reference temperature. Therefore, we can decouple the N-S equation and the energy equation to make the solution much simpler.

The heat transfer between a slider and the SDI is obtained by integrating the reduced N-S and energy equations. The result shows that the heat transfer consists of two parts: heat conduction which transfers heat from the slider to the SDI if the slider has a higher surface temperature than that of the disk, and viscous dissipation which transfers heat to the slider. The heat conduction usually has a larger magnitude than the viscous dissipation, except for some points at the corners of the trailing edge air bearing or the temperature difference between the disk and slider surfaces are close to zero.

We also studied the heat flux variation by changing the flying height of the slider. Note that the model we used is a steady model. Therefore, changing the flying height is actually realized by changing the disk rotation speed (we fix the slider position). Through simulation we find the lower the flying height (or disk rotation speed), the more heat flows out of the slider (assume the slider surface has higher temperature than the disk surface).

We still can not use the results from the steady model to verify Tian, et al’s (1997) work, not only because the heat flux variation mentioned above is a combined result of changing flying height and disk speed, but also because Tian, et al’s work was done for a slider flying over an asperity, which is an unsteady problem. Therefore, we expanded the steady analysis to the dynamic cases.

We proved through dimensional analysis that the heat transfer in the air bearing for a slider flying over an asperity without contact is quasi-steady. Therefore, we can use the heat transfer expression obtained from the steady state model in the dynamic model. Through solving the dynamic heat transfer model, we find that the heat flux varies following the variation of the air bearing spacing. The closer the slider to the disk surface, the more heat is transferred out of the slider. In other words, the air bearing acts as a coolant. This result is identical to the conclusion obtained by Tian, et al. Using a simplified model, we estimate that the variation of the MR readback caused by the fluctuation of the flying height (or air bearing spacing) is about 5% of the total MR readback output.

The temperature response of a MR transducer is a complicated process for a slider flying over an asperity with contact or without contact. Its variation causes the changes of the heat flux between the slider and air bearing, which in turn changes the temperature of the MR transducer again. Therefore, the whole process is dynamic and needs to be solved using an unsteady heat transfer model which combines unsteady heat conduction inside the slider and dynamic heat transfer in the air bearing. The computation time is likely to be huge for the numerical solution of such a model.

REFERENCES

[1] Best, G. L., Sept. 1997, “Contact Recording: Balancing Drive Mechanics and Magnetics”, *Data Storage*, pp.65.

[2] Bogy, D. B., Lu, S., O’Hara, M. and Zhang, S., 1996, “Some Advanced Air Bearing Design Issues for Proximity Recording”, presented in *Int. 1996 ASME/STLE Trib. Conf.*, and to appear in *ASME Journal of Tribology*.

[3] Brenner, H., 1961, “Effect of Finite Boundaries on the Stokes Resistance of An Arbitrary Particle”, *Chem. Eng. Sci.*, 16, pp 242.

[4] Burgdorfer, A., 1959, "The Influence of the molecular Mean Free Path on the Performance of Hydrodynamics Gas Lubricated Bearing", *ASME Journal of Basic Engineering*, Vol. 81, No. 1, pp. 94-100.

[5] Carslaw, H. S., Jaeger, J. C., (1986), *Conduction of Heat in Solid*, Clarendon Press, Oxford.

[6] Cha, E. T., 1993, “Numerical Analysis of Head-Disk Assembly Dynamics for Shaped Rail Sliders with Sub-ambient Pressure Regions”, Doctoral Dissertation, Department of Mechanical Engineering, University of California, Berkeley.

[7] Cha, E. T., Bogy, D. B., 1995, “A Numerical Scheme for Static and Dynamic Simulation of Sub-ambient Pressure Shaped Rail Sliders”, *ASME Journal of Tribology*, Vol. 117, p.36-46.

[8] Chen, M., McLaughlin, J. B., 1995, "A New Correlation for The Aerosol Deposition Rate in Vertical Ducts", *Journal of Colloid and Interface Science*, 169, pp.437-455.

[9] Clift, R., Grace, J. R., Weber, M. E., 1978, “Bubbles, Drops, and Particles”, *Academic Press*.

[10] Cox, R. G., Hsu, S. K., 1977, “The Lateral Migration of Solid Particles In A Laminar Flow Near A Plane”, *Int. J. Multiphase Flow*, Vol. 3, pp. 201-222.

[11] Faxen, H., 1923, Arkiv. Mat. Astro. Fys. 17, No. 8, *Dissertation*, Uppsala Univ.

[12] Fukui, S., Kaneko, R., 1988, “Analysis of Ultra-thin Gas Film Lubrication Based on Linearized Boltzmann Equation: First report-Derivation of A Generalized Lubrication Equation Including Thermal Creep Flow”, *ASME Journal of Tribology*, Vol. 110, p.253-261.

[13] Fukui, S., Kaneko, R., 1990, “A Database for Interpolation of Poiseuille Flow Rates for High Knudsen Number Lubrication Problems”, *ASME Journal of Tribology*, Vol. 112, p.78-83.

[14] Gans, R., 1985, “Lubrication Theory at Arbitrary Knudsen Number”, *J. of Tribology*, Vol. 107, p.431-433.

[15] Garcia-Suarez, C., Bogy, D. B., Talke, F. E., 1984, “Use of an Upwind Finite Element Scheme for Air Bearing Calculation”, *ASLE SP-16*, pp. 90-96.

[16] Golaman, A. J., Cox, R. G., Brenner, H., 1967, "Slow Viscous Motion of A Sphere Parallel to A Plane Wall -I: Motion through a Quiescent Fluid", *Chemical Engineering Science*, Vol. 22, pp.637-651.

[17] Gross, W. A., et al, 1980, "Fluid Film Lubrication", *John Wiley & Sons, Inc.*

[18] Hempstead, R. D., (1974) “Thermally Induced Pulses in Magnetoresistive Heads”, *IBM J. Res. & Dev.*, Vol.18, P547-550.

[19] Hiller, B., Brown, B., 1993, “Interaction of Individual Aluminum Particles with the Head-Disk Interface at Various Velocities”, *Adv. Info. Storage Syst*., Vol. 5, p.351-361.

[20] Hiller, B., Singh, G. P., 1991, “Interaction of Contamination Particles with the Particulate Slider/Disk Interface”, *Adv. Info. Storage Syst*., Vol. 2, p.173-180.

[21] Hsia, Y. T., Domoto, G. A., 1983, "An Experimental Investigation of Molecular Rarefaction Effects in Gas Lubricated Bearings at Ultra-Low Clearance", *ASME Journal of Tribology*, Vol. 105, No. 1, pp. 120-130.

[22] Hu, Y., Bogy, D. B., 1995, “The CML Air Bearing Dynamic Simulator”, *CML Tech. Report*, No 95-011, UC Berkeley.

[23] Hu, Y., Bogy, D. B., 1996, “Dynamic Simulation and Spacing Modulation of Sub-25 nm Fly Height Sliders”, presented in *96 International Tribology Conference* (ASME paper No. 96-Trib-56), to appear in *ASME Journal of Tribology*.

[24] Hunt, A. P., 1971, “A Magnetoresistive Readout Transducer”, *IEEE Transactions on Magnetics*, Vol. Mag-7, No. 1, pp.150-154.

[25] Jander, A., Indeck, R. S., Brug, J. A., Nickel, J. H., (1996) “A Model for Predicting Heating of Megnetoresistive Heads”, *IEEE Tran. On Mag.*, Vol.32, N.5, p3392-3394.

[26] Kennard, A. H., 1938, “Kinetics Theory of Gases”, *McGraw-Hill Book Company, Inc*., New York and London.

[27] Koka, R., 1989a, “Effects of Fine Particles on the Slider/Disk Interface in Rigid Disk Drives”, *Tribol. Mech. Magn. Storage Systems*, STLE SP-26, p. 40-46.

[28] Koka, R., Kumaran, A. R., 1991, “Visualization and Analysis of Particulate Buildup on the Leading Edge Tapers of Sliders”, *Adv. Info. Storage Syst*., Vol. 2, p.161-171.

[29] Liang, Y., Shi, X., Xu, X., 1993, “Study on Turbulent Dispersion of Solid Particles in Plate Jet Near the Nozzle”, (in Chinese), *J. of Engineering Thermophysics*, Vol. 14, No. 4, p.439-444.

[30] Liu, B., Hu, S. B., Soo, K. T. and Wang, J. P., “Contamination Build-up on ABS and Its Effects on Read/Write Performance of Near-Contact Recording Systems”, *IEEE Transactions on Magnetics*, Vol. 32, No.5, 1996.

[31] Liu, V. C., Pang, S. C., Jew, H., 1965, “Sphere Grad in Flows of Almost-Free Molecules”, *The Physics of Fluids*, Vol. 8, No. 5, pp. 788-796.

[32] Lu, S., Bogy, D. B., 1994, “A Multi-Grid Control Volume Method for the Simulation of Arbitrarily Shaped Slider Air Bearings with Multiple Recess Levels”, *CML report*, No. 94-016, UC Berkeley.

[33] Lu, S., Bogy, D. B., 1995, “CML Air Bearing Design Program User’s Manual”, *CML report*, No. 95-003, UC Berkeley.

[34] Lu, S., 1997, *Numerical Simulation of Slider Air Bearing*, Doctoral Dissertation, Department of Mechanical Engineering, University of California, Berkeley.

[35] Maxey, M. R., 1993, “The Equation of Motion for A Small Rigid Sphere in A Nonuniform or Unsteady Flow”, *Gas-Solid Flows*, Fed-Vol. 166, p.57-62.

[36] McLaughlin, J. B., 1993, "The Lift on a Small Sphere in Wall-bounded Linear Shear Flows", *Journal of Fluid Mechanics*, Vol. 246, pp. 249-265.

[37] Miu, D. B., Bogy, D. B., 1986, “Dynamics of Gas Lubricated Slider Bearings in Magnetic Recording Disk Files: Part II – Numerical Simulation”, *ASME Journal of Tribology*, Vol. 108, pp. 584-588.

[38] Millikan, R. A., 1923, “The General Law of Fall of A Small Spherical Body through A Gas, and Its Bearing Upon the Nature of Molecular Reflection from Surfaces”, *Physical Reviews*, Vol.22, No.1, pp.1-23.

[39] Mitsuya, Y., 1993, "Modified Reynolds Equation for Ultra-Thin Film Gas Lubrication Using 1.5-Order Slip-Flow Model and Considering Surface Accommodation Coefficient", *ASME Journal of Tribology*, Vol. 115, pp. 289-294.

[40] News, 1997, “IBM extends capacity of Laptop Drives to 5 GB”, *Data Storage*, July/August, pp.8.

[41] O'Hara, M., Hu, Y., and Bogy, D. B., 1996, “Effects of Slider Sensitivity Optimization”, *IEEE Transactions on Magnetics,* Vol.32, 5, p.3744-3746.

[42] O'Hara, M., and Bogy, D. B., 1995, “CML Air Bearing Optimization Program”, *CML Technical Reports*, No.95-015.

[43] O'Neill, M. E., 1965, "A Slow Motion of Viscous Liquid Caused By A Slowly Moving Solid Sphere", *Mathematika* 11, pp. 67-74.

[44] Patankar, S. V., 1980, *Numerical Heat Transfer and Fluid Flow*, McGray-Hill, New York.

[45] Rottmayer, R. E., Tong, H-C., 1997, “Magnetic Recording Heads for 3 GB/in^2 and Beyond”, *IDEMA Insight*, Vol. X, No.5, pp.1.

[46] Rubinow, S. I., Keller, J. B., 1961, “The Transverse Force on A Spinning Sphere Moving in A Viscous Fluid”, *J. Fluid Mech*., Vol. 11, part 3, p.447-459.

[47] Ruiz, O. J., Bogy, D. B., 1990, “A Numerical Simulation of the Head-Disk Assembly in Magnetic Head Disk: 1. Component Models”, *ASME Journal of Tribology*, Vol. 112, pp. 593-602.

[48] Saffman, P. G., 1965, “The Lift on A Small Sphere in A Slow Shear Flow”, *J. Fluid Mech*., Vol. 22, part 2, p. 385-400.

[49] Shimomizuki, N., Adachi, T., et al, 1993, “Numerical Analysis of Particle Dynamics in A Bend of A Rectangular Duct by the Direct Simulation Monte Carlo Method”, *Gas-Solid Flows*, Fed-Vol. 166, p.145-152.

[50] Shyy, W., Sun, C. S., 1993, "Development of A pressure-correction/Staggered-grid Based Multi-grid Solver for Incompressible Recirculating Flows", *Computer and Fluids*, Vol. 22, No. 1, pp.51-76.

[51] Singer, P., Feb. 1997, “Read/Write Heads: The MR Revolution”, *Semiconductor International*, pp.71.

[52] Sommerfeld, M., Qiu, H., 1993, “Characterization of Particle-Laden, Confined Swirling Flows by Phase-Doppler Anemomentry and Numerical Calculation”, *Int. J. Multiphase Flow*, Vol. 19, No. 6, p. 1093-1127.

[53] Talke, F. E., Tseng, R. C., 1973, “An Experimental Investigation of the Effect of Medium Thickness and Transducer Spacing on the Read-Back Signal in Magnetic Recording Systems”, *IEEE Transactions on Magnetics*, Vol. MAG-9, No.2, pp.133-139.

[54] Tian, H., Cheung, C-Y., Wang, P-K., “Non-Contact Induced Thermal Disturbance of MR Head Signals”, *IEEE Trans. Magn.*, in press, 1997.

[55] Waldera, Jay, (May/June) 1997, “Who is Afraid of Thermal Asperities in MR Drives?”, *Data Storage*, pp55-62.

[56] Wakiya, S. J., 1957, “Viscous Flows past A Spheroid”, *Journal of the Physical Society of Japan*, Vol. 12, No. 10, pp 1130-1141.

[57] Wakiya, S. J., (1960), *Res. Rep. Fac. Eng. Niigata Univ.*, (Japan) 9, 31.

[58] White, R. M., 1985, “Introduction to Magnetic Recording”, *IEEE Press*, New York.

[59] White, J. M., Nigam, A., 1980, “A Factored Implicit Scheme for the Numerical Solution of the Reynolds Equation at Very Low Spacing”, *ASME Journal of Tribology*, Vol. 102, pp. 80-85.

[60] Zhang, S. and Bogy, D. B., 1997a, “Effects of Lift on the Particle Motion in Recessed Regions of a Slider”, *Physics of Fluids*, Vol. 9, No. 5, pp.1265-1272.

[61] Zhang, S. and Bogy, D. B., 1997b, “Slider Designs for Controlling Contamination”, presented in the *Int. 1996 ASME/STLE Trib. Conf.*, and published in *ASME Journal of Tribology*, Vol. 119, pp.537-540.

[62] Zhang, S. and Bogy, D. B., 1997c, “Motion of Particles in A Slider/Disk Interface Including Lift Force and Wall Effects”, presented in *INTERMAG97*, and published in the *IEEE Transactions on Magnetics*, Vol. 33, No. 5, pp.3166-3169.

[63] Zhang, S. and Bogy, D. B., 1997d, “A Heat Transfer Model for Thermal Fluctuation in An Thin Air Bearing”, with D.B. Bogy, *CML Report*, No.97-009.

[64] Zhang, S. and Bogy, D. B., 1997e, “Variation of the Heat Flux Between A Slider & the Air Bearing When the Slider Flies Over An Asperity”, accepted by the *INTERMAG98*, and will appear in the *IEEE Transactions on Magnetics*.